Journal of
METAMORPHIC GEOLOGY   **WILEY**

Hybrid phase equilibria modelling with conventional and trace element thermobarometry to assess the *P–T* evolution of UHT granulites: An example from the Highland Complex, Sri Lanka

Prasanna L. Dharmapriya[1] (ID) | Sanjeewa P. K. Malaviarachchi[1] | Andrea Galli[2] |
Leo M. Kriegsman[3,4] | Yasuhito Osanai[5] | K. Sajeev[6] | Ben-Xun Su[7] |
Toshiaki Tsunogae[8,9] | Chengli Zhang[10] | Tatsuro Adachi[5] | Chandrasekara
B. Dissanayake[1] | Nalaka Deepal Subasinghe[11]

[1]Department of Geology, Faculty of Science, University of Peradeniya, Peradeniya, Sri Lanka

[2]Department of Earth Sciences, ETH Zurich, Zurich, Switzerland

[3]Department of Research & Education, Naturalis Biodiversity Center, Leiden, The Netherlands

[4]Department of Earth Sciences, University of Utrecht, Utrecht, The Netherlands

[5]Division of Earth Sciences, Department of Environmental Changes, Faculty of Social and Cultural Studies, Kyushu University, Fukuoka, Japan

[6]Centre for Earth Sciences, Indian Institute of Science, Bangalore, India

[7]Key Laboratory of Mineral Resources, Institute of Geology and Geophysics, Chinese Academy of Sciences, Beijing, China

[8]Faculty of Life and Environmental Sciences, University of Tsukuba, Ibaraki, Japan

[9]Department of Geology, University of Johannesburg, Auckland Park, South Africa

[10]Key Laboratory of Continental Dynamics of Northwest University, Department of Geology, Northwest University, Xi'an, China

[11]National Institute of Fundamental Studies, Kandy, Sri Lanka

Correspondence
Prasanna L. Dharmapriya and Sanjeewa
P. K. Malaviarachchi, Department of
Geology, Faculty of Science, University of
Peradeniya, 20400, Sri Lanka.
Email: prasannad@sci.pdn.ac.lk (P. L. D.)
and malavi@pdn.ac.lk (S. P. K. M.)

Funding information
Indo-Sri Lanka Joint Research Grant
from the Ministry of Technology and
Research, Sri Lanka (Grant No. MTR/TRD/
AGR/3/2/20, Grant/Award Number: MTR/
TRD/AGR/3/2/20 and the Department
of Science & Technology, Government
of India: DST/INT/SL/P-24/2016; Youth
Innovation Promotion Association, Chinese
Academy of Sciences, Grant/Award
Number: 2016067; National Research
Council (NRC) of Sri Lanka, Grant/Award
Number: 15-089; University of Peradeniya
Research Grant, Grant/Award Number:
URG/18/043

Handling Editor: Simon Harley

Abstract

Here we attempt to constrain the *P–T* evolution of ultrahigh-temperature granulites using textures coupled with multiple thermobarometric approaches. Sapphirine-bearing granulites were collected from a quarry in the central part of the Highland Complex of Sri Lanka. Three sapphirine-bearing domains were selected and petrographically studied. Homogeneous sample domains were thermodynamically modelled using their bulk compositions (forward phase equilibria modelling). One heterogeneous sample from a single domain, composed of irregularly distributed residuum and melt, was also used. The bulk composition of its residual part was calculated using mineral compositions and their respective modes. Equilibrium $T–X(Fe_2O_3)$ phase diagrams were constructed in the chemical system NCKFMASHTO to estimate the bulk ferric/ferrous iron ratio, and conventional geothermometers (garnet–orthopyroxene and Al in orthopyroxene) were applied. The Ti in zircon trace element thermometer was also applied to calculate peak metamorphic conditions. Modal abundance isopleths of each mineral in equilibrium phase diagrams and textural observations were combined to constrain the retrograde *P–T* path. Our hybrid approach of forward and inverse phase equilibria modelling and conventional thermobarometric calculations indicate that the sapphirine-bearing granulites have reached

their peak *T* of 920–940°C at *P* ~10 kbar under relatively highly oxidizing conditions. Subsequently, the rocks followed a near-isobaric cooling path down to 890–860°C, prior to near-isothermal decompression up to 6 kbar. The results highlight the importance of dealing with Fe^{3+}. Multiple thermobarometric approaches on carefully observed mineral textures are required to retrieve the most reliable *P–T* conditions of HT/UHT mineral assemblages.

KEYWORDS
forward and inverse phase equilibria modelling, Sri Lanka, sapphirine granulites, thermobarometry, trace element thermometry

1 | INTRODUCTION

Ultrahigh-temperature (UHT) metamorphism is characterized by extreme thermal conditions in excess of 900°C (below the kyanite–sillimanite transition) at deep crustal levels on a regional scale (e.g. Harley, 1998, 2004). There has been a threefold increase in publications on the topic of UHT metamorphism in the last decade (Kelsey & Hand, 2015). During early studies, scientists derived UHT metamorphism primarily based on the occurrence of diagnostic mineral assemblages such as sapphirine–quartz and orthopyroxene–sillimanite–quartz, and osumilite-bearing assemblages and their inferred stabilities based on classic experimental results (e.g. Bertrand et al., 1991; Carrington & Harley, 1995; Hensen & Green, 1973; Seifert, 1974) and qualitative and quantitative petrogenetic grids (e.g. Dasgupta et al., 1995; Harley, 1998; Hensen & Harley, 1990; Kelsey et al., 2004). Subsequently, a number of workers used different methods such as garnet–orthopyroxene thermobarometry (e.g. Pattison et al., 2003), two-feldspar thermometry (e.g. Ague & Eckert, 2012; Ague et al., 2013; Baldwin & Brown, 2008; Jiao & Guo, 2011; Kooijman et al., 2012; Korhonen, Brown, Clark, & Bhattacharya, 2014), Al-in-orthopyroxene (e.g. Harley & Motoyoshi, 2000; Sajeev & Osanai, 2004), Ti-in-quartz/zircon and Zr-in-rutile thermometry (e.g. Ague & Eckert, 2012; Ague et al., 2013; Baldwin & Brown, 2008), to determine peak pressure and temperature conditions of UHT crustal metamorphism. Retrograde *P–T* trajectories have commonly been derived by interpreting reaction textures combined with petrogenetic grids, or varying relations in pressure–chemical potential space (e.g. Hensen, 1988; Hensen & Harley, 1990; Lal et al., 1987), or reaction line slopes (Kriegsman, 1996). Currently, thermodynamic modelling using pseudosections has become the dominant method, overtaking conventional thermobarometric methods to study extreme granulite facies metamorphism (e.g. Palin et al., 2016). According to Powell and Holland (2008), thermobarometry using phase equilibria modelling has been essentially qualitative. It becomes the 'forward' part of the modelling when the equilibrium phase

diagram is drawn using the composition of the equilibration volume of the rock. According to Powell and Holland (2008), the 'inverse' part of the modelling involves a qualitative comparison of the observed mineral compositions of the rock/thin section and proportions with the calculated equilibria.

However, a number of authors have pointed out the limitation of the thermodynamic modelling approach (e.g. Harley, 2008; Kelsey & Hand, 2015; Palin et al., 2016; Powell & Holland, 2008). Several factors may affect the accuracy and precision of the calculated phase diagrams. For example, the geological uncertainty related to (natural) petrographic variation at the hand sample- and/or thin section-scale, which may govern the uncertainty, influences the sample's (calculated/modelled) bulk composition, that is the primary control on the equilibrium phase relationships (Palin et al., 2016). In addition, uncertainties related to end-member data within the thermodynamic datasets (e.g. Powell & Holland, 2008), whether the activity–composition relations are realistic or not (e.g. Forshaw et al., 2019), and uncertainties associated with determination of effective bulk composition (Palin et al., 2016; Tinkham & Ghent, 2005) could also affect the interpreted *P–T* conditions using pseudosection modelling.

The conventional geothermobarometric approach has the advantage of being independent of the bulk rock composition. Nevertheless, in high-grade rocks, due to high cation diffusivity (especially of Fe and Mg), mineral compositions are easily reset (e.g. Harley, 1989). Therefore, the choice of an appropriate phase composition is problematic and application of appropriate thermobarometry for granulite facies mineral assemblages is burdened with problems, as elaborated in many studies (e.g. Frost & Chacko, 1989; Harley, 1989, 2008; Kelsey, 2008; Kelsey & Hand, 2015; Pattison et al., 2003). Owing to the relative immobility of Al compared to Fe-Mg during cooling, the Al content of orthopyroxene has been suggested as perhaps the most effective means of recovering near-peak *P–T* estimates for granulite facies rocks (Aranovich & Berman, 1997; Fitzsimons & Harley, 1994; Harley, 1984, 1998, 2004, 2008; Harley & Green, 1982). In FMAS to FMASO systems, the stability field of orthopyroxene-bearing
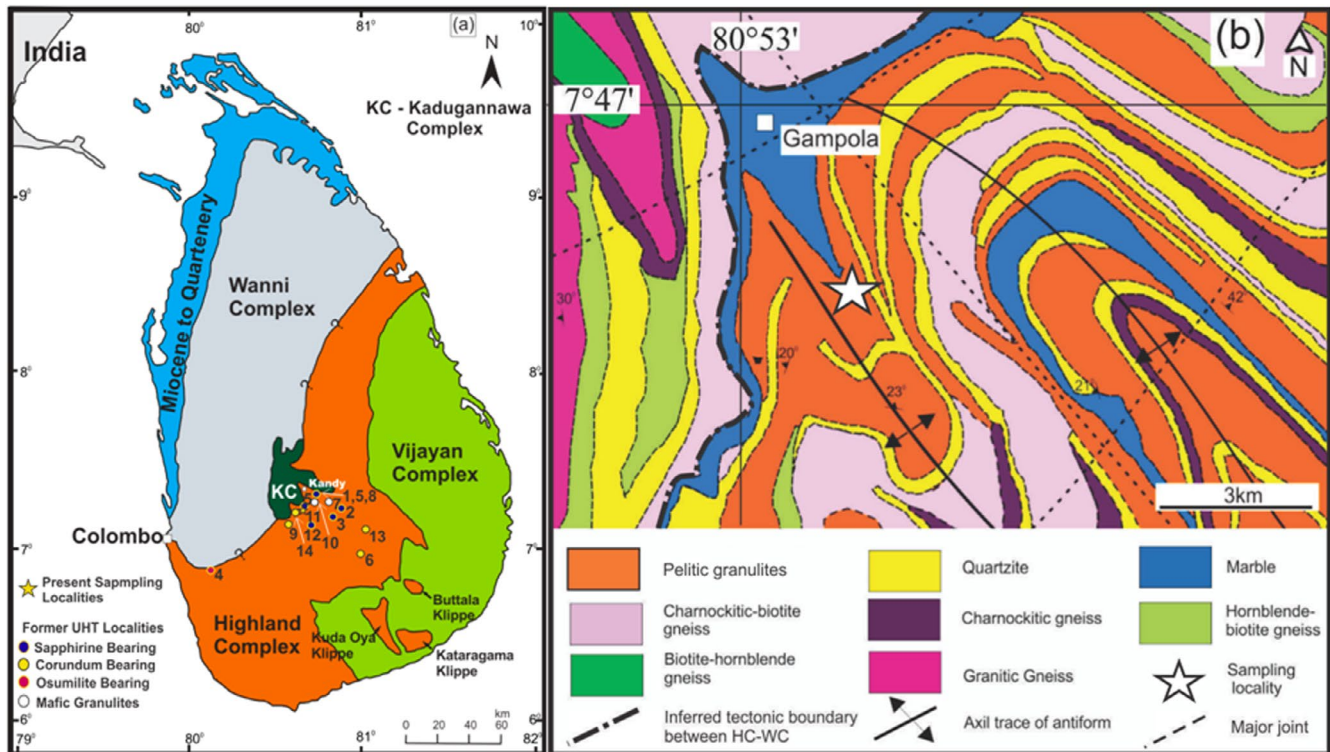
FIGURE 1 (a) Geological subdivision of the Sri Lankan basement (after Cooray, 1994). The sampling locality is shown by a star along with other reported UHT localities: 1. Osanai (1989) (>900°C); 2. Kriegsman and Schumacher (1999) (830°C, here corrected to 950°C); 3. Sajeev and Osanai (2004a) (950°C); 4. Sajeev and Osanai (2004b) (1,150°C); 5. Osanai et al. (2006) (>1,000°C); 6. Sajeev et al. (2007) (925°C); 7. Dharmapriya et al. (2014) (950–975°C); 8. Sajeev et al. (2009) (950°C); 9. Dharmapriya, Malaviarachchi, Galli, et al. (2015) (950–975°C); 10. Takamura et al. (2015) (940°C); 11*-13. Dharmapriya, Malaviarachchi, Santosh, et al. (2015) (900–975°C); 14 Dharmapriya, Malaviarachchi, Kriegsman, Galli, et al. (2017) (900°C); (b) detailed map of the area south of Gampola (Geological Survey and Mines Bureau, 1996; map sheet No. 14, used with permission), showing the khondalite localities within a zone of meta-sediments. Note: Locality 11* (Dharmapriya, Malaviarachchi, Santosh, et al., 2015) and the present sampling locality are the same [Colour figure can be viewed at wileyonlinelibrary.com]

assemblages (e.g. orthopyroxene+sillimanite±quartz) may be extended to lower T conditions under oxidizing conditions, with the preferential incorporation of Fe^{3+} into orthopyroxene under highly oxidizing conditions (e.g. Annersten & Seifert 1981; Harley, 2008). By contrast, for relatively complicated chemical systems such as extending KFMASH to KFMASHO or KFMASHTO, the stability of orthopyroxene+sillimanite is pushed to higher T because the stabilizing effect of Fe^{3+} (and Ti) on biotite to higher T is greater than any effect these components have on stabilizing orthopyroxene to lower T (e.g. White, Powell, Holland, Johnson, & Green, 2014). Hence, the $P–T$ calculations require a proper treatment of the Fe^{3+} content of the minerals involved.

Alternatively, trace element thermometers provide an advantage to measure T when the rocks lack suitable mineral assemblages to apply conventional thermobarometry (e.g Ague & Eckert, 2012; Ague et al., 2013). However, application of the thermometers may require an estimation of the activity of that trace element, if its concentration is insufficient to saturate the rock, which can lead to a high degree of uncertainty (Kelsey & Hand, 2015).

Due to the scarcity of UHT granulite occurrences worldwide (e.g. Al-Mg-rich sapphirine granulites), most studies estimate $P–T$ conditions of UHT granulites using a limited set of thermobarometric approaches (mainly using forward phase equilibria modelling and/or conventional thermobarometry) for a single rock type from an outcrop or a quarry. Thus, the influence of geological and analytical errors relevant to the $P–T$ estimations may not be easy to identify and could lead to overestimated peak metamorphic conditions.

In this context, we present an integrated approach to assess the $P–T$ conditions of sapphirine-bearing granulites based on detailed textural studies coupled with hybrid phase equilibria modelling methods (for which bulk compositions, as measured directly by XRF analysis or from measured mineral compositions and modes, have been used) together with both conventional and trace element thermobarometry. Furthermore, retrograde textures were evaluated by phase equilibria modelling, in which the mineral isopleths representing the mode (abundance) of each single mineral phase in the $P–T$ space were carefully studied to constrain a reliable retrograde $P–T$ trajectory.

2 | GEOLOGICAL BACKGROUND

Sri Lanka is a pivotal locality to study East Gondwana. According to Nd-model ages (Liew et al., 1991; Milisenda et al., 1988, 1994), the basement of Sri Lanka has been subdivided into four litho-tectonic units (Cooray, 1994; Kröner et al., 1991). From west to east, they are the Wanni Complex (WC), Kadugannawa Complex (KC), the Highland Complex (HC) and the Vijayan Complex (VC; Figure 1). It is suggested that the Sri Lankan terrains were juxtaposed at an active continental margin setting during the late Neoproterozoic to Cambrian collisional event (c. 500–600 Ma) that formed Gondwana (e.g. Kröner & Williams, 1993; Kriegsman, 1995; Santosh et al., 2014; see review in Malaviarachchi, 2018; Malaviarachchi et al., 2019). Detailed descriptions of the above three Complexes can be found in Santosh et al. (2014), Dharmapriya et al. (2016) and Malaviarachchi (2018).

The HC is composed of granulite facies metaquartzites, marbles, calcsilicates and metapelitic gneisses, intimately associated with charnockites (Cooray, 1962, 1984; Mathavan & Fernando, 2001). The HC was metamorphosed under granulite facies conditions between 610 and 550 Ma during the assembly of the Gondwana continent (Hölzl, Hofmann, Todt, & Kröner, 1994; Kröner et al., 1994). Regionally, metamorphic pressures and temperatures of the HC decrease from 8 to 9 kbar and 800–900°C in the east and southeast to 4.5–6 kbar and 600–700°C in the southwest (Faulhaber & Raith, 1991; Fernando et al., 2017; Kriegsman, 1996; Kriegsman & Schumacher, 1999; Mathavan et al., 1999; Raase & Schenk, 1994; Schumacher & Faulhaber, 1994). Raase and Schenk (1994) proposed that both the southeastern and southwestern parts of the HC represent a deep-crustal slice with the exposed depth changing from ~30 to 35 km in the southeast to 15–20 km in the west. As most thermobarometric results before 1994 reflect P–T points on the cooling path, this suggests that the lower crustal cross-section exposed nowadays in the HC was tilted after initial cooling.

Evidence for UHT metamorphism has been reported only from a few localities in the central Highland Complex (Bolder-Schrijver et al., 2000; Dharmapriya, Malaviarachchi, Galli, et al., 2015; Dharmapriya, Malaviarachchi, Kriegsman, Galli, et al., 2017; Dharmapriya, Malaviarachchi, Kriegsman, Sajeev, et al., 2017; Dharmapriya et al., 2016; Kriegsman & Schumacher, 1999; Malaviarachchi & Dharmapriya, 2015; Osanai, 1989; Osanai et al., 2000, 2006, 2016a, 2016b; Sajeev & Osanai, 2004b; Sajeev et al., 2007, 2009, 2010) and rarely in the southwestern part of the HC (Sajeev & Osanai, 2004a) from pelitic, mafic and quartzo-feldspathic granulites. Estimated UHT conditions range from 900 to 1,150°C at pressures comprised between 9 and 12.5 kbar (Dharmapriya, Malaviarachchi, Galli, et al.,

2015; Dharmapriya, Malaviarachchi, Kriegsman, Galli, et al., 2017; Dharmapriya, Malaviarachchi, Kriegsman, Sajeev, et al., 2017; Dharmapriya et al., 2016; Osanai et al., 2006; Sajeev & Osanai, 2004a, 2004b; Sajeev et al., 2007). Osanai et al. (2006), Malaviarachchi and Dharmapriya (2015) and Dharmapriya, Malaviarachchi, Galli, et al. (2015), have given detailed summaries of the Sri Lankan UHT granulites.

The HC is classically considered as the oldest lithotectonic unit of Sri Lanka, characterized by Nd-model age of 3,400–2,000 Ma (Milisenda et al., 1988, 1994), sediment deposition from 3,500 Ma to 2,000–1,700 Ma (Hölzl et al., 1994; Kröner et al., 1994) and emplacement of most of the granitoid plutons, today exposed as orthogneisses, into already deposited sediments (final deposition of HC sediments prior to c. 2,000 Ma) at 2,000–1,800 Ma and 670 Ma (Hölzl et al., 1994; Kröner et al., 1994; Kröner & Williams, 1993).

Nevertheless, recent advances of geochronological studies revealed the incorporation of Neoproterozoic detrital zircons in UHT and ordinary metasediments (e.g. Dharmapriya, Malaviarachchi, Santosh, et al., 2015; Dharmapriya et al., 2016; He et al., 2015; Kitano et al., 2018; Malaviarachchi et al., 2019; Sajeev et al., 2010; Santosh et al., 2014; Takamura et al., 2016). Sajeev et al. (2010) reported the incorporation of detrital zircons with ages ranging from 2,300 to 830 Ma. Dharmapriya, Malaviarachchi, Santosh, et al. (2015), Dharmapriya et al. (2016) showed the incorporation of detrital zircon with protolith ages from 2,800 to 730 Ma, whereas the metamorphism of the HC took place during 665–510 Ma. Kitano et al. (2015) and Kitano et al. (2018) reported detrital zircon ages of c. 2,700–670 Ma from the southern and southwestern part of the HC with overgrowth zircon rim ages from 660 to 470 Ma. The Mesoproterozoic age peaks observed in zircons at c. 1.6 Ga and c. 1 Ga might reflect the triggering of a subduction event in a palaeotectonic setting forming the Wanni and Vijayan dual arc systems, respectively (Malaviarachchi et al., 2019; Malaviarachchi & Dharmapriya, 2015; Santosh et al., 2014).

The KC, WC and VC rocks (see Dharmapriya, Malaviarachchi, Galli, et al., 2015; Dharmapriya, Malaviarachchi, Santosh, et al., 2015; He et al., 2015, 2016; Santosh et al., 2014 for more details) have yielded Nd-model ages of 1,800–1,000 Ma, 2,000–1,000 Ma and 1,800–1,000 Ma (Milisenda et al., 1988, 1994), respectively. The rocks in these three complexes were metamorphosed under upper amphibolite to granulite facies conditions simultaneous with the assembly of Gondwana (e.g. Cooray, 1994; He et al., 2015, 2016; Hirayama et al., 2020 Kehelpannala, 1997; Kröner et al., 2013; Malaviarachchi et al., 2019; Mathavan et al., 1999; Perera & Kagami, 2011; Ratheesh-Kumar, Dharmapriya, Windley, Xiao, & Jeevan, 2020).

3 | SAMPLE DESCRIPTIONS AND FIELD RELATIONS

Sapphirine-bearing granulites were collected from a quarry site (~1.5 km along the Galatha Road from Gampola Nuwara Eliya Road; 7.130788N, 80.585328E), southwest of Kandy close to Gampola (Figure 1). The composition of this rock varies considerably in macro-scale from place to place (commonly within 1–5 m distance), locally forming different mineral assemblages (hereafter we refer to them as compositional domains, Figure 2). There are four compositional domain types named $Domain_1$, $Domain_2$, $Domain_3$ and $Domain_4$, that were classified according to their mineral assemblages. The detailed descriptions of field relations and sample descriptions and U–Pb geochronology of $Domain_1$ were given by Dharmapriya, Malaviarachchi, Santosh, et al. (2015), whereas $Domain_3$ and $Domain_4$ were described by Dharmapriya, Malaviarachchi, Sajeev and Zhang (2016). These previous studies were mainly aimed at the geochronology of UHT granulites in the HC and P–T estimation for the above three domains involved only using conventional thermobarometric approaches. As for $Domain_2$, we describe its petrography and mineral reactions here for the first time.

The sapphirine-, kyanite- and spinel-bearing cordierite–garnet–orthopyroxene–sillimanite domain ($Domain_1$, Figure 2a,b) was identified where purple cordierite commonly occurs in the symplectite around garnet (Figure 2c) and occasionally in some melt patches (Figure 2d). $Domain_1$ occurs as discontinuous layers or lenses commonly within host sillimanite- and spinel-bearing garnet–orthopyroxene gneiss ($Domain_4$), which is the dominant rock type in the quarry (Dharmapriya, Malaviarachchi, Santosh, et al., 2015). $Domain_1$ comprises porphyroblastic garnet (0.5–2.5 cm in diameter) commonly surrounded by orthopyroxene–cordierite symplectite and/or orthopyroxene–sillimanite moats (Figure 2c). Ribbon quartz (up to 4 cm in length) defines the main lineation and sillimanite needles follow this preferred orientation. Leucosomes with irregular shaped quartz and feldspar, and small biotite flakes and rare coarse-grained cordierite (~1 cm), may have formed during the retrograde evolution (Figure 2d). The estimated length of $Domain_1$ varies from ~1 to 3.5 m and the width varies from ~30 cm to 1 m. However, all margins with $Domain_2$ and $Domain_4$ are gradational.

The sapphirine-bearing garnet–orthopyroxene–sillimanite-rich domains ($Domain_2$) were found in the lower parts of $Domain_1$ without a clear margin (Figure 2a,b,e). The length of $Domain_2$ varies from ~50 cm to 1.5 m and the width from ~25 to 75 cm. These domains usually contain medium to coarse-grained orthopyroxenes (0.2–0.5 cm in diameter; Figure 2e) and the complete absence of cordierite distinguishes it from $Domain_1$. Medium to coarse-grained anhedral to subhedral garnet (0.3–1 cm) is usually surrounded by biotite–plagioclase coronae. The ribbon quartz (0.5–1.5 cm) grains are not as long as those in $Domain_1$. In places, very

coarse-grained anhedral orthopyroxenes (1–3 cm) are concentrated into quartz- and plagioclase-rich leucosome patches (Figure 2e,f). Medium-grained garnets are also present close to these melt patches (Figure 2f).

Sapphirine- and kyanite-bearing garnet–orthopyroxene–sillimanite gneiss ($Domain_3$) shows evidence for relatively strong flattening (Figure 2g,h). The thickness of this domain varies from ~25 to 50 cm and the length varies from ~1.5 to 3 m. Coarse to medium-grained anhedral garnets (0.25–1.5 cm in diameter) are commonly wrapped by ribbons of quartz and feldspar (up to 5 cm in length, Figure 2h). The wavy patterns of the matrix around peritectic garnet could indicate melt loss (Kriegsman, 2001). Garnets are mostly surrounded by biotite–plagioclase and locally by orthopyroxene–sillimanite symplectite. Medium- to coarse-grained anhedral orthopyroxenes (0.20–0.75 cm) are closely associated with garnet or occur as isolated grains in the matrix (Figure 2h). Tiny, disseminated biotite flakes and feldspar-rich irregular nabs in the matrix may have resulted from retrogression. The margins between $Domain_3$ and $Domain_4$ are gradational.

Sillimanite- and spinel-bearing garnet–orthopyroxene-rich compositional domains ($Domain_4$) cover more than 90% of the quarry (Figure 2a). In this study, the samples of this domain were not considered except for Ti-in-zircon thermometry. Compositional domains having gradual variation of mineral paragenesis without sharp contacts in the quarry may reflect a primary heterogeneity of the sediment during deposition (e.g. Dharmapriya, Malaviarachchi, Galli, et al., 2015; Dharmapriya, Malaviarachchi, Kriegsman, Sajeev, et al., 2017).

4 | PETROGRAPHY

Dharmapriya, Malaviarachchi, Santosh, et al. (2015) described some features relevant to the petrography and mineral reactions in $Domain_1$, but here we give a more detailed description of the petrography. Furthermore, here we report the petrography and mineral reactions of $Domain_2$ for the first time with novel findings of textural features. In addition, we present a detailed petrographical description of Domains3 and 4. The mineral abbreviations used in this paper are after Whitney and Evans (2010).

4.1 | $Domain_1$

The subhedral to anhedral porphyroblastic garnets of $Domain_1$ mainly contain sillimanite, biotite, quartz, plagioclase and K-feldspar as major inclusion phases, and Fe-Ti oxides (exsolved titanohematite–ilmenite±rutile) as minor inclusion phases. Sapphirine, kyanite, monazite, zircon and apatite are accessory minerals. Core areas of some garnets
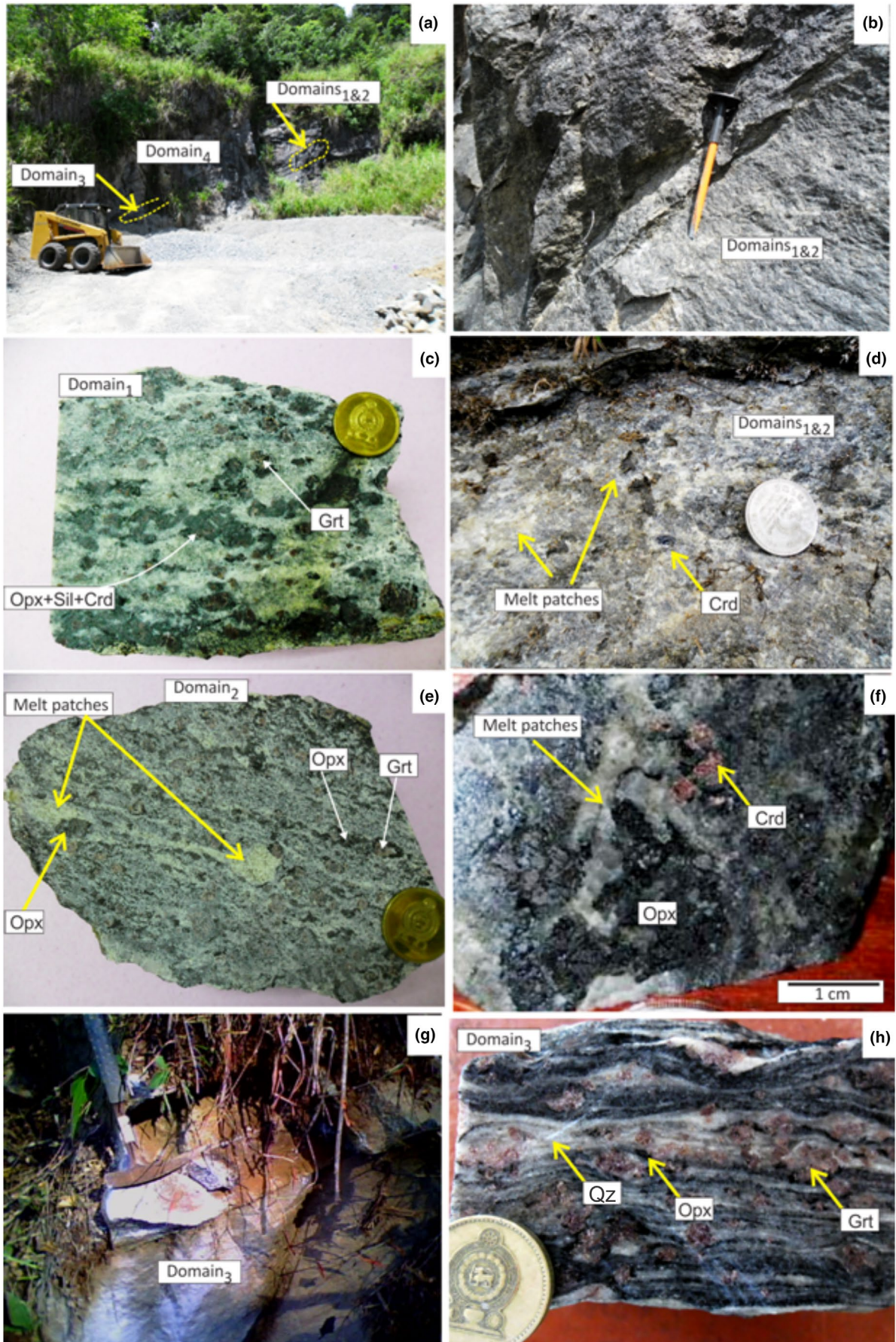
contain coexisting sapphirine and approximately prismatic kyanite (Figure 3a). Kyanite was confirmed using LabRAM HR (UV) micro-Raman analysis (see the figure S1 of Dharmapriya, Malaviarachchi, Santosh, et al., 2015). Quartz and biotite are present as inclusions in the garnet mantle, whereas isolated sillimanite needles are present in the rim of the same garnet (Figure 3a). Most of the garnets contain quartz±biotite±sillimanite inclusions from core to rim.

Garnets are commonly broken down, forming moats and/or symplectitic textures (Figure 3a,b and d–i). Intergrowths of coarse-grained orthopyroxene (0.5–0.75 cm) and medium to coarse-grained prismatic sillimanite (0.2–0.50 cm) occur as moats around garnets (Figure 3b). Orthopyroxene–sillimanite box structures are also present (Figure 3a,b). Anhedral, fine- to medium-grained Fe-Ti oxides mainly of exsolved titano-hematite–ilmenite±rutile are common in the above moats (Figure 3c). Less commonly, matrix quartz coexists with orthopyroxene–sillimanite moats (Figure 3d,e). Vermicular orthopyroxene–cordierite symplectites are present in between orthopyroxene–sillimanite moats and garnet (Figure 3f,g,h). The presence of cordierite among orthopyroxene and sillimanite in these moats is a prominent feature (Figure 3f,g,h,i). Occasionally, relics of quartz and/or plagioclase are present in contact with orthopyroxene and cordierite (Figure 3j,k). Quartz grains are present as inclusion phases in orthopyroxene of the orthopyroxene–sillimanite–cordierite intergrowths. Locally, tiny spinel is present with cordierite in between orthopyroxene and sillimanite (Figure 3l).

The intergrowth of vermicular orthopyroxene and cordierite around garnets frequently contains subrounded magnetite (Figure 3a,f,g,h). Locally, fine-grained sapphirine with spinel inclusions can be observed in the presence of Fe-oxide (magnetite) within orthopyroxene–cordierite symplectite (Figure 3m). Very rarely, some of the garnets are rimmed by an orthopyroxene–plagioclase corona where anhedral, fine-grained sapphirine intergrowths with plagioclase (Figure 3n) are also observed.

The major mineral constituents in the matrix are primatic sillimanite (up to 4 cm in length), ribbon quartz (up to 4 cm in length), subhedral to anhedral plagioclase (0.2–0.75 cm) and K-feldspar (<0.2–0.5 cm). The recrystallized plagioclase and K-feldspar grains are also dominant (Figure 3o). Fine- to medium-grained, anhedral Fe-Ti oxides (mainly exsolved ilmenite–titanohematite±rutile) are present as a minor mineral phase, whereas sapphirine, zircon and monazite exist

as accessory minerals. Medium-grained anhedral sapphirine (~0.25 cm) is associated with (mainly) plagioclase in some microdomains (Figure 3p). These subhedral- to euhedral-shaped plagioclase and cordierite grains with quartz in leucosomes could have crystallized from a melt during retrogression. Anhedral, coarse-grained (up to 1 cm) ternary feldspar is also abundant.

4.2 | Domain₂

Garnet (0.3–1 cm) of this domain is mainly subhedral to anhedral and the matrix consists of biotite, sillimanite and quartz as major mineral constituents, whereas plagioclase, K-feldspar and Fe-Ti oxides (exsolved titanohematite–ilmenite±rutile) occur as minor phases. Sapphirine, zircon, apatite and monazite are present as accessory mineral phases. Medium-grained (up to 0.3 cm) sapphirine is present as isolated inclusions in the core of some garnets (Figure 4a,b). The mantle areas of the same garnets contain inclusions of isolated biotite and quartz rimmed by plagioclase (Figure 4a,b). Locally, sapphirine is located in the core of anhedral garnet, whereas preferredly oriented fibrolitic sillimanite is present only in mantle to rim areas of the same garnet (Figure 4c,d). Biotite inclusions are present throughout some garnets and coarse K-feldspar inclusions are present in the mantle of the same garnet grains (Figure 4c,d). Most of the garnets are rimmed by biotite–plagioclase symplectites (Figure 4e).

In the matrix, plagioclase, orthopyroxene, K-feldspar, ribbon quartz and biotite are present as major mineral constituents together with Fe-Ti oxides (exsolved titanohematite–ilmenite±rutile) and sillimanite as a minor constituent. Zircon, apatite and monazite are found as accessory minerals. Coexistence of porphyroblastic orthopyroxene and prismatic sillimanite can also be observed (Figure 4f–l). In some domains, anhedral, coarse orthopyroxene is intergrown with prismatic sillimanite (Figure 4f,g) coexisting with matrix quartz (Figure 4f,g). Locally, such intergrowths involve fibrolitic sillimanite (Figure 4f). In some domains, coarse orthopyroxene grains coexist with clusters of oriented sillimanite and matrix quartz (Figure 4h–l). Anhedral coarse-grained orthopyroxenes are also present in irregular quartz and plagioclase-rich melt patches (Figure 4m,n). Some of the porphyroblastic orthopyroxenes are overprinted by biotite (Figure 4n).

FIGURE 2 Samples and field relations: (a) the quarry in which samples of sap. phirine-bearing granulites were collected. The yellow dashed lines demarcate the approximate margins of Domain₁, Domain₂ and Domain₃ within host Domain₄; (b) closed view of the quarry from which Domain1 and Domain₂ samples were collected; (c) a hand specimen of Domain₁; (d) closer view of Domain₁ where quartz- and feldspar-rich melt patches are abundance; coarse grain purple colour cordierites are also present; (e) a hand specimen of Domain₂; (f) a closer view of a melt patch of Domain₂; (g) closer view of the quarry from which the samples of Domain₃ were collected; (h) a hand specimen of Domain₃ showing wavy patterns around peritectic garnet, indicating melt loss [Colour figure can be viewed at wileyonlinelibrary.com]
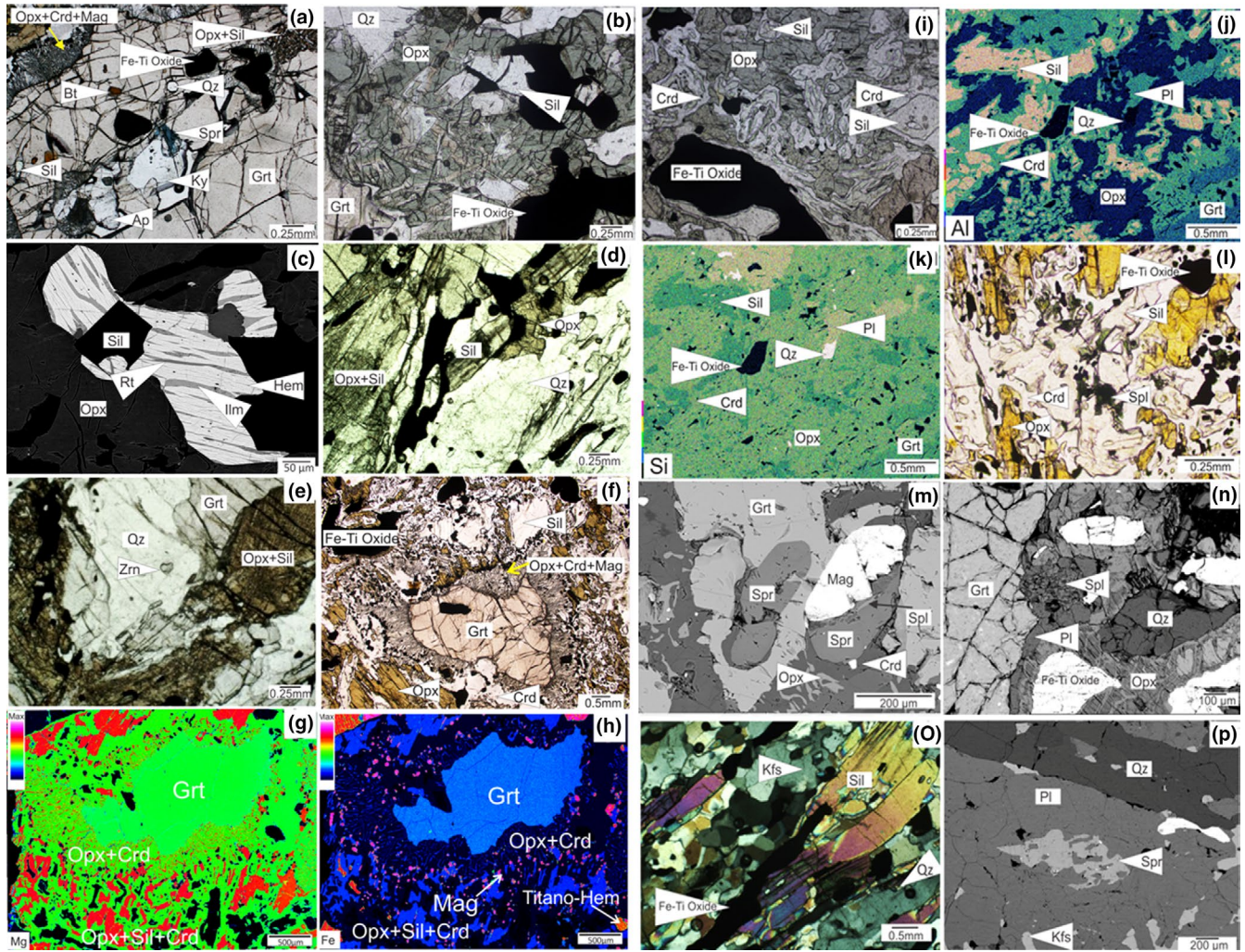
FIGURE 3 Photomicrographs showing textures of Domain₁: (a) garnet with sapphirine, sillimanite, kyanite and biotite as major inclusion phases and the coexistence of sapphirine and kyanite at the core area; (b) intergrowth of coarse-grained orthopyroxene and sillimanite after garnet; (c) BSE image of exsolved titanohematite–ilmenite±rutile in coarse-grained orthopyroxene and sillimanite intergrowth; (d) and (e) coexisting quartz with orthopyroxene and sillimanite after garnet; (f) vermicular orthopyroxene–cordierite symplectite between garnet and intergrowth of coarse-grained orthopyroxene and sillimanite; (g) and (h) wavelength dispersive (WDS) X-ray element maps of garnet and garnet breakdown reaction textures (Fe distribution map (g) and Mg map distribution map [h]); (i) formation of cordierite between orthopyroxene and sillimanite in coarse-grained orthopyroxene and sillimanite as intergrowths; (j) and (k) energy dispersive (EDS) X-ray map of intergrowths of coarse-grained orthopyroxene–sillimanite–cordierite moats. Tiny quartz is also present [Al distribution map (j) and Si distribution map (k)]; (l) small spinel grains at the margins of sillimanite in the orthopyroxene–sillimanite–cordierite moats; (m) BSE image of image showing coexistence of sapphirine and magnetite within orthopyroxene–cordierite symplectite, and a local tiny spinel; (n) BSE image showing sapphirine–plagioclase intergrowth in plagioclase–orthopyroxene moat around garnet; (o) matrix minerals (oriented sillimanite needles also present); (p) BSE image showing medium grained anhedral sapphirine surrounded by plagioclase in the matrix [Colour figure can be viewed at wileyonlinelibrary.com]

4.3 | Domain₃

Garnet (0.25–1 cm) in this domain mainly contains sillimanite, quartz and plagioclase as major mineral phases, whereas biotite and Fe-Ti oxides (exsolved titanohematite–ilmenite±rutile) are minor mineral constituents. Sapphirine, kyanite, rutile, zircon, apatite, and monazite exist as accessory mineral phases. The assemblage sapphirine+kyanite is present in the core area of some garnets (Figure 5a,b). Kyanite was confirmed using LabRAM HR (UV) micro-Raman analysis

(see the figure S3 of Dharmapriya et al., 2016). Biotite and quartz are present as isolated inclusions in the rim of the same garnet (Figure 5a). Garnets contain sillimanite, quartz and biotite inclusions from core to rim (Figure 5c). Locally, garnets have broken down forming orthopyroxene–sillimanite coronae (Figure 5d) or biotite–plagioclase coronae (Figure 5e).

The matrix mainly contains ribbon quartz (up to 6 cm), recrystallized plagioclase and K-feldspar as major constituents, whereas biotite and Fe-Ti oxides (exsolved titanohematite–ilmenite±rutile) occur as minor minerals. Zircon
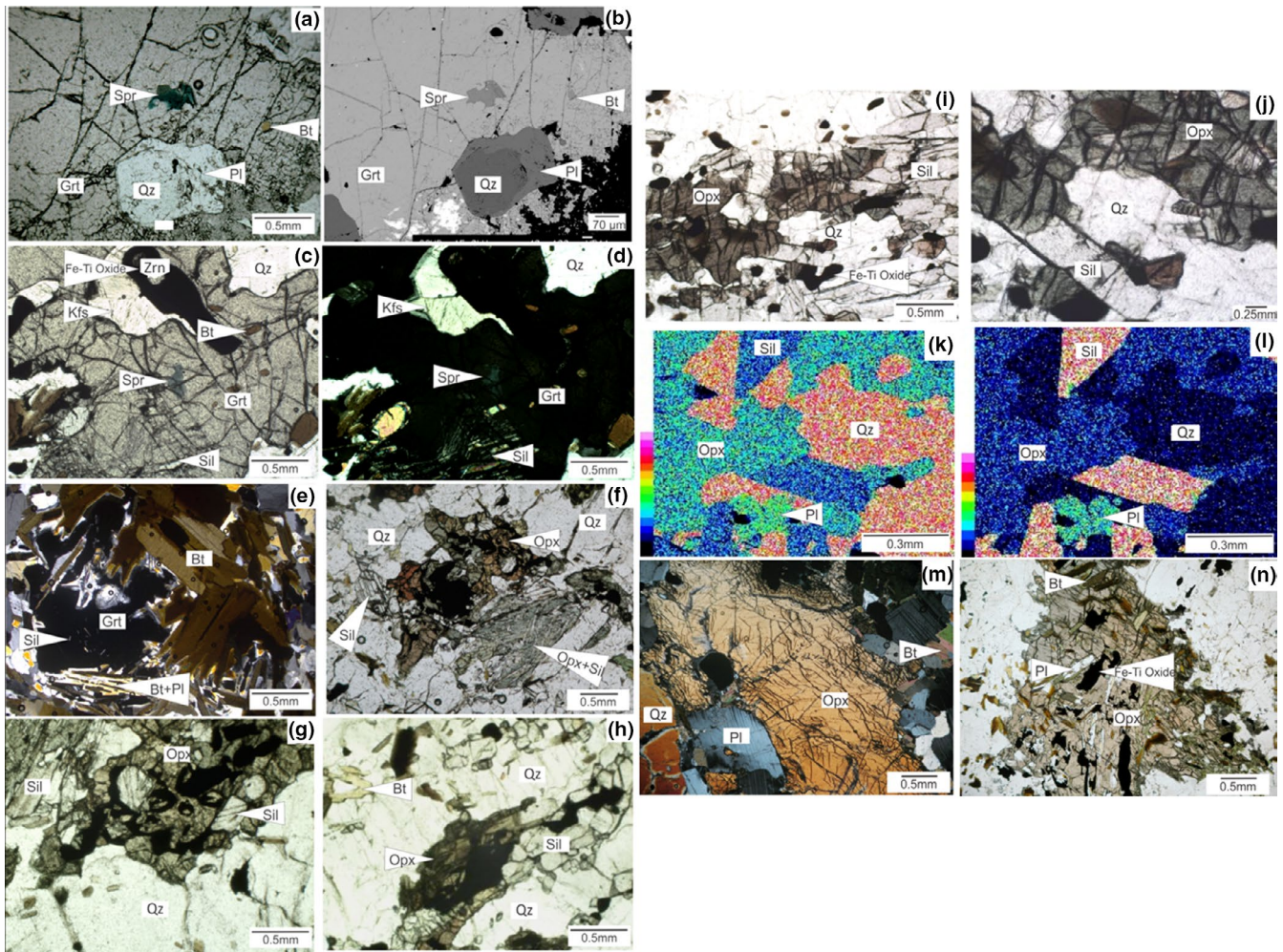
FIGURE 4 Photomicrographs showing textures of Domain$_2$. (a) sapphirine is present as isolated inclusions in the core of some garnets; (b) BSE image sapphirine is present as isolated inclusions in the core of some garnets; (c) plane polarized light (PPL) view: sapphirine is located in the core of anhedral garnet, whereas preferredly oriented fibrolitic sillimanite is present only in mantle to rim areas of the same garnet; (d) cross polarized light view (CPL) of image (c); (e) garnets are rimmed by biotite–plagioclase symplectites; (f), (g), (h), (i) and (j) coexistence of orthopyroxene+sillimanite+quartz in the matrix; (k) EDS map of Si of image (j); (l) EDS map of Al of image (j); coarse orthopyroxene in the matrix; (n) coarse orthopyroxene containing plagioclase inclusions in the matrix [Colour figure can be viewed at wileyonlinelibrary.com]

and monazites are present as accessories, and sillimanite is notably absent. Porphyroblastic orthopyroxene locally co-exists with garnet (Figure 5f). Some of the porphyroblastic orthopyroxene grains have been overprinted by late biotite and quartz in the presence of K-feldspars (Figure 5g). The ribbon quartz demarcates the major lineation (Figure 5h) and commonly wraps around garnet.

5 | MINERAL CHEMISTRY AND WHOLE-ROCK CHEMISTRY

5.1 | Mineral chemistry

Mineral compositions were analysed using JEOL JXA8530 Field Emission Electron Probe Microanalyzers (FE-EPMA)

installed at five different institutions. Analytical methods and standards at each laboratory are given in Appendix S1. The Fe^{2+} and Fe^{3+} contents of garnet, orthopyroxene, spinel and sapphirine were calculated based on charge balance using the method by Droop (1987).

5.1.1 | Garnet

Garnet porphyroblasts in all samples are mainly almandine–pyrope solid solution (Table 1). Their core compositions are $Alm_{41–47}Prp_{46–55}Grs_{2–3}Spe_{1–3}$ (mol.%), and their rim compositions are quite similar, $Alm_{40–47}Prp_{48–56}Grs_{1.5–2.5}Spe_{1–2}$ (mol.%). The Fe and Mg X-ray maps of garnet in Domain$_1$ show homogeneous Fe and Mg contents from core to rim (Figure 3g,h).
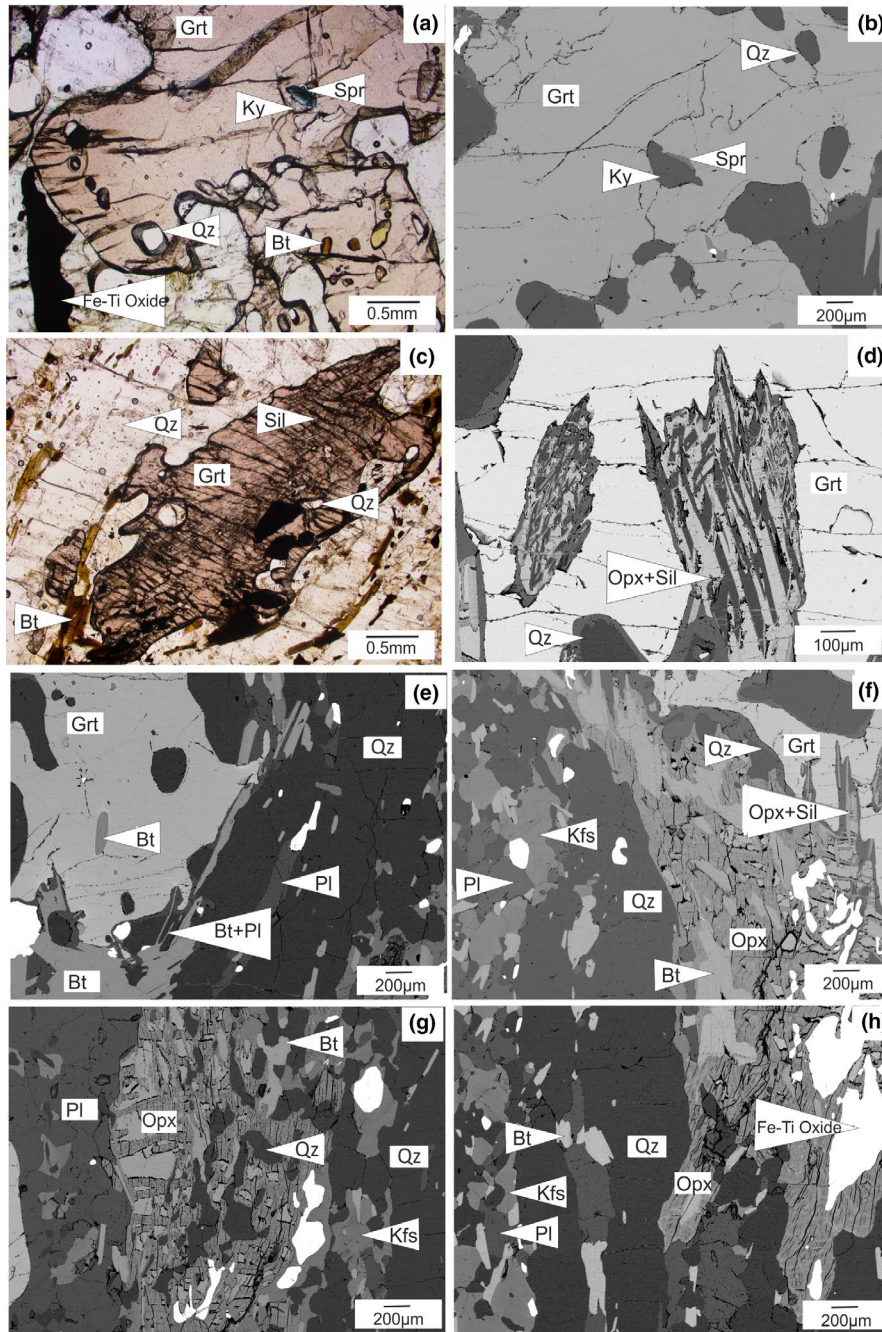
FIGURE 5 Photomicrographs showing textures of Domain$_3$: (a) coexistence of kyanite–sapphirine at the core; (b) BSE image of (a); (c) fibrolitic sillimanite and quartz inclusions in garnet; (d) intergrowth of sillimanite–orthopyroxene at rim of garnet; (e) biotite–plagioclase corona at the rim of garnet; (f) coarse-grained orthopyroxene adjacent to garnet. Intergrowth of sillimanite–orthopyroxene at rim of garnet can also be identified; (g) quartz, biotite and K-feldspar overgrowth on orthopyroxene; (h) BSE image showing elongated quartz in the matrix [Colour figure can be viewed at wileyonlinelibrary. com]

5.1.2 | Orthopyroxene

Orthopyroxene compositions vary with the textural setting (Table 2). In Domain$_1$ and Domain$_3$, orthopyroxenes intergrown with prismatic sillimanite around garnets preserve the highest Al$_2$O$_3$ contents (up to 9.00 wt%), with X_{Mg} ~ 0.7. The Al$_2$O$_3$ content of porphyroblastic orthopyroxene in Domain$_2$ is slightly lower (8.4 wt%, with X_{Mg} ~ 0.7). Vermicular orthopyroxene in orthopyroxene–cordierite symplectites around garnet in Domain$_1$ (Table 2) contains intermediate Al$_2$O$_3$ content of ~6.5 wt% with X_{Mg} ~ 0.7.

5.1.3 | Biotite

Biotite contains a high TiO$_2$ content from ~4.4 to ~6.8 wt%. The Ti content of the matrix biotite is slightly higher in all domains (Table 2). The F content of the biotite inclusions in garnet is in the range of 0.7–1.0 wt% and the biotites in the matrix are in the range of 0.5–0.9 wt%. The Cl content is uniformly low (~0.01–0.1 wt%). The X_{Mg} value is relatively higher in biotite inclusions within garnet (X_{Mg} 0.75–0.85) compared to biotite in the matrix of all the samples (X_{Mg} 0.70–0.75), which may indicate retrograde

TABLE 1 Representative electron microprobe analysis of garnet

	Domain 1			Domain 2			Domain 3		
SiO_2	39.54	39.36	39.89	39.83	40.07	39.84	40.39	40.19	40.16
TiO_2	0.00	0.05	0.03	0.01	0.00	0.04	0.00	0.04	0.03
Al_2O_3	22.93	22.78	22.56	22.52	22.51	22.48	22.19	22.64	22.50
Cr_2O_3	0.00	0.02	0.02	0.52	0.17	0.09	0.01	0.05	0.01
FeO	23.06	23.38	23.01	21.57	21.51	21.89	21.07	21.20	22.48
MnO	1.49	1.33	1.13	0.63	0.66	0.69	0.79	0.66	0.75
MgO	12.28	12.72	12.74	14.61	14.58	14.87	14.46	14.49	13.70
CaO	1.47	1.18	1.06	0.84	1.06	0.81	1.38	1.36	0.94
Na_2O	0.01	0.00	0.03	0.00	0.00	0.01	0.00	0.02	0.02
K_2O	0.00	0.00	0.00	0.00	0.02	0.00	0.00	0.03	0.00
Total	100.76	100.82	100.47	100.53	100.58	100.72	100.29	100.66	100.60
O	12	12	12	12	12	12	12	12	12
Si	2.97	2.95	2.99	2.96	2.98	2.96	3.00	2.98	2.99
Ti	0.00	0.00	0.00	0.00	0.00	0.00	0.00	0.00	0.00
Al	2.03	2.01	1.99	1.97	1.97	1.97	1.95	1.98	1.98
Cr	0.00	0.00	0.00	0.03	0.01	0.01	0.00	0.00	0.00
Fe	1.45	1.47	1.44	1.34	1.34	1.36	1.31	1.31	1.40
Mn	0.09	0.08	0.07	0.04	0.04	0.04	0.05	0.04	0.05
Mg	1.37	1.42	1.42	1.62	1.61	1.65	1.60	1.60	1.52
Ca	0.12	0.10	0.09	0.07	0.09	0.06	0.11	0.11	0.08
Na	0.00	0.00	0.00	0.00	0.00	0.00	0.00	0.00	0.000
K	0.00	0.00	0.00	0.00	0.00	0.00	0.00	0.00	0.00
Tot. cation	8.02	8.04	8.01	8.04	8.03	8.05	8.02	8.03	8.02
Fe^{3+}	0.07	0.11	0.04	0.11	0.10	0.15	0.07	0.09	0.06
Fe^{2+}	1.38	1.35	1.40	1.24	1.23	1.21	1.24	1.22	1.34
Alm	0.47	0.46	0.47	0.42	0.42	0.41	0.41	0.41	0.45
Spe	0.03	0.03	0.02	0.01	0.01	0.02	0.02	0.01	0.02
Prp	0.46	0.48	0.48	0.55	0.54	0.56	0.53	0.54	0.51
Grs	0.04	0.03	0.03	0.02	0.03	0.02	0.04	0.04	0.03
X_{Mg}	0.49	0.49	0.50	0.55	0.55	0.55	0.55	0.55	0.52

Fe-Mg exchange between biotite inclusions and their garnet hosts. All biotites gave oxide totals in between 97–98 wt%. The totals exceed 100% when assuming full hydration, which indicates some hydrogen deficiency (e.g. Cesare et al., 2003).

5.1.4 | Sapphirine

The Al_2O_3 content of sapphirine in the rock (Table 3) varies from 58.5 to 60.5 wt%. Sapphirine compositions are between end-member compositions 2:2:1 ($2MgO. 2Al_2O_3. SiO_2$) and 7:9:3 ($7MgO. 9Al_2O_3. 3SiO_2$). The X_{Mg} value varies from 0.71 to 0.76 (Table 3). Calculated Fe^{3+} of all sapphirines (based on charge balance) is less than 0.275 a.p.f.u. (O_{10} basis).

5.1.5 | Spinel

Spinel from the studied granulites contains a considerable amount of ZnO (~2.0 wt%, Table 3). The X_{Mg} of spinel within orthopyroxene–sillimanite–cordierite intergrowths in $Domain_1$ is ~0.50, whereas it is 0.64 for the spinel inclusions within sapphirine.

5.1.6 | Cordierite

Cordierite porphyroblasts present in melt patches in $Domain_1$ (Table 4) have an X_{Mg} of 0.86. Cordierite in orthopyroxene–cordierite symplectites in $Domain_1$ (Table 4), as well as cordierite between coarse-grained orthopyroxene–sillimanite intergrowth in $Domain_1$, have an X_{Mg} ~0.90.

TABLE 2 Representative electron microprobe analysis of orthopyroxene and biotite

	Opx								Bt					
	Domain1			Domain2			Domain3		Domain1		Domain2		Domain3	
	Opx-Sil Co*		Sy**	Coarse-Mt***		In Melt#	Sy***	Mt*#	Grt##	Mt***#	Grt##	Sy***	Grt##	Mt***#
	Core	Rim		Core	Rim									
SiO$_2$	49.51	49.84	50.76	48.52	48.80	49.32	49.78	49.62	37.97	37.73	39.18	38.22	38.68	38.87
TiO$_2$	0.12	0.05	0.06	0.02	0.00	0.11	0.04	0.08	5.01	6.15	4.49	4.56	4.11	4.41
Al$_2$O$_3$	8.99	8.28	6.65	8.43	8.22	7.47	8.91	8.53	16.34	15.32	16.69	16.39	17.55	16.30
Cr$_2$O$_3$	0.00	0.01	0.03	0.04	0.07	0.07	0.03	0.07	0.03	0.07	0.00	0.01	0.06	0.08
FeO	18.00	17.33	17.60	18.02	18.19	18.46	16.93	18.06	9.02	12.72	6.49	10.09	6.97	10.34
MnO	0.43	0.43	0.46	0.14	0.18	0.52	0.13	0.22	0.07	0.00	0.03	0.00	0.00	0.00
MgO	23.65	24.42	24.74	24.04	24.27	24.18	24.94	23.71	18.01	15.21	19.37	17.19	18.93	17.12
CaO	0.08	0.08	0.07	0.02	0.02	0.07	0.04	0.06	0.00	0.01	0.08	0.02	0.01	0.06
Na$_2$O	0.01	0.01	0.00	0.00	0.00	0.04	0.03	0.01	0.09	0.05	0.42	0.23	0.43	0.20
K$_2$O	0.00	0.00	0.01	0.00	0.00	0.01	0.00	0.01	9.78	9.98	9.37	9.53	9.72	9.71
F									0.73	0.52	0.00	0.96	1.05	0.95
Cl									0.05	0.08	0.03	0.03	0.02	0.02
Total	100.78	100.45	100.38	99.23	99.75	100.25	100.83	100.36	97.09	97.82	96.14	97.22	97.52	98.05
O	6	6	6	6	6	6	6	6	22	22	22	22	22	22
Si	1.79	1.80	1.84	1.79	1.79	1.80	1.79	1.80	5.45	5.48	5.55	5.51	5.48	5.56
Ti	0.00	0.00	0.00	0.00	0.00	0.00	0.00	0.00	0.54	0.67	0.48	0.49	0.44	0.47
Al	0.38	0.35	0.28	0.37	0.36	0.32	0.38	0.37	2.78	2.62	2.79	2.78	2.93	2.75
Cr	0.00	0.00	0.00	0.00	0.00	0.00	0.00	0.00	0.00	0.01	0.00	0.00	0.01	0.01
Fe	0.54	0.53	0.53	0.56	0.56	0.57	0.51	0.55	1.08	1.54	0.77	1.22	0.83	1.24
Mn	0.01	0.013	0.01	0.00	0.01	0.02	0.00	0.01	0.01	0.00	0.00	0.00	0.00	0.00
Mg	1.28	1.32	1.34	1.32	1.33	1.32	1.34	1.28	3.86	3.29	4.09	3.69	4.00	3.65
Ca	0.00	0.00	0.00	0.00	0.00	0.00	0.00	0.00	0.00	0.00	0.01	0.00	0.00	0.01
Na	0.00	0.00	0.00	0.00	0.00	0.00	0.00	0.00	0.02	0.01	0.12	0.07	0.12	0.05
K	0.00	0.00	0.00	0.00	0.00	0.00	0.00	0.00	1.79	1.85	1.69	1.75	1.76	1.77
F									0.33	0.24	0.00	0.44	0.47	0.43
Cl									0.01	0.02	0.01	0.01	0.00	0.01
Tot. cation	4.01	4.02	4.02	4.03	4.03	4.03	4.02	4.01	15.53	15.47	15.48	15.51	15.55	15.50

(Continues)

TABLE 2 (Continued)

	Opx								Bt					
	Domain1			Domain2			Domain3		Domain1	Domain2		Domain3		
	Opx-Sil Co*		Sy**	Coarse-Mt***		In Melt#	Sy**	Mt*#	Grt##	Mt**#	Grt##	Sy***	Grt##	Mt**#
	Core	Rim		Core	Rim									
Fe³⁺	0.04	0.05	0.05	0.09	0.10	0.10	0.06	0.04						
Fe²⁺	0.50	0.47	0.49	0.46	0.45	0.46	0.44	0.51						
X_{Al}	0.19	0.18	0.14	0.18	0.18	0.16	0.19	0.18						
X_{Mg}	0.70	0.72	0.72	0.70	0.70	0.70	0.72	0.70	0.78	0.68	0.84	0.75	0.83	0.75

Opx-Sil Co*—orthopyroxene-sillimanite corona; Sy**—in orthopyroxene-sillimanite symplectite; Coarse-Mt***—coarse orthopyroxene grains associated with orthopyroxene+sillimanite+quartz assemblage in the matrix; In Melt#—coarse anhedral orthopyroxene grains in the malt patches; Mt*#—matrix orthopyroxene; Grt##—biotite inclusions in garnet; **Mt**#- biotite in the matrix; Sy***—biotite in plagioclase-biotite symplectites.

5.1.7 | Feldspars

Plagioclases in all samples are dominated by the albite component (Ab_{65-80}) and K-feldspars are dominantly orthoclase (Or_{79-98}). Feldspar compositions of the samples are shown in Table 4.

5.2 | Whole-Rock Chemistry

The procedure followed to obtain the XRF whole-rock major element geochemistry is described in Appendix S1. The results are shown in Table 5. In pseudosections, the P_2O_5 has been removed from the calculations, and the CaO content equivalent to apatite has been subtracted from the measured bulk composition.

Domain$_1$ and Domain$_2$ contain a moderate SiO_2 content of ~55 wt% (~S/SFM = 50) and FeO ~14 wt%, whereas Domain$_3$ is SiO_2-richer at ~70 wt% (~S/SFM = 70) and shows relatively low FeO at ~7 wt%. Also, the TiO_2 content of the first two domains are 2 and 2.5 wt%, respectively, whereas it is ~1 wt% in Domain$_3$. Domain$_1$ shows moderate Al_2O_3 content at ~17wt% (A/AFM = 19), whereas Domain$_2$ and Domain$_3$ display lower Al_2O_3 of ~12 wt% (with varying A/AFM = 9 and 18, respectively). The X_{Mg} value of Domain$_1$ is 0.4 and of Domain$_2$ and Domain$_3$ ~0.5. The CaO, Na_2O and K_2O content of the different domains are in the ranges 1–2 wt%, 2–2.5 wt% and 1.7–3.2 wt%, respectively.

6 | MINERAL REACTIONS AND TEXTURAL EVOLUTION

6.1 | Prograde reaction textures and peak metamorphism

The coexistence of sapphirine+kyanite in the core area of garnet in Domain$_1$ (Figure 3a) and Domain$_3$ (Figure 5a,b) may be attributed to breakdown of staurolite, which is a common mineral in meta-sedimentary rocks subjected to Barrovian-type metamorphism (e.g. Schreyer et al., 1984). Hence, the absence of staurolite could indicate its complete consumption during reaction progress (Dharmapriya, Malaviarachchi, Kriegsman, Sajeev, et al., 2017; Dharmapriya et al., 2016; Dharmapriya, Malaviarachchi, Santosh, et al., 2015). The model prograde reaction is

$$Mg-rich\ St = Grt + Ky + Spr + V \qquad (1)$$
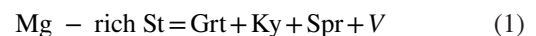
which operates under silica-deficient conditions. The presence of isolated inclusions of quartz, biotite and sillimanite in the area between the mantle and rim of the same garnets and from core to rim in most other garnets of Domain$_1$

TABLE 3 Representative electron microprobe analysis of sapphirine and spinel

	In-Grt*(In)	Matrix(Ku)	Matrix(Ku)	Spr-Pl**(Ch)	Spr-Pl**(Ch)	Spr-Spl#(Tu)	Spr-Spl#(Tu)	In-Grt*(Ch)	In-Grt*(Ch)	In-Grt*(Ku)	In-Grt*(Ku)	Opx-Crd-Spl^(Ku)	Spr-Spl#(Tu)
SiO_2	13.24	13.57	13.55	12.89	13.00	12.72	12.98	13.39	13.42	12.79	13.27	0.03	0.15
TiO_2	0.07	0.06	0.08	0.17	0.14	0.03	0.01	0.00	0.10	0.06	0.05	0.05	0.15
Al_2O_3	60.45	58.53	58.43	58.99	59.49	59.83	58.67	60.39	59.89	60.21	60.31	62.81	66.70
Cr_2O_3	0.11	0.08	0.10	0.32	0.28	0.13	0.23	0.25	0.30	0.06	0.08	0.08	0.67
FeO	9.48	11.00	11.79	10.21	9.96	11.24	11.34	10.26	10.34	9.40	10.03	22.36	15.50
MnO	0.04	0.08	0.05	0.03	0.05	0.09	0.07	0.06	0.05	0.08	0.06	0.23	0.00
MgO	16.61	15.94	15.81	16.20	16.50	15.95	16.02	16.34	16.22	16.73	16.12	12.81	15.80
CaO	0.01	0.04	0.01	0.03	0.02	0.00	0.00	0.07	0.06	0.01	0.01	0.00	0.00
Na_2O	0.04	0.03	0.03	0.00	0.00	0.00	0.00	0.01	0.00	b.d.l	0.04	0.00	0.00
K_2O	0.00	0.00	0.01	0.00	0.00	0.00	0.00	0.00	0.00	0.01	0.00	0.00	0.00
ZnO		0.00	0.00	0.00	0.00	0.00	0.00	0.00	0.00	0.00	0.00	2.01	2.09
Total	100.05	99.33	99.86	98.84	99.44	99.99	99.32	100.78	100.38	99.34	99.97	100.38	101.12
O	10	10	10	10	10	10	10	10	10	10	10	4	4
Si	0.80	0.83	0.83	0.79	0.79	0.77	0.79	0.80	0.81	0.78	0.80	0.00	0.00
Ti	0.00	0.00	0.00	0.01	0.01	0.00	0.00	0.00	0.01	0.00	0.00	0.00	0.00
Al	4.28	4.21	4.20	4.25	4.26	4.28	4.23	4.26	4.25	4.30	4.29	1.96	2.00
Cr	0.01	0.00	0.01	0.02	0.01	0.01	0.01	0.01	0.01	0.00	0.00	0.00	0.01
Fe	0.48	0.56	0.60	0.52	0.51	0.57	0.58	0.51	0.52	0.48	0.51	0.50	0.33
Mn	0.00	0.00	0.00	0.00	0.00	0.00	0.00	0.00	0.00	0.00	0.00	0.01	0.00
Mg	1.49	1.45	1.44	1.48	1.49	1.44	1.46	1.46	1.46	1.51	1.45	0.51	0.60
Ca	0.00	0.00	0.00	0.00	0.00	0.00	0.00	0.00	0.00	0.00	0.00	0.01	0.00
Na	0.01	0.00	0.00	0.00	0.00	0.00	0.00	0.00	0.00	0.00	0.01	0.00	0.00
K	b.d.l	0.00	0.00	0.00	0.00	0.00	0.00	0.00	0.00	0.00	0.00	0.00	0.00
Zn		0.00	0.00	0.00	0.00	0.00	0.00	0.00	0.00	0.00	0.00	0.04	0.04
Total cation	7.06	7.07	7.07	7.07	7.07	7.08	7.08	7.06	7.06	7.07	7.06	3.02	2.99
Al^{IV}	2.21	2.18	2.18	2.22	2.22	2.24	2.22	2.20	2.20	2.23	2.21		
Al^{VI}	2.07	2.03	2.01	2.04	2.04	2.05	2.02	2.06	2.05	2.07	2.08		
Fe^{3+}	0.17	0.19	0.21	0.21	0.20	0.24	0.24	0.17	0.16	0.21	0.16	0.04	0.00
Fe^{2+}	0.31	0.37	0.39	0.39	0.31	0.33	0.34	0.34	0.36	0.27	0.35	0.46	0.33
X_{Mg}	0.76	0.72	0.71	0.74	0.75	0.72	0.72	0.74	0.74	0.76	0.74	0.33	0.64

In-Grt*(In)—inclusion in garnet (analysis at the Center for EarthSciences, Indian Institute of Science, Bangalore, India); In-Grt*(Ku)—inclusion in garnet (analysis at the Division of Earth Sciences, Department of Environmental Changes, Faculty of Social and Cultural Studies, Kyushu University, Japan); Spr-Pl*(Ku)——in sapphirineplagioclase intergrowth (analysis at the Institute of Geology and Geophysics, Chinese Academy of Sciences, Beijing, China); Spr-Spl# (Tu)——spinel inclusion bearing sapphirine(analysis at the Chemical Analysis Division of the Research Facility Centre for Science and Technology, the University of Tsukuba, Japan); Opx-Crd-Spl^(Ku)——orthopyroxene–cordierite–spinel intergrowth (analysis at the Division of Earth Sciences, Department of Environmental Changes, Faculty of Social and Cultural Studies, Kyushu University, Japan).

TABLE 4 Representative electron microprobe analysis of cordierite, plagioclase and K-feldspar

	Crd Domain 1			Pl Domain 1				Pl Domain 2			Pl Domain 3			Kfs Domain 1	Kfs Domain 2	Kfs Domain 3
				In-Grt	Ar-Spr	Spr-PL	Mt	Mt	Melt	Bt-Pl	In-Grt	Mt	Bt-Pl			
SiO$_2$	50.26	50.72	50.49	61.68	62.21	63.95	63.66	62.41	62.664	61.58	63.70	63.36	64.18	64.32	63.95	63.66
TiO$_2$	0.00	0.00	0.00	0.01	0.00	0.00	0.05	0.00	0.00	0.01	0.00	0.01	0.00	0.03	0.00	0.05
Al$_2$O$_3$	33.35	33.34	33.53	23.78	23.97	18.90	18.60	23.07	22.328	23.69	22.63	22.95	23.10	18.44	18.90	18.60
Cr$_2$O$_3$	0.02	0.00	0.00	0.00	0.10	0.06	0.02	0.00	0.068	0.00	0.01	0.04	0.01	0.00	0.06	0.02
FeO	3.4	2.57	2.52	0.20	0.30	0.07	0.03	0.04	0.082	0.33	0.20	0.07	0.11	0.00	0.07	0.03
MnO	0.04	0.02	0.12	0.03	0.04	0.00	0.02	0.00	0.028	0.02	0.00	0.00	0.04	0.01	0.00	0.02
MgO	11.74	12.1	12.04	0.00	0.06	0.01	0.00	0.01	0.00	0.00	0.00	0.04	0.00	0.00	0.01	0.00
CaO	0.01	0.02	0.03	5.19	6.36	0.19	0.12	4.97	3.947	5.32	4.11	4.30	4.35	0.11	0.19	0.12
Na$_2$O	0.02	0.00	0.00	9.01	5.79	2.22	1.24	8.85	9.561	8.83	9.60	9.07	9.24	1.31	2.22	1.24
K$_2$O	0.01	0.01	0.00	0.19	0.28	13.47	14.86	0.22	0.172	0.24	0.11	0.39	0.20	14.60	13.47	14.86
Total	98.85	98.79	98.73	100.09	99.11	98.86	98.59	99.57	98.85	100.02	100.37	100.23	101.22	98.82	98.86	98.59
O	18	18	18	8	8	8	8	8	8	8	8	8	8	8	8	8
Si	5.03	5.05	5.04	2.74	2.77	2.97	2.98	2.78	2.81	2.74	2.81	2.80	2.81	2.99	2.97	2.98
Ti	0.00	0.00	0.00	0.00	0.00	0.00	0.00	0.00	0.00	0.00	0.00	0.00	0.00	0.00	0.00	0.00
Al	3.93	3.92	3.94	1.25	1.26	1.03	1.03	1.21	1.18	1.24	1.18	1.20	1.19	1.01	1.03	1.03
Cr	0.00	0.00	0.00	0.00	0.00	0.00	0.00	0.00	0.00	0.00	0.00	0.00	0.00	0.00	0.00	0.00
Fe	0.29	0.22	0.21	0.01	0.01	0.00	0.00	0.00	0.00	0.01	0.01	0.00	0.00	0.00	0.00	0.00
Mn	0.00	0.00	0.01	0.00	0.00	0.00	0.00	0.00	0.00	0.00	0.00	0.00	0.00	0.00	0.00	0.00
Mg	1.75	1.80	1.79	0.00	0.00	0.00	0.00	0.00	0.00	0.00	0.00	0.00	0.00	0.00	0.00	0.00
Ca	0.00	0.00	0.00	0.25	0.30	0.01	0.01	0.24	0.18	0.25	0.19	0.20	0.20	0.00	0.01	0.01
Na	0.00	0.00	0.00	0.78	0.50	0.20	0.113	0.764	0.8	0.76	0.82	0.78	0.78	0.12	0.20	0.113
K	0.00	0.00	0.00	0.01	0.02	0.80	0.89	0.00	0.01	0.01	0.07	0.02	0.01	0.87	0.80	0.89
Total cation	11.01	10.99	10.99	5.03	4.86	5.01	5.01	5.00	5.02	5.03	5.02	5.00	5.00	4.99	5.01	5.01
An				0.24	0.37	0.01	0.01	0.23	0.18	0.25	0.19	0.20	0.20	0.01	0.01	0.01
Ab				0.75	0.61	0.20	0.11	0.75	0.81	0.74	0.80	0.78	0.79	0.12	0.20	0.11
Or				0.01	0.02	0.79	0.88	0.01	0.01	0.01	0.01	0.02	0.01	0.88	0.79	0.88

Melt1—cordierite in the melt patches; Opx-Crd2—cordierite in orthopyroxene–cordierite symplectite after garnet; Opx-Sil3—cordierite film among orthopyroxene nd sillimanite in orthopyroxene+sillimanite moat after garnet; In-Grt^—inclusion in garnet; In-Spr*—around medium grained sapphirine in the matrix; Spr-Pl*#—in the sapphirine–plagioclase intergrowth; Mt*—in the matrix; Bt-Pl#*—in biotite–plagioclase corona after garnet.

TABLE 5 Representative XRF bulk chemical compositions of different domains

	Domain 1	Domain 2	Domain 3
SiO_2	53.10	54.05	70.86
TiO_2	2.03	2.50	0.83
Al_2O_3	17.50	12.78	12.01
FeO	13.95	14.53	6.74
MnO	0.14	0.16	0.09
MgO	4.95	9.01	3.65
CaO	1.45	1.87	0.98
Na_2O	2.32	1.95	2.02
K_2O	3.21	1.66	2.55
Cr_2O_3	0.03	0.02	0.02
P_2O_5	0.15	0.37	0.06
H_2O	1.28	0.96	0.27
Total	100.10	99.87	100.08
X_{Mg}	0.39	0.52	0.49

(Figure 3a) may be explained by the prograde dehydration melting reaction,

$$Bt + Sil + Qz = Grt + Kfs + Melt \qquad (2)$$

under silica-saturated conditions. Hence, although the matrix of $Domain_1$ is silica saturated, inclusion phases in some garnets represent textural evidence for both silica-deficient and silica-saturated reaction domains during the growth of garnets. Dharmapriya, Malaviarachchi, Kriegsman, Sajeev, et al. (2017) argued that these garnets (in which the core area has grown via reaction 1 and the mantle to rim areas via reaction 2 could have grown across silica saturated and silica-deficient microdomains of the rock during its prograde evolution.

Isolated inclusions of quartz, biotite and sillimanite in the area between the mantle and rim of garnets in $Domain_2$ and $Domain_3$ could also have resulted via reaction 2 during the prograde evolution of the rock. All domains contain ample evidence for the existence of melt phases such as the presence of leucosome consisting of two feldspars, quartz and acicular biotite.

The intergrowth of coarse-grained Al-rich orthopyroxene with medium- to coarse-grained prismatic sillimanite as a corona around garnet, in the presence of quartz, in $Domain_1$ (Figure 3b,d,e) indicates the continuous reaction:

$$Grt + Qz = Opx + Sil \qquad (3)$$

Kriegsman and Schumacher (1999) also reported this reaction and attributed it to decompression after peak P–T conditions. Kriegsman (1996) calculated the slope dP/dT of this
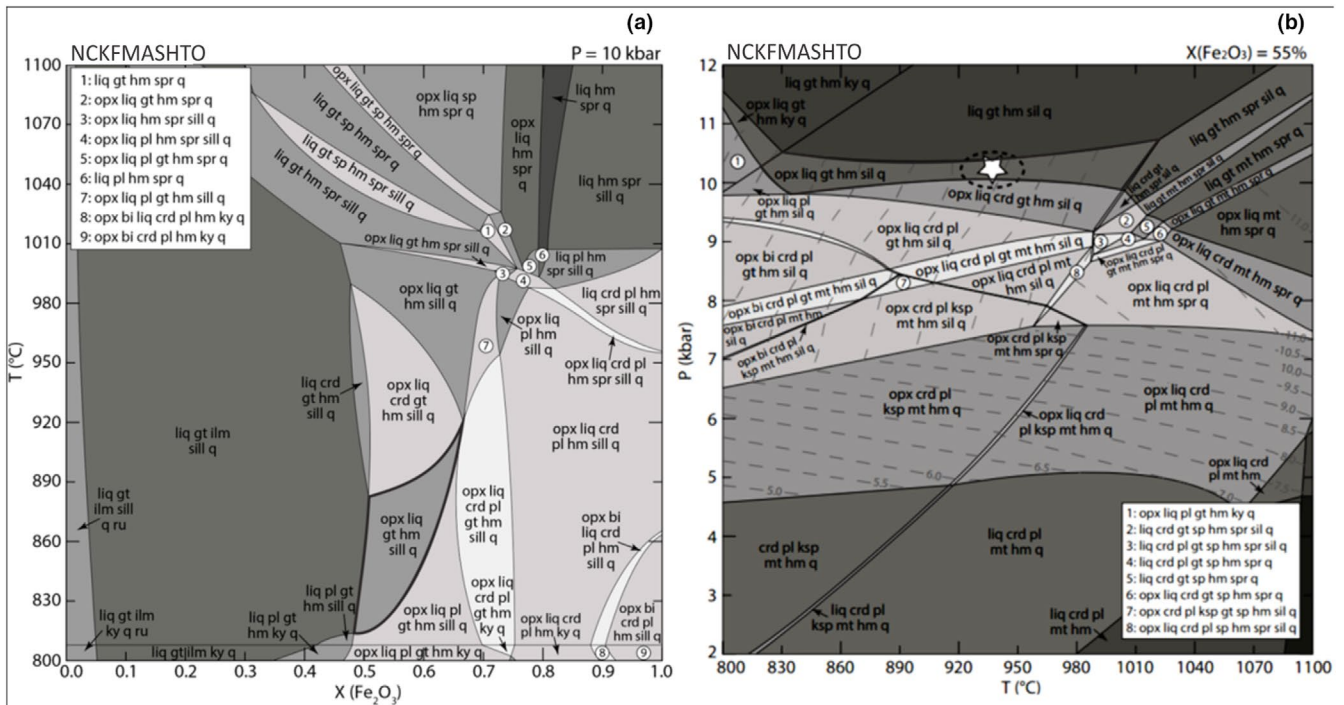
FIGURE 6 Pseudosection calculated based on recalculated local bulk composition data for $Domain_1$. (a) T–$X(Fe2O3)$ pseudosection calculated in the NCKFMASHTO system at P = 10.0 kbar for the $domain_1$ composition; (b) P–T pseudosection calculated at $X(Fe_2O_3)$ = 0.55 for the $domain_1$ composition. Solution-phase models used in the calculations are given in the text of Section 7.2.1. The composition (wt%) is SiO_2: 38.75, TiO_2: 3.01, Al_2O_3: 24.47, FeO: 6.4, Fe_2O_3: 17.4, MgO: 8.87, CaO: 0.27, Na_2O: 0.33, K_2O: 0.02, H_2O: 0.49 [Colour figure can be viewed at wileyonlinelibrary.com]

TABLE 6 Conventional thermobarometric data calculated for Domains 1, 2 and 3

Mineral Composition	Si	Ti	Al	Mg	Fe^{2+}	Fe^{3+}	Mn	Ca	Na	K	Nominal T (°C)	Nominal P (kbar)	Calculated P (kbar)	Calculated T (°C)	Reference[a]
Pre-peak conditions															
Domain 1															
Biotite inclusion		0.54		3.83	1.08		0.09	0.12			800			820	{1}
Garnet (core)				1.37	1.38	0.07		0.25	0.78	0.01	850		$10.3^{(Sil)}/10.4^{(Ky)}$		{2}
Plagioclase**													$11.1^{(Sil)}/11.3^{(Ky)}$		{2}
Biotite inclusion(O =11)***	2.95	0.29		2.09	0.59		0.01	0.00	0.01	0.97	875		$11.6^{(Sil)}/11.7^{(Ky)}$		{2}
Domain 2															
Biotite inclusion		0.48		4.09	0.77		0.04	0.10			800			829	{1}
Garnet (core)				1.68	1.23	0.11		0.24	0.76	0.01	850		$9.6^{(Sil)}$		{2}
Plagioclase**													$10.6^{(Sil)}$		{2}
Biotite inclusion(O =11)*	2.99	0.26		2.21	0.42		0.00	0.01	0.06	0.91	875		$10.8^{(Sil)}$		{2}
Domain 3															
Biotite inclusion		0.47		3.65	1.24		0.05	0.11			800			795	{1}
Garnet (core)				1.60	1.24	0.07		0.19	0.82	0.01	850		$11.6^{(Sil)}/11.4^{(Ky)}$		{2}
Plagioclase**													$12.5^{(Sil)}/12.3^{(Ky)}$		{2}
Biotite inclusion(O =11)*	2.96	0.24		2.16	0.45		0.00	0.00	0.06	0.97	875		$12.9^{(Sil)}/12.8^{(Ky)}$		{2}
Peak conditions															
Domain 1-Rock H								0.08				8		902	{3}
Garnet (mantle)				1.45	1.33	0.03	0.12					9		932	{3}
Orthopyroxene#			0.00	0.38	1.29	0.46						10		963	{3}
Domain 2-Rock H								0.06				8		917	{3}
Garnet (mantle)				1.52	1.36	0.00	0.05					9		947	{3}
Orthopyroxene##			0.35	1.30	0.50	0.03						10		978	{3}
											900		8.1		{4}#
											950		8.36		{4}#
											1,000		8.6		{4}#

TABLE 6 (Continued)

Mineral Composition	Si	Ti	Al	Mg	Fe²⁺	Fe³⁺	Mn	Ca	Na	K	Nominal T (°C)	Nominal P (kbar)	Calculated P (kbar)	Calculated T (°C)	Reference[a]
Plagioclase *#*															
								0.21	0.79	0.00	900		$9.3/8.4^{(Sil)}$		{5}/{2}
											950		$9.7/9.1^{(Sil)}$		{5}/{2}
											10,000		$10.1/9.7^{(Sil)}$		{5}/{2}
Domain 3															
Garnet (mantle)				1.60	1.29	0.02	0.04	0.07				8		920	{3}
Orthopyroxene###			0.36	1.28	0.50	0.05						9		950	{3}
												10		981	{3}
											900		10.6		{4}#
											950		11.0		{4}#
											1,000		11.3		{4}#
Plagioclase *#*															
								0.20	0.78	0.02	900		$10.5/9.8^{(Sil)}$		{5}/{2}
											950		$11.1/10.7^{(Sil)}$		{5}/{2}
											1000		$11.6/11.5^{(Sil)}$		{5}/{2}

**Plagioclase: plagioclase inclusions in the core of Garnet; *#*Plagioclase: plagioclase in the matrix; ***Biotite inclusion$^{(O=11)}$: for 11 oxygen p.f.u.; Orthopyroxene#: Coarse orthopyroxene in Opx–Sil corona; Orthopyroxen##: Biotite $^{(Mt)}$: Matrix biotite.

[a] {1} Ti in Biotite geothrmometer (Henry et al., 2005); {2} $^{(Sil)}$ Grt–Sil–Pl–Qz geobarometer (Koziol & Newton, 1988); {3} Grt–Opx geothermometer (Harley & Green, 1982); {4} #Grt–Opx geobarometer (Newton & Perkins, 1982). Octahedral Al has been estimated as $Al^{M1} = 2-Si-Fe^{3+}$. {5} $^{(Ky)}$ Grt–Ky–Pl–Qz geobarometer, $^{(Sil)}$ Grt–Sil–Pl–Qz geobarometer (Ganguly & Saxena, 1984); (Av): Average.

reaction to be −6.5 bar/K in the FMAS system with Grt+Qz on the *HP-HT* side. The inferred *P–T* path in his Figure 3 allows this reaction to be up-temperature if it occurs after the peak pressure, that is, heating during decompression. In the NCKFMASHTO system (e.g. Figure 6b), the slope is ~0 bar/K, which makes it easier to cross the reaction field during such a *P–T* path.

The intergrowth of coarse-grained Al-rich orthopyroxene with medium- to coarse-grained prismatic sillimanite in the matrix in Domain$_2$ (Figure 4g,h) and intergrowth of Al-rich medium-grained orthopyroxene and needle-shaped sillimanite at the rim of garnets in Domain$_3$ (Figure 5d) could also be produced by reaction 3. This reaction is well known from other UHT granulites (e.g. Limpopo Belt: Belyanin et al., 2012).

6.2 | Peak metamorphic assemblages

The peak assemblage of the Domain$_1$ and Domain$_2$ was recognized as garnet, Al-rich orthopyroxene, sillimanite, quartz, plagioclase, K-feldspar, Fe-Ti oxides and melt. Orthopyroxene+sillimanite+quartz is the typical UHT mineral assemblage found in both domains. The occurrences of sapphirine surrounded by plagioclase in leucosomes in Domain$_1$ (Figure 3p) could indicate the existence of localized domains of sapphirine+melt, where the melt crystallized during cooling. In Domain$_3$ garnet, Al-rich orthopyroxene, plagioclase, K-feldspar, quartz and Fe-Ti oxides and melt may be regarded as the peak metamorphic assemblage.

6.3 | Retrograde mineral textures

In Domain$_1$ and Domain$_3$, the presence of ternary feldspars indicates that the rocks have undergone a period of slow cooling after peak metamorphism. The local crystallization of leucocratic nabs and pods which mainly contain relatively coarse plagioclase, K-feldspars and irregular quartz in three domains may have resulted from the same cooling stage. Local crystallization of quartz with fibrolitic sillimanite inclusions could have crystallized from a melt phase. In addition, the studied samples contain ample retrograde reaction textures as indicated below.

In Domain$_1$, the occurrence of cordierite around orthopyroxene–sillimanite coronae in the presence of quartz (Figure 3f–k) may indicate the retrograde reaction:

$$Opx + Sil + Qz = Crd \qquad (4)$$
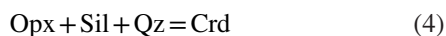
Orthopyroxene–cordierite symplectites around garnet (Figure 3a,f,g,h) provide clear evidence for the retrograde reaction:

$$Grt + Qz = Opx + \ Crd. \qquad (5)$$

The local occurrences of tiny spinel within orthopyroxene–sillimanite–cordierite-bearing domains (Figure 3l) can be explained by the reaction:

$$Opx + Sil = Spl + Crd, \qquad (6)$$
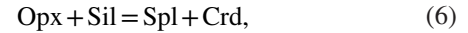
under local silica-deficient conditions, whereas the local formation of sapphirine with spinel inclusions in between magnetite, cordierite and vermicular orthopyroxene (Figure 3m) could imply the oxidizing reaction:

$$Crd + Spl = Spr + Mag. \qquad (7)$$

Biotite–plagioclase coronae around garnet in Domain$_2$ (Figure 4e) and Domain$_3$ could result from the reaction:

$$Grt \pm \ Kfs + Melt = \ Bt + Pl, \qquad (8)$$
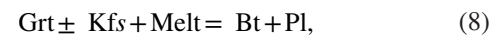
which is a melt-consuming reaction in the sense of Kriegsman and Álvarez-Valero (2010). The partial replacement of orthopyroxene by biotite and quartz in Domain$_1$, Domain$_2$ and Domain$_3$ can be explained by another melt-consuming reaction:

$$Opx \pm \ Kfs + Melt = \ Bt + Qz. \qquad (9)$$

The abundance of leucosome in the quarry suggests that the source of the required H$_2$O-bearing fluid phase to balance the reaction 8 and 9 is indeed likely to be a crystallizing melt phase after peak metamorphism.

7 | *P–T* CALCULATIONS

The metamorphic evolution was reconstructed combining the results of pseudosections, conventional geothermobarometry and trace element thermometry for the different rock types.

7.1 | Prograde evolution

Due to the dynamic changes of rock composition via melt loss, the overprinting of early assemblages by peak- and post-peak phases and the homogenization of mineral chemistry during the high-grade metamorphism, the reconstruction of the prograde segment of the *P–T* path is a challenging task (Harley, 2008; Kelsey, 2008). Nevertheless, mineral assemblages preserved as trapped inclusions in large porphyroblasts such as garnet may provide crucial information on at least a portion of the prograde history (e.g. Dharmapriya, Malaviarachchi, Kriegsman, Galli et al., 2017; Hiroi et al., 1994). For this purpose, inclusion phases present in the core to mantle

areas of porphyroblastic garnets were investigated similar to Dharmapriya, Malaviarachchi, Santosh, et al. (2015) in which the authors estimated the prograde condition of Domain$_1$. In view of the fact that, on the one hand, granulites may not be able to preserve whole-rock and/or mineral compositions of the whole metamorphic cycle, and on the other hand, each approach for constraining metamorphic P and T has its own deficiencies, we thus attempt to integrate a large set of approaches here.

To estimate the prograde P–T evolution of Domain$_1$, Domain$_2$ and Domain$_3$, we used inclusion phases present in the core and mantle areas of porphyroblastic garnets (Table 6). The core compositions of garnet and its inclusions (e.g. core compositions of Pl, Bt) were used for calculations. Considering the garnet chemistry, we could identify a slight compositional zonation of grossular content from core to rim in some domains (e.g. Domain$_1$). In addition, the chemical composition of mineral inclusions in garnet and the matrix are also slightly different. For example, in Domain$_1$ the grossular content of porphyroblastic garnet decreased slightly but consistently from 0.040 at the core, through 0.032 at the mantle to 0.029 at the rim (Table 1). As Ca diffusion is slower than Fe and Mg diffusion (e.g. Vielzeuf et al., 2007), the Ca content in garnet may preserve its original zoning pattern even when Fe, Mg and Mn are homogenized. Also, the anorthite content of plagioclase inclusions in garnet and the composition of plagioclase in the matrix are 0.24 and 0.36, respectively (Table 4). The X_{Mg} and the TiO_2 content of biotite inclusions in garnet are 0.78 and 5.00 wt%, respectively, whereas those in matrix biotite are 0.68 and 6.20 wt%, respectively (Table 2).

Due to the slow diffusion of Ti in the biotite structure (e.g. Henry et al., 2005), the Ti in biotite inclusions is likely to represent the prograde composition. In addition, there is no exchange mechanism with the garnet host to modify Ti. The same applies to Na in plagioclase, which can therefore also preserve prograde conditions. However, the X_{Mg} of biotite inclusions in garnet is prone to retrograde re-equilibration (e.g. Fernando et al., 2003 and many others).

The peak temperature was estimated independently using the Ti in biotite geothermometer of Henry et al. (2005) and the pressure was calculated using the garnet–aluminosilicate–plagioclase–quartz (GASP) geobarometer of Koziol and Newton (1988). GASP yielded a P of ~11 to 11.5 kbar at an estimated temperature of 850°C. However, the uncertainty associated with the calculated prograde P, T conditions is relatively high due to retrograde Fe–Mg between garnet and biotite. Using melting experiments of natural metapelites under fluid-absent conditions, Vielzeuf and Holloway (1988) found that reaction 2 can take place at a minimum temperature of ~860°C. Since the Ti content of the biotite inclusions in garnets of the three domains are 4.5–5 wt%, the breakdown of biotite is likely to have taken

place at high-T conditions. Hence, the calculated prograde temperature conditions (~800–830°C) from Ti in biotite thermometer are deemed more reliable than the experimental constraints. The possible uncertainties associated with the above P–T calculations are presented in Section 8.1.1.

7.2 | Peak metamorphic conditions

7.2.1 | Phase equilibria modelling

Pseudosections were constructed in the chemical system NCKFMASHTO with the software Perplex_X_07 (Connolly, 2005), using a modified version of the internally consistent thermodynamic dataset 'kel04ver.dat' (the 2004 update of the Holland & Powell, 1998 database). The mineral solution models used are follows: alkali-feldspar—San: Waldbaum and Thompson (1969), biotite—Bio(TCC): Tajčmanová et al. (2009), cordierite—hCrd: Holland and Powell (1998), garnet—Gt(WPH): White et al. (2007), ilmenite—Ilm(WHP); White et al. (2000), melt—melt (HP): White et al. (2007), orthopyroxene—Opx(HP): Powell and Holland (1999), plagioclase—Pl(h): Newton et al. (1980), sapphirine—Sapp(Tp): Taylor-Jones and Powell (2010), spinel—Sp(WPC): White et al. (2002) and white mica—wm (HP): Holland and Powell (1998).

The homogeneous samples from Domain$_2$ and Domain$_3$ were modelled using their bulk compositions as measured by XRF analysis. For the heterogeneous sample from Domain$_1$, which shows an irregular distribution of residuum and melts, we retrieved the bulk composition of the residual part and combined it with the measured mineral compositions and modes. The calculated compositions are given in the figure caption (Figure 6). H_2O contents correspond to the loss on ignition. Input XRF bulk compositions used for pseudosection calculations of Domains 2 and 3 are given in Table 5. For each sample, the bulk Fe_2O_3 content was estimated from T–$X(Fe_2O_3)$ sections as calculated at $P = 10$ kbar. P–T pseudosections were contoured for Al_2O_3 in orthopyroxene and for mineral modes using the software PyWerami. The mean Al_2O_3 content of orthopyroxene was taken, considering core and rim compositions of orthopyroxene in Domains 1, 2 and 3.

Peak P–T *estimation by phase equilibria modelling for bulk compositions from measured mineral compositions and modes*

Domain$_1$: The T–$X(Fe_2O_3)$ diagram (Figure 6a) displays the effects of the oxidation state on the assemblage stability fields. The observed peak assemblage orthopyroxene–garnet–sillimanite–quartz–hematite–melt is predicted to be stable for $X(Fe_2O_3)$ ranging between 0.45 and 0.65 and T comprised
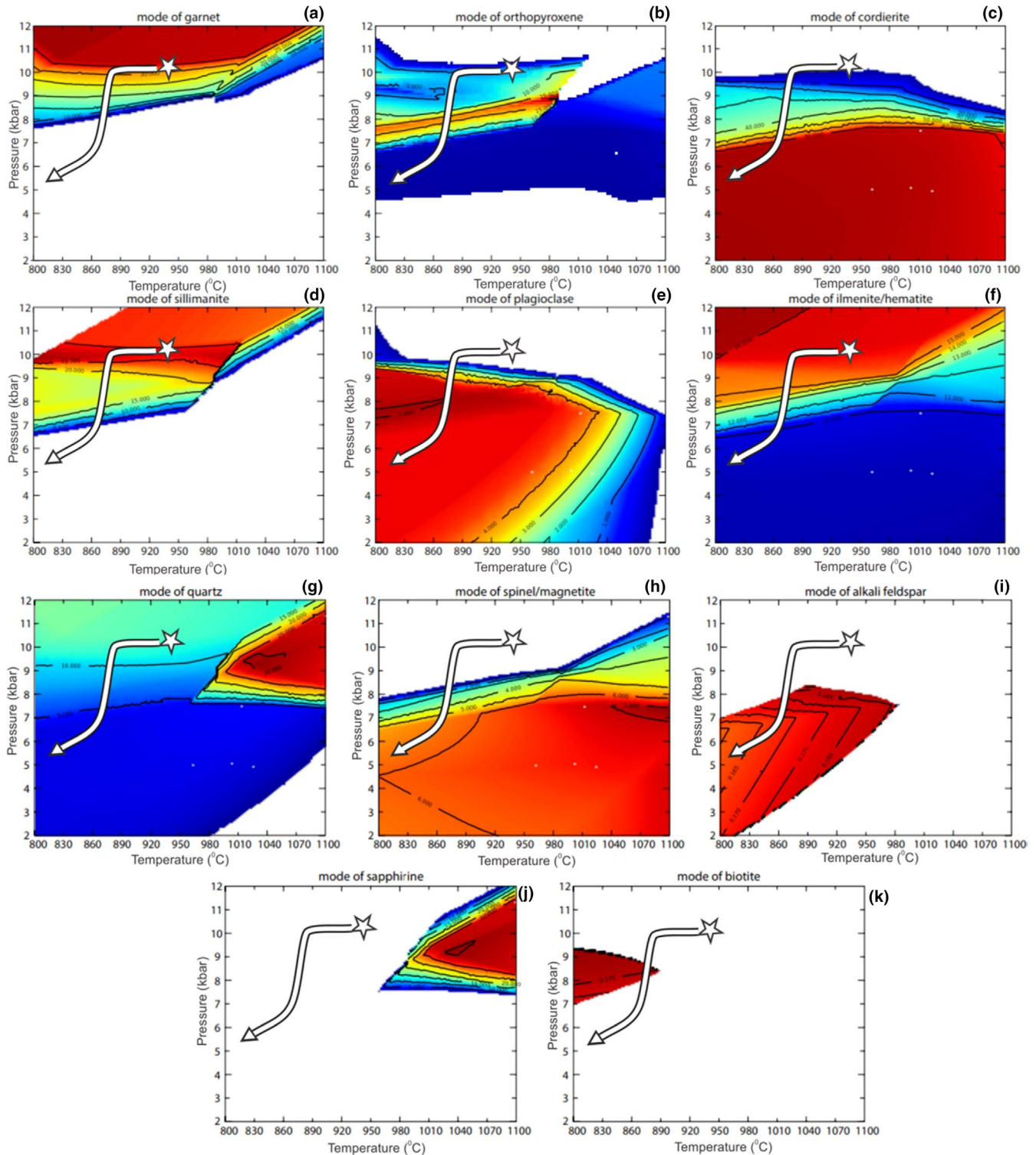
FIGURE 7 *P–T* diagrams showing the modal proportion (vol.%) of selected minerals in Domain$_1$: garnet (a), orthopyroxene (b), cordierite (c), sillimanite (d), plagioclase (e), ilmenite/hematite (f), quartz (g), spinel/magnetite (h), K-feldspar (i), sapphirine (j) and biotite (k); calculated in the NCKFMASHTO system for Domain$_1$-Rock A. Star corresponds to the estimated *P–T* peak conditions calculated from *P–T* pseudosections and conventional geothermobarometry; arrows display the inferred post-peak *P–T* path [Colour figure can be viewed at wileyonlinelibrary.com]

between 925 and 1,010°C. At higher *T* and/or high $X(Fe_2O_3)$, sapphirine would appear. At lower *T*, cordierite is predicted to occur. Also, it is noted that for $X(Fe_2O_3) < 0.45$, orthopyroxene would not be stable (See Figure 6a).

In the *P–T* pseudosection calculated at $X(Fe_2O_3) = 0.55$ (Figure 6b), the peak assemblage is stable over a wide *T* window ranging between 820 and 1,015°C but for a narrow *P* range from 9.5 to 10.5 kbar. At lower *T* and *P*, plagioclase and cordierite are

predicted to be stable, respectively, whereas at higher T and P sapphirine would appear and orthopyroxene would disappear, respectively. Contouring the pseudosection for Al_2O_3 in orthopyroxene (mean = 8.9 wt% Al_2O_3) narrows the T estimate to ~920–950°C and P of 10 kbar. Figure 7 shows the $P–T$ diagram from Figure 6b, with modal abundance contours for various phases. A detailed discussion is found in the Section 7.3.

7.2.1.2. Peak P–T estimation by phase equilibria modelling after whole-rock bulk compositions as measured by XRF analysis

Domain$_2$: The $T–X(Fe_2O_3)$ sections of Figure 8a show that the peak assemblage orthopyroxene–garnet–sillimanite–quartz–plagioclase–K-feldspar–hematite–melt is stable only for $X(Fe_2O_3)$ ~0.70. At lower $X(Fe_2O_3)$, no sillimanite is predicted to be stable, whereas at higher oxidizing conditions, garnet would disappear. The occurrence of alkali feldspar and the lack of biotite limit the temperatures between 915 and 950°C.

In the $P–T$ section calculated at $X(Fe_2O_3) = 0.70$ (Figure 8b), the field corresponding to the observed peak assemblage occurs at T between 910 and 955°C and P ~9.5–10 kbar. This estimate is in good agreement with $P–T$ inferred from Domain$_1$ and with the position of the Al in Opx isopleth corresponding to the mean measured value of 8.3 wt% Al_2O_3.

Domain$_3$: As outlined by the $T–X(Fe_2O_3)$ section of Figure 9a, the peak assemblage orthopyroxene–garnet–sillimanite–quartz–plagioclase–K-feldspar–hematite–melt requires high oxidizing conditions ranging between 0.58 and 0.76 to be stable. The simultaneous appearance of garnet and orthopyroxene constrains the possible range of $X(Fe_2O_3)$, whereas the lack of biotite and magnetite constrains the T window.

In the $P–T$ diagram of Figure 9b calculated at $X(Fe_2O_3) = 0.70$, the occurrence of peak orthopyroxene limits the maximum pressure to ~11 kbar, whereas the lack of magnetite suggests a minimum pressure ~9.5 kbar. The observed peak assemblage is predicted to be stable for a wide temperature range comprised between 900 and 1,020°C. Again, the Al in orthopyroxene isopleths (mean value: 8.5 wt% Al_2O_3) allow confining the estimated temperature at ~920–940°C and pressure of ~10 kbar. Figure 10 is a $P–T$ diagram showing the modal proportion variation for Domain$_3$ and a detailed discussion is found in the Section 7.3.

Peak P–T estimation by conventional geothermobarometry

Geothermobarometric calculations were undertaken using both the Harley and Green (1982) and Aranovich and Berman (1997) calibrations of the Grt-Opx geothermometer for Domain$_1$ to Domain$_3$, the Newton and Perkins (1982) calibration of the orthopyroxene–garnet–plagioclase–quartz geobarometer for Domain$_2$ and Domain$_3$, and the Koziol and
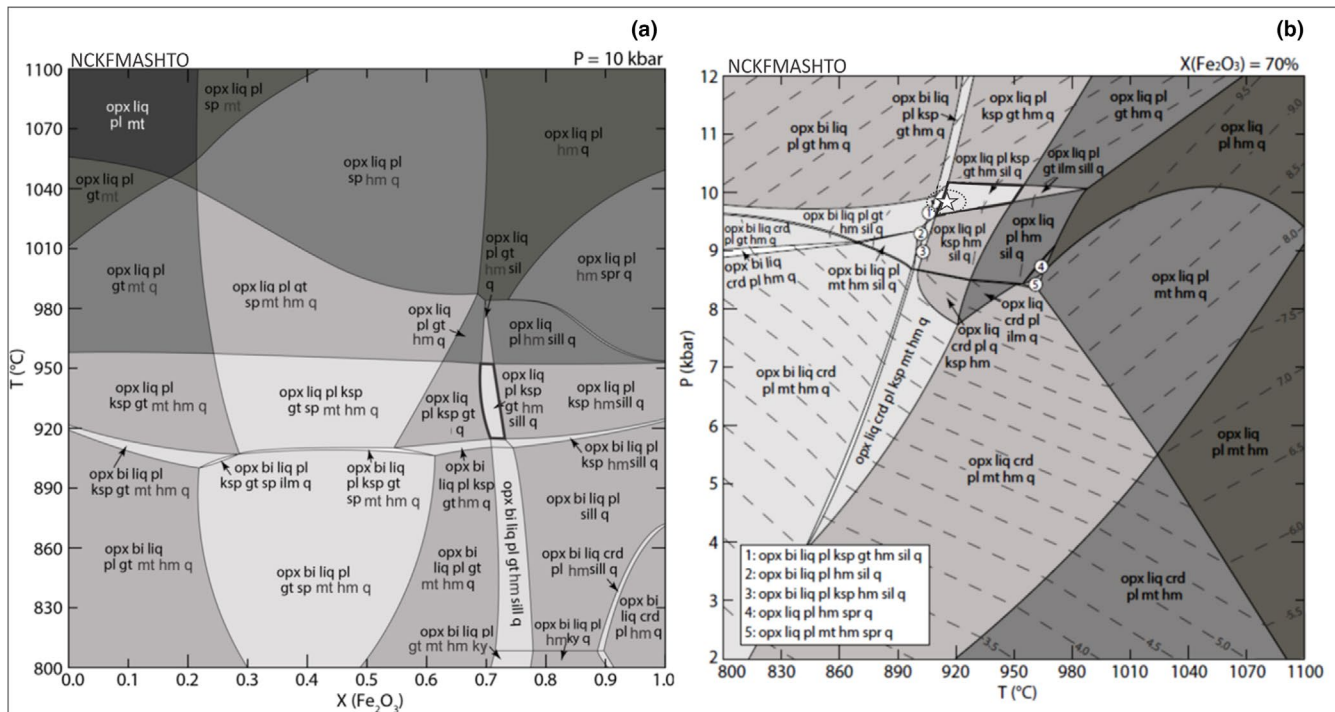
FIGURE 8 Pseudosection calculated based on XRF data for Domain$_2$. (a) $T–X(Fe_2O_3)$ pseudosection calculated in the NCKFMASHTO system at $P = 10.0$ kbar for the domain$_2$ composition; (b) $P–T$ pseudosection calculated at $X(Fe_2O_3)=0.70$ for the domain$_2$ composition. The XRF data used for calculation are given in Table 5. Solution-phase models used in the calculations are given in Table 5 [Colour figure can be viewed at wileyonlinelibrary.com]
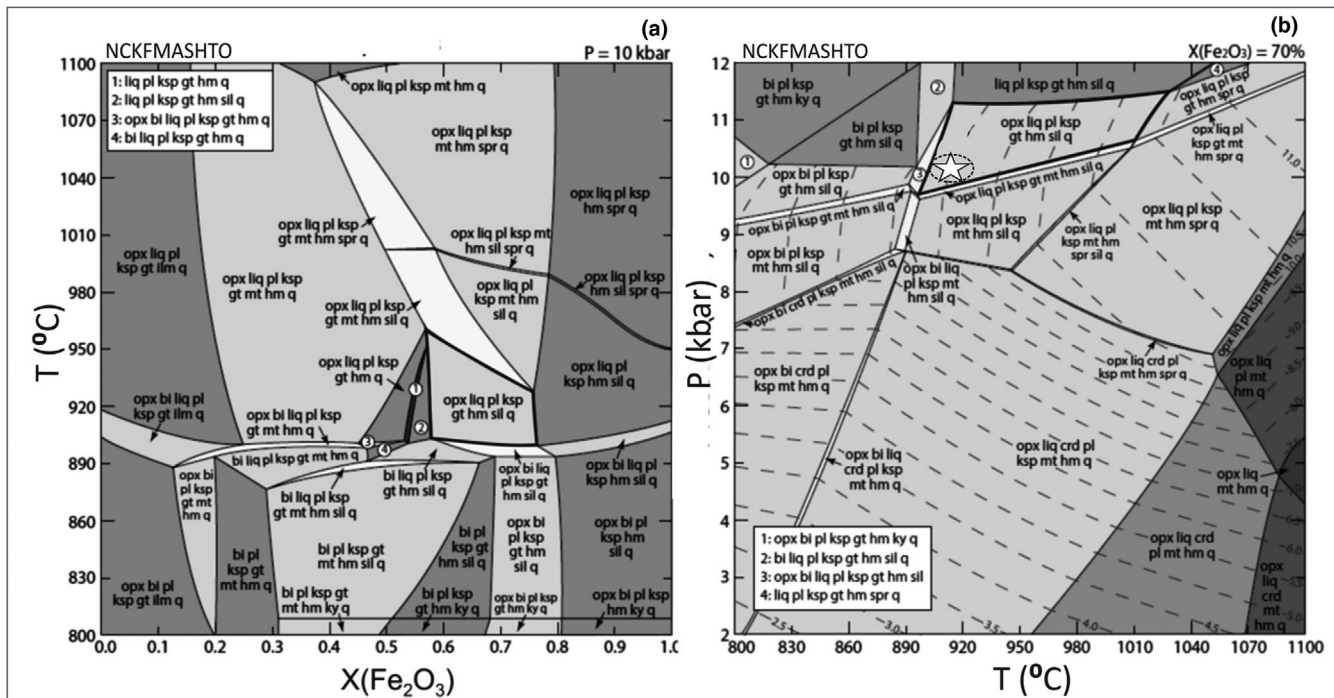
FIGURE 9 Pseudosection calculated based on XRF data for Domain$_3$. (a) T–$X(Fe_2O_3)$ pseudosection calculated in the NCKFMASHTO system at $P = 10.0$ kbar for the domain$_3$ composition; (b) P–T pseudosection calculated at $X(Fe_2O_3) = 0.70$ for the domain$_3$ composition. The XRF data used for calculation are given in Table 5. Solution-phase models used in the calculations are given in Table 5

Newton (1988) and Ganguly and Saxena (1984) calibrations of the GASP geobarometer for Domain$_2$ and Domain$_3$. For the calculations, we used the averaged core compositions of porphyroblastic orthopyroxene and matrix plagioclase and the averaged mantle composition of garnet porphyroblasts.

Temperatures estimated by the Grt-Opx geothermometer of Harley and Green (1982) and Aranovich and Berman (1997) are strongly sensitive to the amount of octahedral Al estimated in the orthopyroxene structure (e.g. Pattison et al., 2003) and may be considerably reduced if the effect of Fe^{3+} is considered (e.g. Harley, 2008). In the calculations, $Al^{M1} = Al^{tot}/2$ was estimated and the results were compared assuming $Al^{M1} = 2–Si–Fe^{3+}$. The amount of ferric iron is determined stoichiometrically from microprobe analyses (Droop, 1987). Chemical parameters and the results of the calculations are summarized in Table 6.

Domain$_1$: Peak T calculated with the Harley and Green (1982) calibrations of the Grt-Opx geothermometer assuming $Al^{M1} = Al^{tot}/2$ are 955, 987 and 1,020°C, at nominal P of 8, 9 and 10 kbar. However, when the effects of Fe^{3+} are considered, the same calibrations yield considerably lower T of 902, 932 and 963°C (Table 6). Whereas the former calculation exceeds the temperatures of 920–950°C estimated from the P–T pseudosection contoured for Al in orthopyroxene by ~50°C, the latter fits the results of the phase diagram well. The stoichiometric calculations indicate that the Fe^{3+}/Fe^{2+} ratio in Opx approaches 20% in these highly oxidized rock

compositions, thus favouring an estimate of the octahedral Al as $2–Si–Fe^{3+}$.

Domain$_2$: Similar to Domain$_1$, T calculated using the Grt-Opx thermometers assuming $Al^{M1} = Al^{tot}/2$ exceed those calculated considering Fe^{3+} by 20°C for the Harley and Green (1982) calibrations, respectively (Table 6). In the second case, calculated T of 917, 947, 978°C at P of 8, 9 and 10 kbar are in the range of the P–T conditions estimated from the P–T pseudosection. Pressures calculated using the GASP barometer yield 9.3, 9.7, 10.1 kbar and 8.4, 9.1, 9.7 kbar for the Ganguly and Saxena (1984) and Koziol and Newton (1988) calibrations, respectively, at nominal T of 900, 950 and 1,000°C. At the same T, the Newton and Perkins (1982) calibration of the Grt–Opx–Pl–Qz barometer yields slightly lower P of 8.1, 8.4, 8.6 kbar, respectively (Table 6).

Domain$_3$: Again, T of 920, 950, 981°C calculated with the Harley and Green (1982) thermometer, assuming $Al^{M1} = 2–Si–Fe^{3+}$ fit the P–T of 920–940°C and 10 kbar inferred from the P–T pseudosection better than assuming $Al^{M1} = Al^{tot}/2$ (Table 6). Pressures estimated using the GASP barometer are 10.5, 11.1, 11.6 kbar and 9.8, 10.7, 11.5 kbar at nominal T of 900, 950, 1,000°C using the Ganguly and Saxena (1984) and Koziol and Newton (1988) calibrations, respectively. Similar P of 10.6, 11, 11.3 kbar at T of 900, 950, 1,000°C (Table 6) are estimated using the Grt-Opx-Pl-Qz barometer of Newton and Perkins (1982).
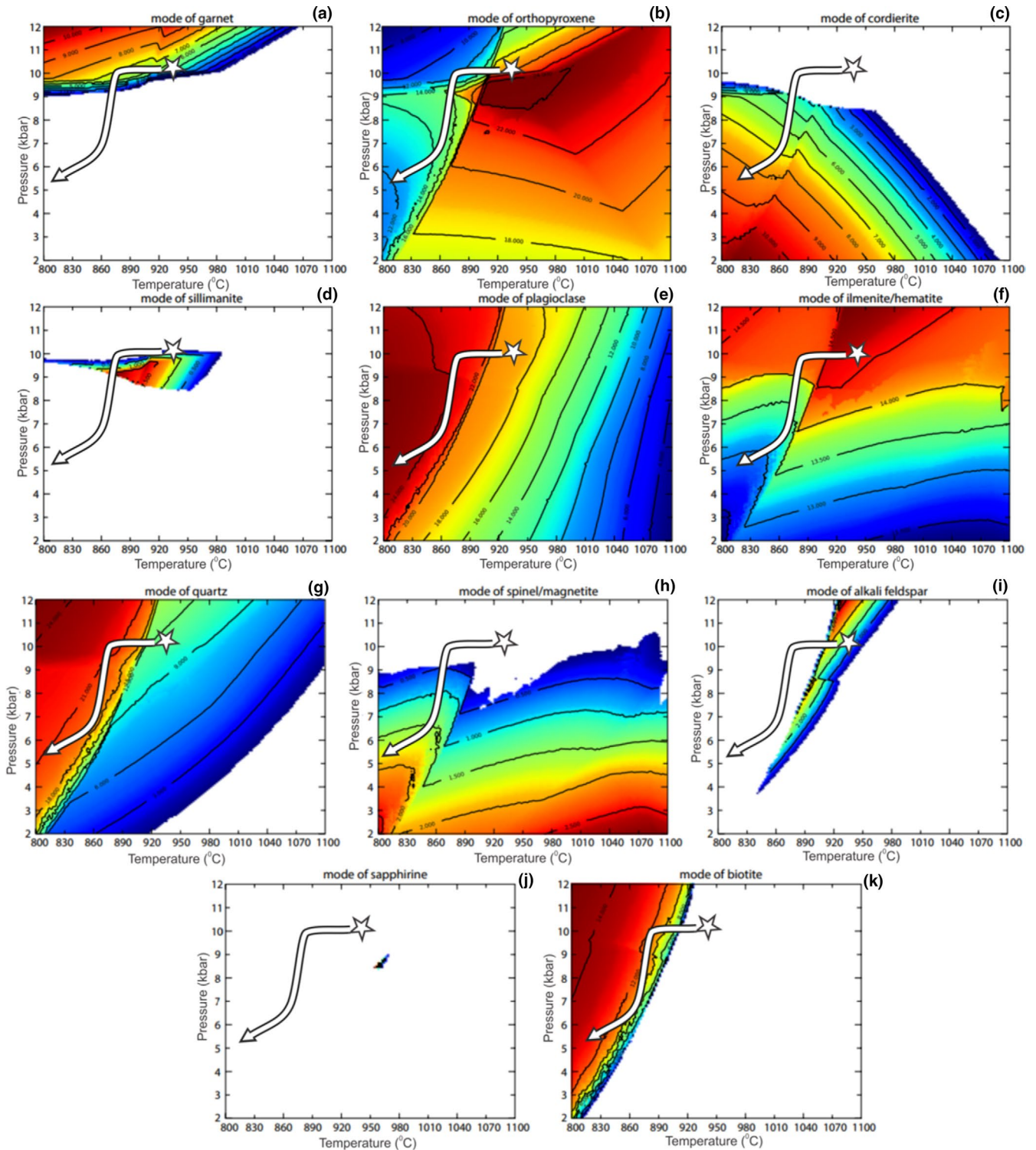
FIGURE 10 *P–T* diagrams showing the modal proportion (vol.%) of selected minerals in Domain$_3$:(a) garnet, (b) orthopyroxene, (c) cordierite, (d) sillimanite, (e) plagioclase, (f) ilmenite/hematite, (g) quartz, (h) spinel/magnetite, (i) K-feldspar, (j) sapphirine and (k) biotite expressed; calculated in the NCKFMASHTO system for Domain$_1$. Star corresponds to the estimated *P–T* peak conditions calculated from *P–T* pseudosections and conventional geothermobarometry; arrows display the inferred post-peak *P–T* path [Colour figure can be viewed at wileyonlinelibrary.com]

Peak P–T *estimation by trace element thermometry*

Peak metamorphic conditions were calculated for Domain$_3$ and Domain$_4$ (i.e. the host rock of the quarry) using Ti-in-zircon thermometry after Watson Wark and Thomas

(2006) and Ferry and Watson (2007). The calculations were done using the Ti content of 8 and 18 ppm in metamorphic zircon of Domain$_3$ and Domain$_4$, respectively. The analytical conditions for trace element analysis of

those zircons are given in Appendix S1, where Table S1 presents the results.

The measured Ti concentrations correspond to apparent temperatures of Domain$_3$ and Domain$_4$ after the Ti-in-zircon thermometry of Watson et al. (2006), in the range of 690–732°C (mean 711°C) and 680–861°C (mean 714°C), respectively. However, a number of studies pointed out that the activity of both TiO_2 and SiO_2 must be known very accurately to apply the Ti-in-zircon thermometer when the rock is undersaturated with SiO_2 and/or TiO_2. Though the studied samples are SiO_2 saturated, they lack free rutile grains and the available Fe-Ti oxides are mainly present in exsolved titanohematite–ilmenite±rutile. The presence of Ti-rich minerals such as ilmenite may suggest a relatively high TiO_2 activity at the time of zircon crystallization, assuming that the Ti-phase and zircon crystallized together (Fu et al., 2008). By contrast, even ilmenite-bearing rocks have been found to have $a TiO_2$ as low as 0.6 (Watson et al., 2006). Watson and Harrison (2005) suggested that most natural melts capable of crystallizing zircons (i.e. saturated in $ZrSiO_4$) have TiO_2 activities exceeding ~0.5. Hence, we calculated T after the thermometer of Ferry and Watson (2007) with $a TiO_2$ at 0.6, 0.7 and 0.8, respectively (using $a SiO_2 = 1$). This gave temperatures in the range 736–786°C (mean 761°C), 723–770°C (mean 746°C) and 711–758°C (mean 734°C), respectively, for Domain$_3$ and in the range of 723–940°C (mean 766°C), 710–920°C (mean 751°C) and 698–903°C (mean 738°C), respectively, for Domain$_4$ (Table S1). However, the mean temperatures obtained from both domains for various $a TiO_2$ are much lower than the obtained peak T for the studied samples from both pseudosections and conventional thermometric methods. It is noted that for retrieving the same peak metamorphic conditions obtained from the conventional thermobarometry and hybrid phase equilibrium modelling for domains 1,2 and 3 the $a TiO_2$ should be less than 0.2 in both domains 2 and 4. The obtained lower temperatures could be due to a much lower $a TiO_2$ of the rocks than we inferred or, alternatively, the zircons may not have fully equilibrated with respect to Ti during their crystallization, or alternatively zircon growth may not have commenced until the peak of metamorphism (e.g. Baldwin & Brown, 2008; Kelsey, 2008; Kelsey & Hand, 2015; Kelsey & Powell, 2011).

7.3 | Post-peak evolution

Textural observations revealed the occurrence of many post-peak reactions, especially developed in different domains of the studied rocks, which lead to the formation of coronae and symplectitic aggregates around peak-metamorphic porphyroblasts (see reactions 4, 5, 9). Such post-peak features associated with mineral zoning may allow reconstructing the detailed post-peak $P–T$ path. This possibility was investigated using isopleths representing the mode (abundance) of each single mineral phase in $P–T$ space (Figures 7 and 10). Such an approach is potentially very useful because it allows visualizing in which direction minerals are predicted to increase or decrease their modes (but not necessarily appear or disappear), thus displaying the position and slope of mineral reactions in a $P–T$ diagram.

In Domain$_1$, porphyroblastic orthopyroxene shows a rim-ward decrease in Al_2O_3 content from ~9.0 to ~8.2 wt%. As suggested by the nearly vertical slope of the Al in Opx isopleths at $P > 7$ kbar in the $P–T$ section (Figure 7), such zoning indicates that the rock experienced a period of isobaric cooling from peak T at ~940°C down to $T < 900°C$ at ~10 kbar, compatible with the change of ~30–45°C per wt% of Al_2O_3 reported from many granulitic terrains (e.g. Harley & Motoyoshi, 2000; Podlesskii, 2006). The formation of cordierite±plagioclase at the expense of sillimanite, quartz and orthopyroxene, inferred by textural observations (reaction 4), is reproduced by the modelling of mineral isopleths to occur during the early stage of decompression at P ~9–9.5 kbar. Furthermore, nearly isothermal decompression is predicted to produce orthopyroxene and cordierite after garnet at P ~7–8 kbar, which corresponds to reaction 5. During the late observable stage of decompression, spinel/magnetite and cordierite are predicted to increase their modal abundance, whereas sillimanite and orthopyroxene would be consumed at $T < 7$ kbar, as inferred from reaction 6.

Modal abundance isopleths of orthopyroxene, quartz, plagioclase, biotite and melt (but not garnet) calculated for Domain$_3$ show a completely different topology, compared to that of Domain$_1$ (Figure 10). As illustrated in Figure 10, the modal abundance of these phases is strongly T-dependent and not as P-dependent as those in Domain$_1$. Thus, the occurrence of quartz, biotite±plagioclase around porphyroblastic orthopyroxene suggests that such coronae formed during an isobaric cooling stage after peak T, probably in the presence of melt (reaction 8) at ~900°C, in accordance with an early phase of isobaric cooling inferred from Al zoning in orthopyroxene in Domain$_1$. Cordierite-bearing textures, which would suggest a subsequent phase of isothermal decompression, are not developed in the studied samples.

8 | DISCUSSION

8.1 | $P–T$ evolution of the studied sapphirine granulites and implications for the metamorphic evolution of UHT granulites in the HC

8.1.1 | Prograde metamorphism

The prograde conditions calculated by conventional thermobarometric calculations yielded P ~ 11 to 11.5 kbar at T

~800–850°C. The peak metamorphic conditions calculated from both conventional thermobarometry and pseudosections indicate that the pressure condition at the peak of metamorphism was ~9.5 to 10.5 kbar ~920–940°C. Hence, the pressure condition at peak metamorphic conditions is 1–2 kbar lower than the maximum pressure (during prograde evolution). The presence of kyanite+sapphirine in garnet cores and the presence of isolated sillimanite inclusions in the rim area of the same garnets in Domain$_1$ indicate that the rock has entered into the sillimanite stability field from the kyanite stability field during garnet growth. Hence, the textural evidence coupled with thermobarometric calculations indicate that the HC records decompression from the kyanite stability field to the sillimanite stability field during prograde metamorphism (Figure 11).

Hiroi et al. (1994) also suggested a prograde decompression stage for granulite facies rocks (including sapphirine-bearing granulites), on the basis of equilibrium conditions between garnet (X_{Grs} = 0.08), plagioclase (X_{An}0.1, assumed), kyanite and quartz. These authors estimated peak P conditions ~12.5 kbar at ~600°C. Dharmapriya, Malaviarachchi, Kriegsman, Galli, et al. (2017) attempted to estimate the prograde $P–T$ evolution of metasedimentary rocks using an HT/marginally UHT metapelite coupled with phase equilibria modelling and mineral textures preserved in porphyroblastic garnet. These authors calculated the pre-melting, original rock composition through stepwise re-integration of melt into the residual, XRF-based composition. According to those studies, the earliest recognizable stage occurred in the sillimanite field at ~575°C at 4.5 kbar. The subsequent $P–T$

trajectory may have had an average dP/dT of ~30 bar/°C in the kyanite field, up to 660°C at 6.5 kbar, before crossing the wet-solidus at ~675°C at 7.5 kbar. The highest-pressure condition reached was estimated at P > 10 kbar and T ~780°C before prograde decompression associated with further heating. At 825°C and 10.5 kbar, the rock re-entered into the sillimanite field (Dharmapriya, Malaviarachchi, Kriegsman, Galli, et al., 2017).

In contrast to Hiroi et al. (1994), Osanai et al. (2006) postulated that UHT granulites in the HC were subjected to prograde decompression from the eclogite facies (~17 kbar: 1,000°C) to granulite facies (~12 kbar; 1,100°C). The prograde high-P condition of >17 kbar was inferred based on the stability field of garnet+clinopyroxene+quartz in metabasites (from quartz-in and plagioclase-out lines) determined by high $P–T$ experiments of Green and Ringwood (1967) on quartz–tholeiitic composition. These authors assumed that the sapphirine granulites in the HC could also follow the same $P–T$ trajectory. However, the peak P calculation of prograde conditions (11.5–12 kbar ~800–850°C) in this study, and in most other studies on Sri Lanka, is significantly lower.

The presence of garnet+kyanite+sapphirine in garnet of Domain$_1$ and Domain$_3$ has been inferred as a product of reaction 1 (Dharmapriya et al., 2016; Dharmapriya, Malaviarachchi, Santosh, et al., 2015) during prograde metamorphism. This indicates that garnet growth has taken place within the kyanite stability field. Fockenberg (1998) showed that the $P–T$ stability field of Mg-staurolite is 12–66 kbar and 608–918°C based on experimental data.
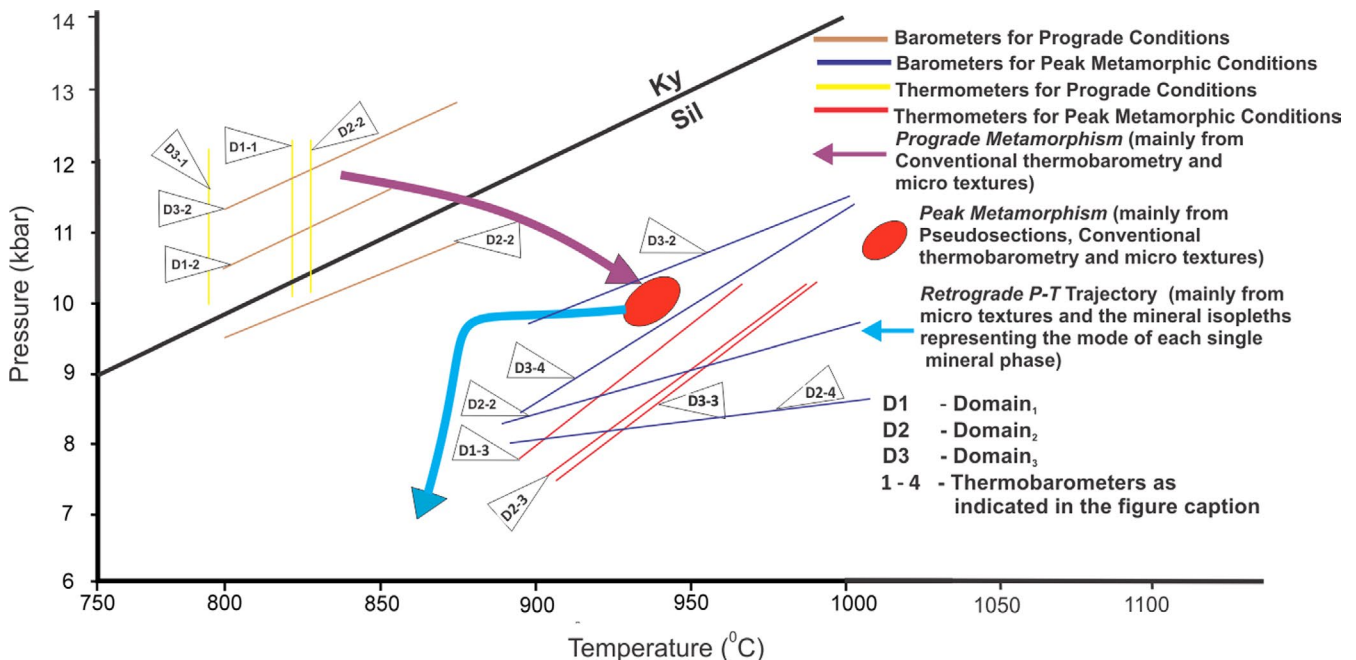

FIGURE 11 Generalized $P–T$ trajectory of the studied sapphirine granulites from the Highland Complex, based on mineral textural observations and conventional geothermobarometry and pseudosection calculations. The used geothermobarometers are (1) Ti in biotite (Henry et al., 2005), (2) Grt–Sil–Pl–Qtz (Koziol & Newton, 1988), (3) Grt–Opx geothermometer (Harley & Green, 1982), (4) Grt–Opx geobarometer (Newton & Perkins, 1982), (5) Grt–Sil–Pl–Qz geobarometer (Ganguly & Saxena, 1984) [Colour figure can be viewed at wileyonlinelibrary.com]

However, these experimental results cannot be directly applied to the natural rocks (Kelsey et al., 2006). Tsunogae and Van Reenen (2011), based on Mg-staurolite (X_{Mg} = 0.47–0.53), illustrated prograde high-P conditions at P > 14 kbar in the Central Limpopo Complex, South Africa. Sato et al. (2010) reported high-P–T experiments of staurolite with X_{Mg} = 0.5–0.7 at 12–19 kbar and 850–1,050°C. Since the reported X_{Mg} of staurolite is ~0.50 in the HC, the reaction 1 could have taken place at P–T of ~11 to 12 kbar and ~820 to 850°C. The khondalite samples ~2 km westward from the present sampling locality (X_{Mg} = 0.47) and close to Victoria dam (Dharmapriya, Malaviarachchi, Santosh, et al., 2015) also contain Mg-staurolites (X_{Mg} value ~0.50). Furthermore, Dharmapriya, Malaviarachchi, Santosh, et al. (2015) showed that the corundum-bearing UHT granulites in the Central HC also yield P from 10.5 to 11 kbar (within the sillimanite stability field) during prograde evolution. Therefore, coupled with P–T from conventional thermobarometric calculations and stability of Mg-staurolites in the HC metasediments, we interpret that the HC granulites have reached at least 11–12 kbar during the prograde evolution.

Reaction 2 in Domain$_1$ and Domain$_2$ indicate that the rocks have entered from the kyanite stability field to the sillimanite stability field via biotite dehydration melting reactions. Electron microprobe analysis of biotite inclusions in garnets indicates the incorporation of higher amount of Ti (4–7 wt%) and a considerable amount of F (0.5–1 wt%). This means that biotite melting reactions could have taken place at very high-temperature conditions during the prograde evolution. Experimental studies on melt production during granulite facies anatexis (e.g. Stevens, Clemens, & Droop, 1997) have shown that Ti-rich biotite can survive up to UHT conditions. Cesare et al. (2003) demonstrated that such high-Ti biotites are commonly hydrogen deficient, which fits the relatively high totals of our EPMA data. The stability of Ti-rich biotite at high-T conditions has been reported in many HT and UHT domains worldwide such as El Hoyazo, Spain (~850°C and 5–7 kbar:Álvarez-Valero et al., 2005), the Trivandrum Block in south India (800–850°C and P = 5 ± 1 kbar: Cesare et al., 2008) and the Gruf Complex of the Central Alps (Galli et al., 2012). Bose et al. (2005) also reported F-rich biotite (F up to 3.3 wt%) from UHT granulites in the Eastern Ghats, India. These authors have inferred high melting temperatures for the prograde assemblages. Based on a comparative study of the biotite composition with those of experimental data and their samples, these authors estimated a minimum temperature of 950°C for the terminal stability of biotite-bearing assemblages.

8.1.2 | Implications for Peak Metamorphism

Coupled with conventional thermobarometry and pseudosection calculations, it is inferred that the studied rocks have reached T ~ 930 to 940°C at P ~ 10 kbar during peak metamorphism (Figure 11). Kriegsman and Schumacher (1999) reported that sapphirine-bearing granulites at Hakuruthale and Munwatta followed a clockwise P–T path in which peak P–T reached ~9 kbar and 830°C (based on FMAS petrogenetic grids). Recalculation of theses P–T conditions using pseudosection and Al-in-orthopyroxene thermometry yielded the peak metamorphic conditions ~950°C at 10 kbar (Braun & Kriegsman, 2003), approximately equivalent with the results of this study. Sajeev and Osanai (2004) reported the coexistence of sapphirine+quartz inside garnet from sapphirine-bearing granulites around Kandy and the authors speculated that the rocks could have reached T up to 1,150°C (from isopleths of Al_2O_3 in orthopyroxene) at P of 12 kbar during peak metamorphism. These authors reported Al_2O_3 in orthopyroxene up to 13 wt% (from the samples of Ampitiya quarry; location 1 in Figure 1). Sajeev et al. (2010) refined the above-calculated peak P–T conditions to ~1,050°C at 9 kbar using pseudosections.

The coexistence of sapphirine+quartz was not observed in our samples. Instead, the presence of quartz inclusions in sapphirine-bearing garnet in Domain$_1$ and Domain$_3$ has been interpreted in terms of the incorporation of inclusion phases representing silica-saturated and silica-deficient compositional domains within single garnets in UHT pelitic granulites (Dharmapriya, Malaviarachchi, Kriegsman, Sajeev, et al., 2017). Some of the rocks (e.g Domain$_1$) contain evidence for sapphirine+melt during peak metamorphic conditions. Based on pseudosection calculations, Kelsey et al. (2005) observed that sapphirine+silicate melt can coexist above ~900°C in KFMASH, implying that such sapphirine-bearing assemblages represent UHT conditions.

Incorporation of titanohematite as a mineral phase in the peak assemblages of all studied domains indicates that the peak metamorphic conditions occurred probably at highly oxidizing conditions. UHT silica-saturated assemblages under high oxidizing conditions have been reported from many UHT granulite terrains elsewhere such as Eastern Ghats, India (Dasgupta et al., 1995; Mohan et al., 1986), Labwor Hills, Uganda (Sandiford et al., 1987) and Wilson Lake, Labrador (Morse & Talley, 1971). Furthermore, Harley (2008) noted the importance of measuring compositions of minerals such as sapphirine, orthopyroxene and spinel in such oxidized systems, due to the fact that preferential incorporation of Fe^{3+} into these minerals under highly oxidizing conditions not only shifts the P–T stability fields of typical UHT mineral assemblages but may also reverse the partitioning of Fe–Mg between the minerals (Hensen, 1986; Powell & Sandiford, 1988), thus affecting the stable UHT assemblages that can be formed.

Orthopyroxene+sillimanite+quartz in Domain$_1$ and Domain$_2$ and aluminous orthopyroxene (Al_2O_3 > 8.5 wt%) in Domain$_1$, Domain$_2$ and Domain$_3$ can be considered as

diagnostics assemblages/phases indicating UHT metamorphism (e.g. Harley, 1998, 2004, 2008; Kelsey, 2008; Kelsey & Hand, 2015). In the KFMASH system, for example, orthopyroxene–sillimanite-bearing assemblages are restricted to >900°C, and >8 kbar, in the presence of melt (e.g. Carrington & Harley, 1995; Kelsey et al., 2004). Since orthopyroxene in this quarry contains up to 20% of total iron as Fe^{3+}, the Fe^{3+} content of the orthopyroxene may have played a critical role.

Several workers (e.g. Annersten & Seifert, 1981; Powell & Sandiford, 1988) showed that the stability range of orthopyroxene+sillimanite±quartz may be extended to lower temperatures under oxidizing conditions, with preferential incorporation of Fe^{3+} into orthopyroxene. The same process decreases the amount of Al attributed to Tschermak's component and increases the X_{Mg} of the orthopyroxene (Harley, 2008). Hence, direct application of Al content of orthopyroxene (in conventional Al-in-orthopyroxene thermometry) to estimate the T in the HC could be inappropriate, especially if the rock contains evidence for high oxygen fugacity, which may overestimate the temperatures (Annersten et al., 1978; Annersten & Seifert, 1981; Harley, 2008; Powell & Sandiford, 1988).

However, the incorporation of ilmenite in the peak metamorphic assemblage of some other UHT metapelite (e.g. Dharmapriya, Malaviarachchi, Galli, et al., 2015; Dharmapriya, Malaviarachchi, Kriegsman, Galli, et al., 2017; Dharmapriya, Malaviarachchi, Santosh, et al., 2015) indicates relatively low oxygen fugacity during peak metamorphic conditions compared to the sapphirine granulites studied here. Hence, oxidizing conditions could have been variable during the peak metamorphic conditions within the HC.

8.1.3 | Retrograde evolution

The mineral textures (section Petrography) and pseudosection calculations (section P–T calculations) of the sapphirine granulites in both localities provide sufficient evidence for near-isobaric cooling after peak metamorphism. The presence of Al zonation of coarse Al-rich orthopyroxene porphyroblasts and ternary feldspars (mesoperthite) could be considered as supporting evidence for cooling of UHT granulite after peak metamorphism (Harley, 2004, 2008). Harley and Motoyoshi (2000) used the spacing of Al_2O_3 isopleths to infer that Al_2O_3 zoning in orthopyroxene is consistent with cooling after peak metamorphism. Sajeev and Osanai (2004b) also defined a near-isobaric cooling stage based on the Al zonation of orthopyroxene. Harley (2008) noted that ternary feldspar compositions (Grew, 1982; Harley, 1986; Hokada, 2001) can be used to support UHT metamorphic P–T estimates for several granulite terrains.

Leucosomes consisting of plagioclase, K-feldspar, quartz, biotite±orthopyroxene in the studied rocks probably have crystallized during this near-isobaric cooling stage from the melt phase that was produced during peak metamorphism. Reactions 9 and 10 are also likely to result from this cooling stage. Biotite in the matrix (in leucosomes) and overprinting garnet and orthopyroxene (±plagioclase) also contains a high amount of Ti (4.4–5.6 wt%) and F (0.7–1 wt%). This indicates formation of these retrograde biotites still at high-T conditions. The local melt could have been enriched in Ti and F from the melting of earlier Ti- and F-rich biotite, as proposed by Bose et al. (2005) for UHT metapelites in the Eastern Ghats.

The conventional thermobarometric calculations coupled with pseudosections indicate that the studied rocks have undergone a near-isobaric cooling stage down to ~870 to 850°C. Textural evidence for reactions (4, 5, 6 and 7) in Domain$_1$ together with pseudosection calculations provide evidence for a subsequent sequence of reactions consistent with near-isothermal decompression. Reaction 4 has classically been used to infer isothermal decompression P–T paths in UHT granulites (Kelsey et al., 2003) such as Beitbridge, Limpopo Belt, Zimbabwe (Harris & Holland, 1984); Forefinger Point, East Antarctica (Harley et al., 1990); Lützow-Holm Bay, East Antarctica (Motoyoshi & Ishikawa, 1997) and Sri Lanka (Kriegsman & Schumacher, 1999; Sajeev & Osanai, 2004). Reaction 7 provides evidence for the existence of relatively highly oxidizing conditions also during the decompression stage.

Previous studies on sapphirine granulites in the HC (Bolder-Schrijver et al., 2000; Kriegsman & Schumacher, 1999) concluded that the rocks have undergone a near-isothermal decompression stage after peak metamorphism. Based on textual evidence and Al_2O_3 isopleths of orthopyroxene, Sajeev and Osanai (2004) suggested two isobaric cooling stages after peak UHT metamorphism: from 1,150 to 1,020°C after peak metamorphism (at 12 kbar), and subsequently, from ~1,000 to 950°C after a near isothermal decompression stage from ~11.5 to 9 kbar. This allowed the possibility of two separate metamorphic events. Although textural evidence of the studied sapphirine granulites reveal only a single stage of cooling and decompression event after peak UHT metamorphism (Figure 11), the retrograde trajectory derived in this study is still comparable with that proposed in previous studies (Dharmapriya, Malaviarachchi, Galli, et al., 2015; Dharmapriya, Malaviarachchi, Kriegsman, Sajeev, et al., 2017; Perera, 1987, 1994; Prame, 1991; Raase & Schenk, 1994).

8.2 | Which thermobarometric approach would be the best for retrieving P–T evolution of UHT granulites?

UHT granulite-facies metamorphism was defined by Harley (1998) as the thermal extreme of regional metamorphic conditions that can be attained in the crust, reaching temperatures

of more than 900°C. The reconstruction of the prograde and peak metamorphic conditions of these UHT granulites is predominantly challenging because of the common overprinting of early phases and peak assemblages by post-mineral assemblages, resetting of the original mineral compositions during cooling and/or changes in the bulk composition due to the addition or loss of melts and fluids (e.g. Harley, 2008; Kelsey, 2008; Kelsey & Hand, 2015). Although phase diagrams and conventional geothermobarometry are being used as two main thermodynamic approaches to calculate $P–T$ conditions and reconstruct the metamorphic evolution, recent advancements in thermodynamic databases have provided a platform for implementation of advanced modelling toolkits (Doukkari, 2018; Kelsey & Hand, 2015; Palin et al., 2016; Powell & Holland, 2008).

'Forward' phase diagrams calculated for specific rock compositions (pseudosections, first designed by Hensen, 1971), if integrated with textural observations and mineral chemistry, may allow estimating the peak UHT conditions at which a rock equilibrated and reconstructing the post-peak $P–T$-trajectory. Important advantages of the pseudosection approach are (a) the ability to model complex chemical systems approaching a real rock system; (b) the ability to contour the mineral compositions (e.g. Al content of orthopyroxene, X_{Grs} in garnet), which is more useful to refine the stability field of the particular mineral assemblage and (c) the independence from mineral compositions, which avoids possible uncertainties due to post-peak resetting of mineral compositions.

Hence, deriving peak and post-peak metamorphic conditions of HT/UHT granulites using forward phase equilibria modelling has become one of the essential components in recent petrological research (e.g. Brandt et al., 2011; Dharmapriya, Malaviarachchi, Santosh, et al., 2015; Iwamura et al., 2013; Korhonen, Brown, Clark, & Bhattacharya, 2013; Shimizu et al., 2013).

Using forward phase equilibria modelling on four types of MgAl-rich granulites, Brandt et al. (2011) constrained the $P–T$ evolution of HP-UHT granulites from the Palni Hills, South India. They argued that the preservation of porphyroblastic orthopyroxene in leucosomes in their studied UHT granulites suggests melt loss from the rocks (e.g. White et al., 2004), which implies a change of the bulk-rock composition during the prograde evolution. Hence, the authors based the early stages of the metamorphic evolution mainly on changes in the stable aluminosilicate, which are robust against bulk chemistry changes. The prograde segment of the inferred $P–T$ path is therefore qualitative (Brandt et al., 2013). To integrate the prograde conditions, the authors also used the grossular isopleths in garnet and, finally, to refine the peak and retrograde metamorphic conditions they used Al in orthopyroxene isopleths. Iwamura et al. (2013) also combined forward phase equilibria modelling with the isopleths of anorthite content in plagioclase and Al content in orthopyroxene to elucidate the

$P–T$ evolution of spinel–sapphirine-bearing mafic granulites from Akarui Point, Lützow-Holm Complex, East Antarctica.

Conversely, the major limitation of this forward phase equilibria modelling is the choice of an appropriate 'reactive' rock composition to be modelled, which needs to be representative of a rock in equilibrium. In this sense, at different stages of the metamorphic evolution, different problems have to be considered in the choice of the input composition, especially in HT/UHT rocks (e.g. Kelsey & Hand, 2015; White & Powell & Clarke, 2002; White, Powell, & Halpin, 2004). During the pre-peak and peak evolution of a partially molten rock, the assumed loss of melt (or at least part of it) from the system would cause progressive changes in the bulk composition towards more residual compositions with increasing temperature and degree of melt loss (e.g. Dharmapriya, Malaviarachchi, Kriegsman, Galli, et al., 2017; White et al., 2002, 2004). Therefore, the exact composition before melt-loss is unknown and can only be modelled, that is, estimated by melt re-integration into the system (e.g. Dharmapriya, Malaviarachchi, Kriegsman, Galli, et al., 2017; White et al., 2004). To offer a reasonable approximation of the protolith composition at sub-solidus conditions, the method of White et al. (2004) was followed with stepwise re-integration of melt until reaching a composition that allows the wet solidus to be calculated, as exemplified by aluminous metapelites from Broken Hill, Australia. This offers a good approximation for most of the major oxides. However, the approach cannot predict variations in Ti and ferric iron because these components are not (yet) included in the melt model for pelitic compositions (Dharmapriya, Malaviarachchi, Kriegsman, Galli, et al., 2017; White et al., 2007).

A number of factors can potentially affect the accuracy and precision of the calculated forward phase diagrams, such as (a) geological uncertainty related to natural petrographic variation at the sample- and/or thin section-scale, which influences the sample's bulk composition, that is, the primary control on its equilibrium phase relationships (Palin et al., 2016); (b) uncertainties related to end-member data within the thermodynamic datasets (e.g. Powell & Holland, 2008) and (c) determination of the effective bulk composition, including XRF (Palin et al., 2016; Stüwe, 1997).

On the other hand, HT/UHT granulite facies metamorphism is always associated with anatexis. The melt produced may not completely escape from the system and could crystallize as in-situ pockets that react with the granulites during cooling (Kriegsman & Hensen, 1998). Such migmatitic rocks are often heterogeneous and composed of microdomains of residuum (melanosome) and melt (leucosome), which are impossible to separate. Thus, the total bulk composition, as measured, for example, by XRF, is their sum and could be less meaningful. During the post-peak evolution, decreased cation diffusion rates and loss of melt during cooling may result in the formation of micro-scale volumes of equilibration. In this

context, a specific reactive microdomain of equilibration is unlikely to correspond to the bulk of the rock (Stüwe, 1997). In such cases, the inverse phase equilibria modelling approach could be used to estimate more realistic P–T values. The bulk chemical compositions of the specific mineral paragenesis can be obtained from the EPMA (under X-ray area scanning mode; e.g. Clarke et al., 2001; Marmo et al., 2002), or by recalculating using EPMA mineral chemistry and the volume percentages of the particular mineral phase (as was done in this study). For example, Palin et al. (2016) presented two case studies, using garnet–cordierite granofels and garnet–staurolite–kyanite schists to assess the relative importance of geological uncertainty on bulk compositions. These authors determined the bulk chemical compositions via (a) X-ray fluorescence (XRF) and (b) point counting techniques together with EPMA mineral data. Applying the second method to multiple thin sections of heterogeneous garnet–staurolite–kyanite schist revealed a significant variation in mineral proportions and, as a consequence, a wide range in major-element oxides. Palin et al. (2016) further showed that pseudosections constructed for such bulk chemical compositions derived through point counting more accurately reproduce equilibrated mineral assemblages than those calculated using whole-rock XRF compositions.

The conventional geothermobarometric approach has the advantage to be independent of the bulk rock composition. Nevertheless, in high-grade rocks, due to high cation diffusivity (especially of Fe and Mg), mineral compositions are easily reset (Harley, 1998, 2004, 2008; Pattison et al., 2003). Therefore, the choice of an appropriate phase composition is rather problematic. As summarized by Harley (2008), the best geothermobarometers in UHT rocks are those based on the alumina content of orthopyroxene in equilibrium with garnet (e.g. Aranovich & Berman, 1997; Fitzsimons & Harley, 1994; Harley, 1984, 1998, 2004, 2008; Harley & Green, 1982). For example, Fitzsimons and Harley (1994) presented thermobarometric calculations for two suites of garnet–orthopyroxene–plagioclase–quartz rocks from East Antarctica (the Brattstrand Bluffs coastline of Prydz Bay and the Nemesis Glacier region of the northern Prince Charles Mountains). The authors reported that the corrected temperatures are closure temperatures for Al diffusion, which are likely to be good estimates of the peak metamorphic temperature. Retrograde Fe-Mg exchange has clearly been significant in these rocks, with major consequences for thermobarometry and the temperature correction in these specimens was up to 140°C.

Furthermore, due to still existing limitations of thermodynamic datasets, the P–T evolution is difficult to evaluate using both the forward and/or inverse phase equilibria modelling when some additional elements have significant concentrations. For example, if Zn-rich spinel is present as a stable mineral phase during the P–T trajectory of the rock,

then it is unfeasible to get liable result using phase equilibria modelling due to the lack of suitable solution model for such spinels (e.g. Dharmapriya et al., 2014). Also, to model Zn-spinel, we would need to know how Zn partitions into garnet, orthopyroxene, sapphirine, etc., that coexist with Zn-rich spinel, but such data are still lacking. For instance, Dharmapriya et al. (2014) reported the coexistence of Zn-rich spinel (ZnO content up to 15.8 wt%) and quartz in garnet from the southwestern part of the HC Sri Lanka, in which forward phase equilibria modelling indicated that the two minerals coexist at temperatures >925°C and pressures between 5 and 8 kbar. In the meantime, those authors modelled an adjacent intermediate granulite bearing the same spinel–quartz assemblage. The results indicated that the intermediate granulite did not reach the UHT metamorphic conditions during the peak metamorphism. Also, the conventional thermobarometric calculations using the spinel–quartz-bearing pelitic granulite indicated that the peak metamorphic conditions did not exceed T of 900°C and P of 7.5–8.5 kbar. Hence, Dharmapriya et al. (2014) concluded that the overestimated peak metamorphic T during the pseudosection modelling is probably due to the lack of proper thermodynamic data to account for Zn in the modelling, which hampers the quantification of its role.

By contrast, some UHT granulite facies rocks show a lack of diagnostic minerals (e.g. Al-rich orthopyroxene) or mineral assemblages to demonstrate UHT conditions. In such circumstances, it is difficult to retrieve peak UHT conditions via phase equilibrium modelling because the P–T stability fields may be very broad (e.g. White et al., 2002). Then, peak metamorphic conditions could be calculated from conventional thermometers such as two-feldspar thermometry (e.g. Fuhrman & Lindsley, 1988) or alternatively using trace element thermometry (e.g. Ferry & Watson, 2007; Tomkins et al., 2007). But the most consistent result can only be obtained from the trace element thermometry if the trace element is present in sufficient concentration to saturate the rock (e.g. Ferry & Watson, 2007). If that is not the case, then the application of the thermometers requires a good estimate of the activity of that trace element, which may again give rise to a fair degree of uncertainty (Kelsey & Hand, 2015). Intergrain diffusion and trace element exchange by fluid-mediated recrystallization during retrograde metamorphism could also result in a large spread of calculated temperatures from trace element thermometers. For example, Meyer, John, Brandt and Klemd (2011) studied ultra-high temperature (UHT) metamorphic rocks from the Epupa Complex in NW-Namibia using Zr-in-rutile thermometry, conventional thermobarometry and pseudosection modelling. Ortho- and para-gneisses recorded peak metamorphic UHT conditions of 970 ± 40°C at 9.5 ± 2 kbar, as estimated from conventional thermobarometry and constraints from pseudosection modelling (Meyer et al., 2011). In contrast, all Zr-in-rutile thermometry calibrations, except one, gave similar temperature estimates for

the studied samples and calculated temperatures in the wide range of <400°C to >1,000°C. These authors concluded that the range of calculated temperatures is due to inter-grain diffusion and trace element exchange by fluid-mediated recrystallization during the retrograde metamorphic evolution.

Recently, Clark et al. (2019) attempted to estimate the peak metamorphic condition from a highly residual granulite facies migmatitic rock from Lunnyy Island in the Rauer Group, East Antarctica, using multiple thermobarometric approaches. A clockwise P–T path was inferred from sequence of mineral growth with a phase equilibria modelling for the whole-rock chemical composition. The estimated peak metamorphic conditions are at 9 ± 0.5 kbar and $910 \pm 50°C$ based on conventional Al-in-orthopyroxene thermobarometry, Zr-in-rutile thermometry, and calculated compositional isopleths. These authors argued that when comparing the thermometry methods used in this study, it is apparent that the Al-in-orthopyroxene thermobarometer provides the most reliable estimate of peak conditions for their sample. Although the studied rock contains matrix rutile as an accessory phase, Ti- in- zircon thermometry yields significantly lower temperature estimates of 678–841°C. The authors argued that estimates at the upper end of this range are consistent with growth of zircon from crystallizing melt at temperatures close to the elevated (H_2O undersaturated) solidus. However, those estimates, significantly lower than the calculated temperature of this residual solidus, may reflect isolation of rutile from the effective equilibration volume leading to an activity of TiO_2 that is lower than the assumed value of unity.

In addition, our work shows that it is essential to constrain oxidizing conditions and, if needed, the activity of fluids during application of any type of thermobarometric approach. As discussed in Section 8.1.2 above, the stability field of orthopyroxene-bearing assemblages (e.g. orthopyroxene+sillimanite±quartz) may be extended to significantly lower T conditions with preferential incorporation of Fe^{3+} into orthopyroxene under highly oxidizing condition. Also, and importantly, the stability fields of sapphirine quartz-bearing assemblages extend out of the typical UHT range after considering the effects of Fe_2O_3 and TiO_2 on FMAS phase relations (e.g. Taylor-Jones & Powell, 2010). For example, Taylor-Jones and Powell (2010) showed that the stability field of sapphirine+quartz can reach temperatures >980°C in the conventionally considered FeO–MgO–Al_2O_3–SiO_2 (FMAS) chemical system. In contrast, after considering the effect of Fe^{3+} and Ti in the FeO–MgO–Al_2O_3–SiO_2–O (FMASO) and FeO–MgO–Al_2O_3–SiO_2–TiO_2–O (FMASTO) chemical systems, the stability field extends down to 850°C. Hence, the Fe^{3+} content of all minerals must be constrained during the P–T calculations. As shown by Harley (2008), it is critical to consider the effect of Fe^{3+} when the rock contains UHT mineral assemblages coexisting with phases such as hematite, hemoilmenite and titanomagnetite, rather than rutile.

As summarized by Kelsey and Hand (2015), the bulk Fe^{3+} can be calculated by three main methods: (a) by stoichiometry of mineral analyses (e.g. Droop, 1987), and using those mineral compositions expressed in Fe_2O_3 wt% and FeO wt%, in combination with mineral abundances in the mapped area of a thin section; (b) when the selected rock sample is homogeneous, titration on solutions of dissolved rock powders can be used to measure the total iron Fe^{2+} and then it is possible to recalculate the amount of FeO versus Fe_2O_3 and (c) using calculated P–X or T–X section analysis (e.g. Dharmapriya, Malaviarachchi, Galli, et al., 2015; Korhonen et al., 2012 to graphically represent the effect of changing Fe_2O_3 on the phase relationships across a range of compositions.

On the other hand, currently, most petrologists tend to estimate P–T conditions using a single collected rock sample/ rock type from an outcrop/quarry, after finding diagnostic minerals or a mineral assemblage of UHT metamorphism. Thus, the influence of such geological and other uncertainties relevant to the P–T calculations is likely to yield overestimated peak metamorphic conditions. Even though a single sample is used, if we can retrieve the P–T conditions using multiple thermobarometric approaches, then it is a possibility to get reliable results. Hence, here we encourage the retrieval of UHT metamorphic conditions using multiple thermobarometric methods for multiple lithologies as exemplified in this study. Such an integrated approaches likely to yield more reliable average thermobarometric conditions of multiple points on the P–T trajectory.

9 | CONCLUSIONS

We reach the following broad conclusions based on our petrologic study on the selected UHT rocks from the HC of Sri Lanka:

1. The presence of Al-rich orthopyroxene (Al_2O_3 up to 9 wt%) and orthopyroxene+sillimanite+quartz assemblage±sapphirine can be considered as typical indicators of UHT metamorphism. Detailed textural observations coupled with conventional thermobarometric calculations and forward and inverse pseudosection modelling indicated that the rocks have reached P up to 11–12 kbar at T ~800–850°C during prograde metamorphism. Subsequently, the rocks followed a prograde decompression event with increasing temperature up to peak UHT metamorphism at T of 920–950°C and P of 10–10.5 kbar under relatively highly oxidizing conditions. During subsequent retrogression, the rocks followed a near-isobaric cooling path down to 890–860°C, prior to near-isothermal decompression to ~6 kbar. The HC sapphirine granulites contain a considerable amount of Fe^{3+} in the UHT mineral phases and the whole-rock

composition and due to this fact the stability fields of diagnostic UHT assemblages (e.g. orthopyroxene+sillimanite+quartz) shift to lower T conditions.

2. Forward phase equilibria modelling will yield a reliable P–T result when using more restitic bulk compositions, whereas inverse phase equilibria modelling based on re-integrated bulk compositions is useful to obtain a meaningful result for migmatitic UHT granulites. However, the calculation of peak P–T conditions coupled with conventional thermobarometric methods will yield a more reliable result and can be used to minimize the uncertainties.

3. The investigation of retrograde P–T trajectories using isopleths representing the modal abundance of each mineral phase in P–T space is likely to be a more reliable approach when the rocks contain complicated retrograde mineral textures. This approach allows visualizing in which direction minerals are predicted to increase or decrease their modes (but not necessarily appear or disappear), thus revealing the position and slope of mineral reactions in a P–T diagram.

We encourage retrieving the UHT metamorphic conditions employing multiple thermobarometric methods using an integrated approach on the same UHT locality, thus yielding more reliable P–T conditions and P–T trajectories. An essential element of this approach is to do properly constrain the oxidizing conditions.

ORCID

Prasanna L. Dharmapriya [iD] https://orcid.org/0000-0001-5934-6768

REFERENCES

Ague, J. J., & Eckert, J. O. Jr (2012). Precipitation of rutile and ilmenite needles in garnet: Implications for extreme metamorphic conditions in the Acadian Orogen, U.S.A. *American Mineralogist*, *97*, 840–855. https://doi.org/10.2138/am.2012.4015

Ague, J. J., Eckert, J. O. Jr, Chu, X., Baxter, E. F., & Chamberlain, C. P. (2013). Discovery of ultrahigh-temperature metamorphism in the Acadian orogen, Connecticut, USA. *Geology*, *41*, 271–274. https://doi.org/10.1130/G33752.1

Álvarez-Valero, A. M., Cesare, B., & Kriegsman, L. M. (2005). Formation of elliptical garnet in a metapelitic enclave by melt-assisted dissolution and reprecipitation. *Journal of Metamorphic Geology*, *23*, 65–74. https://doi.org/10.1111/j.1525-1314.2005.00562.x

Annersten, H., Olesch, M., & Seifert, F. A. (1978). Ferric iron in orthopyroxene: A Mössbauer spectroscopic study. *Lithos*, *11*, 301–310. https://doi.org/10.1016/0024-4937(78)90037-3

Annersten, H., & Seifert, F. (1981). Stability of assemblage orthopyroxene-sillimanite-quartz in the system MgO-FeO-Fe$_2$O$_3$-Al$_2$O$_3$-SiO$_2$-H$_2$O. *Contributions to Mineralogy and Petrology*, *77*, 158–165.

Aranovich, L. Y., & Berman, R. G. (1997). A new garnet-orthopyroxene thermometer based on reversed Al$_2$O$_3$ solubility in FeO-Al$_2$O$_3$-SiO$_2$ orthopyroxene. *American Mineralogist*, *82*, 345–353.

Baldwin, J. A., & Brown, M. (2008). Age and duration of ultrahigh-temperature metamorphism in the Anápolis-Itauçu Complex, Southern Brasília Belt, central Brazil – Constraints from U-Pb geochronology, mineral rare earth element chemistry and trace element thermometry. *Journal of Metamorphic Geology*, *26*, 213–233. https://doi.org/10.1111/j.1525-1314.2007.00759.x

Belyanin, G. A., Rajesh, H. M., Sajeev, K., & Van Reenen, D. D. (2012). Orthopyroxene + sillimanite predating sapphirine + quartz: A rare case of ultrahigh-temperature metamorphism from the Central Zone, Limpopo Complex, South Africa. *The Canadian Mineralogist*, *50*, 1153–1163. https://doi.org/10.3749/canmin.50.5.1153

Bertrand, P., Ellis, D. J., & Green, D. H. (1991). The stability of sapphirine-quartz and hypersthenes-sillimanite-quartz assemblage: An experimental investigation in the system FeO-MgO-Al$_2$O$_3$-SiO$_2$ under H$_2$O and CO$_2$ conditions. *Contributions to Mineralogy and Petrology*, *108*, 338–344.

Bolder-Schrijver, L. J. A., Kriegsman, L. M., & Touret, J. L. R. (2000). Primary carbonate/CO$_2$ inclusions in sapphirine-bearing granulites from central Sri Lanka. *Journal of Metamorphic Geology*, *18*, 259–269. https://doi.org/10.1046/j.1525-1314.2000.00254.x

Bose, S., Das, K., & Fukuoka, M. (2005). Fluorine content of biotite in granulite-grade metapelitic assemblages and its implications for the Eastern Ghats granulites. *European Journal of Mineralogy*, *17*, 665–674. https://doi.org/10.1127/0935-1221/2005/0017-0665

Brandt, S., Schenk, V., Raith, M. M., Appel, P., Gerdes, A., & Srikantappa, C. (2011). Late Neoproterozoic P-T evolution of HP-UHT granulites from the Palni Hills (South India): New constraints from phase diagram modelling, LA-ICP-MS zircon dating, and in-situ EMP monazite dating. *Journal of Petrology*, *52*, 1813–1856. https://doi.org/10.1093/petrology/egr032

Braun, I., & Kriegsman, L. M. (2003). Proterozoic crustal evolution of southernmost India and Sri Lanka. *Geological Society of London, Special Publications*, *206*, 169–202.

Carrington, D. P., & Harley, S. L. (1995). Partial melting and phase relations in high grade metapelites: An experimental petrogenetic grid in the KFMASH system. *Contributions to Mineralogy and Petrology*, *120*, 270–291. https://doi.org/10.1007/BF00306508

Cesare, B., Cruciani, G., & Russo, U. (2003). Hydrogen deficiency in Ti-rich biotite from anatectic metapelites (El Joyazo-SE Spain): Crystal-chemical aspects and implications for high-temperature petrogenesis. *American Mineralogist*, *88*, 583–595. https://doi.org/10.2138/am-2003-0412

Cesare, B., Satish-Kumar, M., Cruciani, G., Pocker, S., & Nodari, L. (2008). Mineral chemistry of Ti-rich biotite from pegmatite and metapelitic granulites of the Kerala Khondalite Belt (southeast India): Petrology and further insight into titanium substitutions. *American Mineralogist*, *93*, 327–338. https://doi.org/10.2138/am.2008.2579

Clark, C., Taylor, R. J. M., Johnson, T. E., Harley, S. M., Fitzsimons, I. C. W., & Oliver, L. (2019). Testing the fidelity of thermometers at ultrahigh temperatures. *Journal of Metamorphic Geology*, *37*, 917–934. https://doi.org/10.1111/jmg.12486

Clarke, G. L., Daczko, N. R., & Nockolds, C. (2001). A method for applying matrix corrections to X-ray intensity maps using the Bence-Albee algorithm and Matlab. *Journal of Metamorphic Geology*, *19*, 635–644. https://doi.org/10.1046/j.0263-4929.2001.00336.x

Connolly, J. A. D. (2005). Computation of phase equilibria by linear programming: A tool for geodynamic modelling and its application to subduction zone decarbonation. *Earth and Planetary Science Letters*, *236*, 524–541.

Cooray, P. G. (1962). Charnockites and their associated gneisses in the Precambrian of Ceylon. *Journal of Geological Society of London*, *118*, 239–273. https://doi.org/10.1144/gsjgs.118.1.0239

Cooray, P. G. (1984). *An Introduction to the Geology of Sri Lanka (Ceylon)*, 2nd Revised ed. p. 340.

Cooray, P. G. (1994). The Precambrian of Sri Lanka: A historic review. *Precambrian Research*, *66*, 3–18.

Dasgupta, D., Sengupta, P., Ehl, J., Raith, M., & Bardhan, S. (1995). Reaction textures in a suite of spinel granulites from the eastern Ghats Belt, India: Evidence for polymetamorphism, a partial petrogenetic grid in the system KFMASH and the roles of ZnO and Fe_2O_3. *Journal of Petrology*, *36*, 345–461. https://doi.org/10.1093/petrology/36.2.435

Dharmapriya, P. L., Malaviarachchi, S. P. K., Galli, A., Su, B.-X., Subasinghe, N. D., & Dissanayake, C. B. (2015). Rare evidence for formation of garnet+corundumduring isobaric cooling of UHT meta-pelites: New insights for retrograde P-T trajectory of the Highland Complex, Sri Lanka. *Lithos*, *220*, 300–317.

Dharmapriya, P. L., Malaviarachchi, S. P. K., Galli, A., Su, B.-X., Subasinghe, N. D., Dissanayake, C. B., Nimalsiri, T. B., & Zhu, B. (2014). P-T evolution of a spinel+quartz bearing khondalite from the Highland complex, Sri Lanka: Implications for non-UHT metamorphism. *Journal of Asian Earth Sciences*, *95*, 99–113. https://doi.org/10.1016/j.jseaes.2014.05.003

Dharmapriya, P. L., Malaviarachchi, S. P. K., Kriegsman, L. M., Galli, A., Sajeev, K., & Zhang, C. (2017). New constraints on the *P-T* path of HT/UHT metapelites from the Highland Complex of Sri Lanka. *Geoscience Frontiers*, *8*, 1405–1430. https://doi.org/10.1016/j.gsf.2016.12.005

Dharmapriya, P. L., Malaviarachchi, S. P. K., Kriegsman, L. M., Sajeev, K., Galli, A., Osanai, Y., Subasinghe, N. D., & Dissanayake, C. B. (2017). Distinct metamorphic evolution of alternating silica-saturated and silica-deficient microdomains within garnet in ultrahigh-temperature granulites: An example from Sri Lanka. *Geoscience Frontiers*, *8*, 1115–1133. https://doi.org/10.1016/j.gsf.2016.11.008

Dharmapriya, P. L., Malaviarachchi, S. P. K., Sajeev, K., & Zhang, C. (2016). New LA-ICPMS U-Pb geochronology of detrital zircons from the Highland Complex: Insights into Sri Lanka-India Gondwana linkage. *International Geology Review*, *58*, 1856–1883.

Dharmapriya, P. L., Malaviarachchi, S. P. K., Santosh, M., Tang, L., & Sajeev, K. (2015). Late-Neoproterozoic ultrahigh temperature metamorphism in the Highland Complex, Sri Lanka. *Precambrian Research*, *271*, 311–333. https://doi.org/10.1016/j.precamres.2015.10.010

Doukkari, S. A., Diener, J. F., Ouzegane, K., & Kienast, J. R. (2018). Mineral equilibrium modelling and calculated chemical potential relations of reaction textures in the ultrahigh-temperature In Ouzzal terrane (In Hihaou area, Western Hoggar, Algeria). *Journal of Metamorphic Geology,*, *36*, 1175–1198.

Droop, G. R. T. (1987). A general equation for estimating Fe^{3+} concentrations in ferromagnesian silicates and oxides from microprobe analyses, using stoichiometric criteria. *Mineralogical Magazine*, *51*, 431–435.

Faulhaber, S., & Raith, M. (1991). Geothermometry and geobarometry of high-grade rocks: A case study on garnet–pyroxene granulites in southern Sri Lanka. *Mineralogical Magazine*, *55*, 17–40. https://doi.org/10.1180/minmag.1991.055.378.04

Fernando, G. W. A. R., Dharmapriya, P. L., & Baumgartner, L. P. (2017). Silica-undersaturated reaction zones at a crust–mantle interface in the Highland Complex, Sri Lanka: Mass transfer and melt infiltration during high-temperature metasomatism. *Lithos*, *284–285*, 237–256. https://doi.org/10.1016/j.lithos.2017.04.011

Fernando, G. W. A. R., Hauzenberger, C. A., Baumgartner, L. P., & Hofmeister, W. (2003). Modeling of retrograde diffusion zoning in garnet: Evidence for slow cooling of granulites from the Highland Complex of Sri Lanka. *Mineralogy and Petrology*, *78*, 53–71. https://doi.org/10.1007/s00710-002-0224-1

Ferry, J. M., & Watson, E. B. (2007). New thermodynamic models and revised calibrations for the Ti-in-zircon and Zr-in-rutile thermometers. *Contributions to Mineralogy and Petrology*, *154*, 429–437. https://doi.org/10.1007/s00410-007-0201-0

Fitzsimons, I. C. W., & Harley, S. L. (1994). The influence of retrograde cation exchange on granulite P-T estimates and a convergence technique for the recovery of peak metamorphic conditions. *Journal of Petrology*, *35*(2), 543–576. https://doi.org/10.1093/petrology/35.2.543

Fockenberg, T. (1998). An experimental study of the pressure-temperature stability of Mg-Alpumpellyite in the system MgO-Al_2O_3-SiO_2-H_2O. *American Mineralogist*, *83*, 220–227.

Forshaw, J. B., Waters, D. J., Pattison, D. R. M., Palin, R. M., & Gopon, P. A. (2019). Comparison of observed and thermodynamically predicted phase equilibria and mineral compositions in mafic granulites. *Journal of Metamorphic Geology*, *37*, 153–179.

Frost, B. R., & Chacko, T. (1989). The granulite uncertainty principle: Limitations on thermobarometry in granulites. *Journal of Geology*, *97*, 435–450. https://doi.org/10.1086/629321

Fu, B., Page, F. Z., Cavosie, A. J., Fournelle, J., Kita, N. T., Lackey, J. S., Wilde, S. A., & Valley, J. W. (2008). Ti-in-zircon thermometry: Applications and limitations. *Contributions to Mineralogy and Petrology*, *156*, 197–215. https://doi.org/10.1007/s00410-008-0281-5

Fuhrman, M. L., & Lindsley, D. H. (1988). Ternary-feldspar modeling and thermometry.. *American Mineralogist*, *73*, 201–215.

Galli, A., Le Bayon, B., Schmidt, M. W., Burg, J. P., Reusser, E., Sergeev, S. A., & Larionov, A. (2012). U-Pb zircon dating of the Gruf Complex: Disclosing the late Variscan granulitic lower crust of Europe stranded in the Central Alps. *Contributions to Mineralogy and Petrology*, *163*, 353–378.

Ganguly, J., & Saxena, S. K. (1984). Mixing proporties of aluminosilicate garnets: Constraints from natural and experimental data, and applications to geothermo-barometry. *American Mineralogist*, *69*, 88–97.

Green, D. H., & Ringwood, A. E. (1967). An experimental investigation of the gabbro to eclogite transformation and its petrological applications. *Geochemica Cosmochimica Acta*, *31*, 767–833. https://doi.org/10.1016/S0016-7037(67)80031-0

Grew, E. S. (1982). Sapphirine, kornerupine, and sillimanite + orthopyroxene in the charnockitic region of South India. *Journal of the Geological Society of India*, *23*, 469–505.

Harris, N. B. W., & Holland, T. J. B. (1984). The significance of cordierite-hypersthene assemblages from the Beitbridge region of the central Limpopo belt: evidence for rapid decompression in the Archaean?. *American Mineralogist*, *69*, 1036–1049.

Harley, S. L. (1984). The solubility of alumina in orthopyroxene coexisting with garnet in FeO–MgO–Al_2O_3–SiO_2 and CaO–FeO–MgO–Al_2O_3–SiO_2. *Journal of Petrology*, *25*, 665–696. https://doi.org/10.1093/petrology/25.3.665

Harley, S. L. (1986). A sapphirine-cordierite-garnet-sillimanite granulite from Enderby Land, Antarctica: Implications for FMAS petrogenetic grids in the granulite facies. *Contributions to Mineralogy and Petrology*, *94*, 452–460. https://doi.org/10.1007/BF00376338

Harley, S. L. (1989). The origins of granulites – A metamorphic perspective. *Geological Magazine*, *126*(3), 215–247. https://doi.org/10.1017/S0016756800022330

Harley, S. L., Hensen, B. J., & Sheraton, J. W. (1990). Two-stage decompression in orthopyroxene–sillimanite granulites from Forefinger Point, Enderby Land, Antarctica: implications for the evolution of the Archaean Napier Complex. *Journal of Metamorphic Geology*, *8*, 591–613.

Harley, S. L. (1998). On the occurrence and characterization of ultrahigh temperature crustal metamorphism. In P. J. Treloar and P. J. O'Brien (Eds.), *What drives metamorphism and metamorphic relations? Geological Society of London, Special Publication*, *138*, 81–107.

Harley, S. L. (2004). Extending our understanding of ultrahigh temperature crustal metamorphism. *Journal of Mineralogical and Petrological Sciences*, *99*, 140–158. https://doi.org/10.2465/jmps.99.140

Harley, S. L. (2008). Refining the *P-T* records of UHT crustal metamorphism. *Journal of Metamorphic Geology*, *26*, 125–154. https://doi.org/10.1111/j.1525-1314.2008.00765.x

Harley, S. L., & Green, D. H. (1982). Garnet-orthopyroxene barometry for granulites and peridotites. *Nature*, *300*, 697–701. https://doi.org/10.1038/300697a0

Harley, S. L., & Motoyoshi, Y. (2000). Al zoning in orthopyroxene in a sapphirine quartzite: Evidence for >1120°C UHT metamorphism in the Napier Complex, Antarctica, and implications for the entropy of sapphirine. *Contributions to Mineralogy and Petrology*, *138*, 293–307.

He, X. F., Santosh, M., Tsunogae, T., & Malaviarachchi, S. P. K. (2015). Early to late Neoproterozoic magmatism and magma mixing & mingling in Sri Lanka: Implications for convergent margin processes. *Gondwana Research*, *32*, 151–180.

He, X. F., Santosh, M., Tsunogae, T., Malaviarachchi, S. P. K., & Dharmapriya, P. L. (2016). Neoproterozoic arc accretion along the 'eastern suture' in Sri Lanka during Gondwana assembly. *Precambrian Research*, *279*, 57–80. https://doi.org/10.1016/j.precamres.2016.04.006

Henry, D. J., Guidotti, C. V., & Thomson, J. A. (2005). The Ti-saturation surface for low-to-mediumpressure metapelitic biotites: Implications for geothermometry and Ti substitution mechanism. *American Mineralogists*, *90*, 316–328.

Hensen, B. J. (1971). Theoretical phase relations involving cordierite and garnet in the system MgO-FeO-Al_2O_3-SiO_2. *Contributions to Mineralogy and Petrology*, *33*, 191–214. https://doi.org/10.1007/BF00374063

Hensen, B. J. (1986). Theoretical phase relations involving cordierite and garnet revisited: The influence of oxygen fugacity on the stability of sapphirine and spinel in the system Mg–Fe–Al–Si–O. *Contributions to Mineralogy and Petrology*, *92*, 362–367. https://doi.org/10.1007/BF00572165

Hensen, B. J. (1988). Chemical potential diagrams and chemographic projections: Application to sapphirine-granulites from Kiranur and Ganguvarpatti, Tamil Nadu. Evidence for rapid uplift in part of the South Indian Shield? *Neues Jahrbuch Fur Mineralogie Abhandlungen*, *158*, 193–210.

Hensen, B. J., & Green, D. H. (1973). Experimental study of the stability of cordierite and garnet in pelitic compositions at high pressures and temperatures. III. Synthesis of experimental data and geological applications. *Contributions to Mineralogy and Petrology*, *38*, 151–166. https://doi.org/10.1007/BF00373879

Hensen, B. J., & Harley, S. L. (1990). Graphical analysis of *P-T–X* relations in granulite facies metapelites. In J. R. Ashworth, & M. Brown (Eds.), *High temperature metamorphism and crustal anatexis* (pp. 19–56). Unwin Hyman.

Hirayama, E., Tsunogae, T., Malaviarachchi, S. P. L., Takamura, T., Dharmapriya, P. L., & Tsutsumi, Y. (2020). Prolonged neoproterozoic high-grade metamorphism of the Wanni Complex, Sri Lanka: New insights from petrology, phase equilibria modelling, and zircon U-Pb geochronology of partially melted cordierite gneiss from Walpita. *Geological Journal*, *2020*, 1–22.

Hiroi, Y., Ogo, Y., & Namba, K. (1994). Evidence for prograde metamorphic evolution of Sri Lankan pelitic granulites, and implications for the development of continental crust. *Precambrian Research*, *66*, 245–263. https://doi.org/10.1016/0301-9268(94)90053-1

Hokada, T. (2001). Feldspar thermometry in ultrahigh-temperature metamorphic rocks: Evidence of crustal metamorphism attaining ~1100 C in the Archean Napier Complex, East Antarctica. *American Mineralogist*, *86*, 932–938. https://doi.org/10.2138/am-2001-0718

Holland, T. J. B., & Powell, R. (1998). An internally consistent thermodynamic dataset for phases of petrological interest. *Journal of Metamorphic Geology*, *16*, 309–343.

Hölzl, S., Hofmann, A. W., Todt, W., and Kröner, A. (1994). U-Pb geochronology of the Sri Lanka basement. In M. Raith and S. Hoernes

(Eds.), *Tectonic, Metamorphic and Isotopic Evolution of Deep Crustal Rocks, With Special Emphasis on Sri Lanka. Precambrian Research*, *66*, 123–149.

Iwamura, S., Tsunogae, T., Kato, M., Koizumi, T., & Dunkley, D. J. (2013). Petrology and phase equilibrium modelling of spinel-sapphirine-bearing mafic granulite from Akarui Point, Lützow-Holm Complex, East Antarctica: Implications for the P-T path. *Journal of Mineralogical and Petrological Sciences*, *108*, 345–350.

Jiao, S., & Guo, J. (2011). Application of the two-feldspar geothermometer to ultrahigh-temperature (UHT) rocks in the Khondalite belt, North China craton and its implications. *American Mineralogist*, *96*, 250–260. https://doi.org/10.2138/am.2011.3500

Kehelpannala, K. V. W. (1997). Deformation of a high-grade Gondwana fragment, Sri Lanka. *Gondwana Research*, *1*, 47–68. https://doi.org/10.1016/S1342-937X(05)70005-8

Kelsey, D. E. (2008). On ultrahigh-temperature crustal metamorphism. *Gondwana Research*, *13*, 1–29. https://doi.org/10.1016/j.gr.2007.06.001

Kelsey, D. E., Clark, C., Hand, M., & Collins, A. S. (2006). Comment on ''First report of garnet-corundum rocks from southern India: Implications for prograde high-pressure (eclogite-facies?) metamorphism''. *Earth and Planetary Science Letters*, *249*, 529–534. https://doi.org/10.1016/j.epsl.2006.07.048

Kelsey, D. E., & Hand, M. (2015). On ultrahigh temperature crustal metamorphism: Phase equilibria, trace element thermometry, bulk composition, heat sources, timescales and tectonic settings. *Geoscience Frontiers*, *6*, 311–356. https://doi.org/10.1016/j.gsf.2014.09.006

Kelsey, D. E., & Powell, R. (2011). Progress in linking accessory mineral growth and breakdown to major mineral evolution in metamorphic rocks: A thermodynamic approach in the $Na_2O-CaO-K_2O-FeO-MgO-Al_2O_3-SiO_2-H_2O-TiO_2-ZrO_2$ system. *Journal of Metamorphic Geology*, *29*, 151–166. https://doi.org/10.1111/j.1525-1314.2010.00910.x

Kelsey, D. E., White, R. W., Holland, T. J. B., & Powell, R. (2004). Calculated phase equilibria in $K_2O-FeO-MgO-Al_2O_3-SiO_2-H_2O$ for sapphirine-quartz-bearing mineral assemblages. *Journal of Metamorphic Geology*, *22*, 559–578. https://doi.org/10.1111/j.1525-1314.2004.00533.x

Kelsey, D. E., White, R. W., & Powell, R. (2003). Orthopyroxene-sillimanite-quartz assemblages: Distribution, petrology, quantitative *P-T-X* constraints and *P-T* paths. *Journal of Metamorphic Geology*, *21*, 439–453. https://doi.org/10.1046/j.1525-1314.2003.00456.x

Kelsey, D. E., White, R. W., & Powell, R. (2005). Calculated phase equilibria in $K_2O-FeO-MgO-Al_2O_3-SiO_2-H_2O$ for silica-undersaturated sapphirine bearing mineral assemblages. *Journal of Metamorphic Geology*, *23*, 217–239. https://doi.org/10.1111/j.1525-1314.2005.00573.x

Kitano, I., Osanai, Y., Nakano, N., Adachi, T. (2015). LA-ICP-MS Zircon U-Pb ages from metamorphic rocks in the southwestern part of Highland Complex, Sri Lanka. Japan Geoscience Union Meeting, 2015. Makuhari, Chiba, Japan.

Kitano, I., Osanai, Y., Nakano, N., Adachi, T., & Fitzsimons, I. C. W. (2018). Detrital zircon and igneous protolith ages of high-grade metamorphic rocks in the Highland and Wanni Complexes, Sri Lanka: Their geochronological correlation with southern India and East Antarctica. *Journal of Asian Earth Science*, *156*, 122–144. https://doi.org/10.1016/j.jseaes.2018.01.017

Kooijman, E., Smit, M. A., Mezger, K., & Berndt, J. (2012). Trace element systematics in granulite facies rutile: Implications for Zr geothermometry and provenance studies. *Journal of Metamorphic Geology*, *30*, 397–412. https://doi.org/10.1111/j.1525-1314.2012.00972.x

Korhonen, F. J., Powell, R., & Stout, J. H. (2012). Stability of sapphirine + quartz in the oxidized rocks of the Wilson Lake terrane, Labrador: calculated equilibria in NCKFMASHTO. *Journal of Metamorphic Geology*, *30*, 21–36.

Korhonen, F. J., Brown, M., Clark, C., & Bhattacharya, S. (2013). Osumilite-melt interactions in ultrahigh temperature granulites: Phase equilibria modelling and implications for the P-T-t evolution of the Eastern Ghats Province, India. *Journal of Metamorphic Geology*, *31*, 881–907.

Koziol, A. M., & Newton, R. C. (1988). Redetermination of the anorthite breakdown reaction and improvement of the plagioclase-garnet-Al_2SiO_5 geobarometer. *American Mineralogist*, *73*, 216–223.

Kriegsman, L. M. (1995). The Pan-African event in East Antarctica: A view from Sri Lanka and the Mozambique Belt. *Precambrian Research*, *75*, 263–277. https://doi.org/10.1016/0301-9268(95)80010-F

Kriegsman, L. M. (1996). Divariant and trivariant reaction line slopes in FMAS and CFMAS: Theory and applications. *Contributions to Mineralogy and Petrology*, *126*, 38–50. https://doi.org/10.1007/s004100050234

Kriegsman, L. M. (2001). Quantitative field methods for estimating melt production and melt loss. *Physics and Chemistry of the Earth, A*, *26*, 247–253. https://doi.org/10.1016/S1464-1895(01)00052-7

Kriegsman, L. M., & Álvarez-Valero, A. M. (2010). Melt-producing versus melt-consuming reactions in pelitic xenoliths and migmatites. *Lithos*, *116*, 310–332. https://doi.org/10.1016/j.lithos.2009.09.001

Kriegsman, L. M., & Hensen, B. J. (1998). Back reaction between restite and melt: Implications for geothermobarometry and pressure-temperature paths. *Geology*, *26*(12), 1111–1114.

Kriegsman, L. M., & Schumacher, J. C. (1999). Petrology of sapphirine bearing and associated granulites from central Sri Lanka. *Journal of Petrology*, *40*, 1211–1239. https://doi.org/10.1093/petroj/40.8.1211

Kröner, A., Cooray, P. G., & Vitanage, P. W. (1991). Lithotectonic subdivision of the Precambrian basement in Sri Lanka. In A. Kröner (Ed.), *The Crystalline Crust of Sri Lanka, Part1. Summary of Research of the German-Sri Lankan Consortium*. Geological Survey Department, Sri Lanka, Professional Papers, *5*, pp. 5–21.

Kröner, A., Jaeckel, P., & Williams, I. S. (1994). Pb-loss patterns in zircons from a high-grade metamorphic terrain as revealed by different dating methods: U-Pb and Pb–Pb ages for igneous and metamorphic zircons from northern Sri Lanka. *Precambrian Research*, *66*, 151–181. https://doi.org/10.1016/0301-9268(94)90049-3

Kröner, A., Rojas-Agramonte, Y., Kehelpannala, K., Zack, T., Hegner, E., Geng, H. Y., Wong, J., & Barth, M. (2013). Age, Nd–Hf isotopes, and geochemistry of the Vijayan Complex of eastern and southern Sri Lanka: A Grenville-age magmatic arc of unknown derivation. *Precambrian Research*, *234*, 288–321. https://doi.org/10.1016/j.precamres.2012.11.001

Kröner, A., & Williams, I. S. (1993). Age of metamorphism in the high-grade rocks of SriLanka. *Journal of Geology*, *101*, 513–521. https://doi.org/10.1086/648243

Lal, R. K., Ackermand, D., & Upadhyay, H. (1987). *P-T–X* relationships deduced from corona textures in sapphirine–spinel–quartz assemblages from Paderu, southern India. *Journal of Petrology*, *28*, 1139–1168. https://doi.org/10.1093/petrology/28.6.1139

Liew, T. C., Milisenda, C. C., Hölzl, S., Köhler, H., & Hofmann, A. W. (1991). Isotopic characterization of the high-grade basement

rocks of Sri Lanka. In A. Kröner (Ed.), *The Crystalline Crust of Sri Lanka, Part I. Summary of Research of the German-Sri Lankan Consortium*. Geological Survey Department, Sri Lanka, pp. 258–267. Professional Paper 5.

Malaviarachchi, S. P. K. (2018). Review on age of magmatism and crust formation in Sri Lanka: U-Pb and Lu–Hf isotopic perspectives. *Journal of Indian Institute of Science*, *98*, 417. https://doi.org/10.1007/s41745-018-0069-1

Malaviarachchi, S. P. K., Bindusara, S., Dharmapriya, P. L., Su, B.-C., Su, L. I., Su, B.-X., Zhang, H., Zhang, C., Sajeev, K., Sakyi, P. A., & Alemayehu, M. (2019). U-Pb geochronology of zircons from river sediments in Sri Lanka: Implications on early Archean to late Cambrian magmatism and episodic crustal growth. *Journal of Asian Earth Sciences*, *171*, 388–412. https://doi.org/10.1016/j.jseaes.2018.08.029

Malaviarachchi, S. P. K., & Dharmapriya, P. L. (2015). Revisiting ultrahigh temperature granulites of Sri Lanka: New prograde and retrograde mineral textures from the Highland complex. *Journal of Indian Institute of Science*, *95*, 159–171.

Marmo, B., Clarke, G. L., & Powell, R. (2002). Fractionation of bulk rock composition due to porphyroblast growth: Effects on eclogite facies mineral equilibria, Pam Peninsula, New Caledonia. *Journal of Metamorphic Geology*, *20*, 151–165. https://doi.org/10.1046/j.0263-4929.2001.00346.x

Mathavan, V., & Fernando, G. W. A. R. (2001). Reactions and textures in grossular–wollastonite–scapolite calc-silicate granulites from Maligawila, Sri Lanka. *Lithos*, *59*, 217–232.

Mathavan, V., Prame, W. K. B. N., & Cooray, P. G. (1999). Geology of the high grade Proterozoic terrains of Sri Lanka and the assembly of Gondwana: An update on recent developments. *Gondwana Research*, *2*, 237–250. https://doi.org/10.1016/S1342-937X(05)70148-9

Meyer, M., John, T., Brandt, S., & Klemd, R. (2011). Trace element composition of rutile and the application of Zr-in-rutile thermometry to UHT metamorphism (Epupa Complex, NW Namibia). *Lithos*, *126*, 388–401.

Milisenda, C. C., Liew, T. C., Hofmann, A. W., & Köhler, H. (1994). Nd isotopic mapping of the Sri Lankan basement: Update, and additional constraints from Sr isotopes. *Precambrian Research*, *66*, 95–110.

Milisenda, C. C., Liew, T. C., Hofmann, A. W., & Kröner, A. (1988). Isotopic mapping of age provinces in Precambrian high-grade terrains: Sri Lanka. *Journal of Geology*, *96*, 608–615. https://doi.org/10.1086/629256

Mohan, A., Ackermand, D., & Lal, R. K. (1986). Reaction textures and *P-T-X* trajectory in the sapphirine-spinel bearing granulites from Ganguvarpatti, Southern India. *Neues Jahrbuch Für Mineralogie, Abhandlungen*, *154*, 1–19.

Morse, S. A., & Talley, J. H. (1971). Sapphirine reactions in deep-seated granulites near Wilson Lake, Central Labrador, Canada. *Earth and Planetary Science Letters*, *10*, 325–328. https://doi.org/10.1016/0012-821X(71)90037-9

Motoyoshi, Y., & Ishikawa, M. (1997). Metamorphic and structural evolution of granulites from Rundvågshetta, Lützow-Holm Bay, East Antarctica. In C. A. Ricci (Ed.) *The Antarctic region: Geological evolution and processes*. Proceedings of the VII International Symposium on the Antarctic Earth Sciences, Siena, Terra Antarctica, 65–72.

Newton, R. C., Charlu, T. V., & Kleppa, O. J. (1980). Thermochemistry of the high structural state plagioclases. *Geochemica Cosmochimica Acta*, *44*, 933–941. https://doi.org/10.1016/0016-7037(80)90283-5

Newton, R. C., & Perkins, D. (1982). Thermodynamic calibration of geobarometers based on the assemblages garnet-plagioclase-orthopyroxene-(clinopyroxene)-quartz. *American Mineralogist*, *67*, 203–222.

Osanai, Y. (1989). A preliminary report on sapphirine/kor.nerupine granulite from Highland series, Sri Lanka (extended abstract). Seminar on recent advances in Precambrian Geology of Sri Lanka. IFS Kandy, Sri Lanka.

Osanai, Y., Ando, K. T., Miyashita, Y., Kusachi, I., Yamasaki, T., Doyama, D., & Mathavan, V. (2000). Geological field work in the southwestern and central parts of the Highland complex, Sri Lanka during 1998–1999, special reference to the highest grade metamorphic rocks. *Journal of Geoscience, Osaka City University*, *43*, 227–247.

Osanai, Y., Sajeev, K., Nakano, N., Kitano, I., Kehelpannala, W. K. V., Kato, R., Adachi, T., & Malaviarachchi, S. P. K. (2016a). UHT granulites of the Highland complex, Sri Lanka II: Geochronological constraints and implications for Gondwana correlation. *Journal of Mineralogical and Petrological Sciences*, *111*, 157–169. https://doi.org/10.2465/jmps.151230

Osanai, Y., Sajeev, K., Nakano, N., Kitano, I., Kehelpannala, W. K. V., Kato, R., Adachi, T., & Malaviarachchi, S. P. K. (2016b). UHT granulites of the Highland complex, Sri Lanka I: Geological and petrological background. *Journal of Mineralogical and Petrological Sciences*, *111*, 145–156. https://doi.org/10.2465/jmps.151227

Osanai, Y., Sajeev, K., Owada, M., Kehelpannala, K. V. W., Prame, W. K. B., Nakano, N., & Jayatileke, S. (2006). Metamorphic evolution of ultrahigh-temperature and high-pressure granulites from Highland Complex, Sri Lanka. *Journal of Asian Earth Sciences*, *28*, 20–37.

Palin, R. M., Weller, O. M., Waters, D. J., & Dyck, B. (2016). Quantifying geological uncertainty in metamorphic phase equilibria modelling: A Monte Carlo assessment and implications for tectonic interpretations. *Geoscience Frontiers*, *7*, 591–607. https://doi.org/10.1016/j.gsf.2015.08.005

Pattison, D. R. M., Chacko, T., Farquhar, J., & McFarlane, C. R. M. (2003). Temperatures of granulite-facies metamorphism: Constraints from experimental phase equilibria and thermobarometry corrected for retrograde exchange. *Journal of Petrology*, *44*, 867–900. https://doi.org/10.1093/petrology/44.5.867

Perera, L. R. K. (1987). Petrogenesis of Granulite-Facies Metamorphicrocks in Sri Lanka. University of Peradeniya (unpublished M. Phil. Thesis).

Perera, L. R. K. (1994). P-T–t path vs isotopic ages in correlations, anti-correlations and pseudo-correlations of regional metamorphic terrains, a case study from Sri Lanka. *Journal of Geological Society of Sri Lanka*, *5*, 27–41.

Perera, L. R. K., & Kagami, H. (2011). Centimetre-and Metre-scale Nd and Sr Isotopic Homogenization in Kadugannawa Complex, Sri Lanka. *Journal of the Geological Society of Sri Lanka*, *14*, 129–141.

Podlesskii, K. K. (2006). Geothermobarometry of orthopyroxene-bearing aluminous granulites based on internally consistent thermodynamic datasets. Granulites and Granulites 2006, Brasilia, Program and Abstracts, pp. 67.

Powell, R., & Holland, T. J. B. (1999). Relating formulations of the thermodynamics of mineral solid solutions: Activity modelling of pyroxenes, amphiboles and micas. *American Mineralogist*, *84*, 1–14.

Powell, R., & Holland, T. J. B. (2008). On thermobarometry. *Journal of Metamorphic Geology*, *26*, 155–179. https://doi.org/10.1111/j.1525-1314.2007.00756.x

Powell, R., & Sandiford, M. J. (1988). Sapphirine and spinel phase relationships in the system FeO-MgO-Al$_2$O$_3$-TiO$_2$-O$_2$ in the presence of quartz and hypersthene. *Contributions to Mineralogy and Petrology*, *98*, 64–71.

Prame, W. K. B. N. (1991). Petrology of the Kataragama Complex, Sri Lanka: Evidence for high pressure granulite facies metamorphism and subsequent isobaric cooling. Geological Survey Department, Sri Lanka, Professional Paper 5, 200–224.

Raase, R., & Schenk, V. (1994). Petrology of granulite faciesmetapelitesof the Highland Complex, Sri Lanka: Implications for metamorphic zonation and P-T path. *Precambrian Research*, *66*, 265–294.

Ratheesh-Kumar, R. T., Dharmapriya, P. L., Windley, B. F., Xiao, W. J., & Jeevan, U. (2020). The tectonic 'Umbilical Cord' linking India and Sri Lanka, and the tale of their failed rift. *Journal of Geophysical Research-Solid Earth*, *125*(5), e2019JB018225. https://doi.org/10.1029/2019JB018225

Sajeev, K., & Osanai, Y. (2004a). Osumilite and spinel + quartz from Sri Lanka: Implications for UHT conditions and retrograde *P-T* path. *Journal of Mineralogical and Petrological Sciences*, *99*, 320–327. https://doi.org/10.2465/jmps.99.320

Sajeev, K., & Osanai, Y. (2004b). Ultrahigh-temperature metamorphism (1150 °C, 12 kbar) and multi-stage evolution of Mg, Al rich granulites from the central Highland Complex, Sri Lanka. *Journal of Petrology*, *45*, 1821–1844.

Sajeev, K., Osanai, Y., Connolly, J. A. D., Suzuki, S., Ishioka, J., Kagami, H., & Rino, S. (2007). Extreme crustal metamorphism during a Neoproterozoic event in Sri Lanka, a study of dry mafic granulites. *Journal of Geology*, *115*, 563–582. https://doi.org/10.1086/519778

Sajeev, K., Osanai, Y., Kon, Y., & Itaya, T. (2009). Stability of pargasite during ultrahightemperature metamorphism: A consequence of titanium and REE partitioning? *American Mineralogist*, *94*, 535–545. https://doi.org/10.2138/am.2009.2815

Sajeev, K., Williams, I. S., & Osanai, Y. (2010). Sensitive high-resolution ion microprobe U-Pb dating of prograde and retrograde ultrahigh-temperature metamorphism as exemplified by Sri Lankan granulites. *Geological Society of America*, *38*, 971–974. https://doi.org/10.1130/G31251.1

Sandiford, M., Neale, F., & Powell, R. (1987). Metamorphic evolution of aluminous granulites from Labwor Hills, Uganda. *Contributions to Mineralogy and Petrology*, *95*, 217–225. https://doi.org/10.1007/BF00381271

Santosh, M., Tsunogae, T., Malaviarachchi, S. P. K., Zhang, Z., Ding, H., Tang, L., & Dharmapriya, P. L. (2014). Neoproterozoic crustal evolution in Sri Lanka: Insights from petrologic, geochemical and zircon U-Pb and Lu–Hf isotopic data and implications for Gondwana assembly. *Precambrian Research*, *255*, 1–29. https://doi.org/10.1016/j.precamres.2014.09.017

Sato, K., Santosh, M., & Tsunogae, T. (2010). High P-T phase relation of magnesian (Mg0.7Fe0.3) staurolite composition in the system FeO-MgO-Al$_2$O$_3$-SiO$_2$-H$_2$O: Implications for prograde high-pressure history of ultrahigh-temperature metamorphic rocks. *American Mineralogist*, *95*, 177–184.

Schreyer, W., Horrocks, P. C., & Abraham, K. (1984). High-magnesium staurolite in a sapphirine-garnet rock from the Limpopo belt, Southern Africa. *Contributions to Mineralogy and Petrology*, *86*, 200–207. https://doi.org/10.1007/BF00381847

Schumacher, R., & Faulhaber, S. (1994). Summary and discussion of P-T estimates from garnet–pyroxene–plagioclase–quartz-bearing granulite-facies rocks from Sri Lanka. *Precambrian Research*, *66*, 295–308. https://doi.org/10.1016/0301-9268(94)90055-8

Seifert, F. (1974). Stability of sapphirine: A study of the aluminous part of the system MgO–Al$_2$O$_3$–SiO$_2$–H$_2$O. *Journal of Geology*, *82*, 173–204.

Shimizu, H., Tsunogae, T., & Santosh, M. (2013). Petrology and phase equilibrium modeling of sapphirine + quartz assemblage from the Napier Complex, East Antarctica: Diagnostic evidence for Neoarchean ultrahigh-temperature metamorphism. *Geoscience Frontiers*, *4*, 655–666.

Stevens, G., Clemens, J. D., & Droop, G. T. R. (1997). Melt production during granulite-facies anatexis: Experimental data from ''primitive'' metasedimentary protoliths. *Contributions to Mineralogy and Petrology*, *128*, 352–370. https://doi.org/10.1007/s004100050314

Stüwe, K. (1997). Effective bulk composition changes due to cooling: A model predicting complexities in retrograde reaction textures. *Contributions to Mineralogy and Petrology*, *129*, 43–52.

Tajčmanová, L., Connolly, J. A. D., & Cesare, B. (2009). A thermodynamic model for titanium and ferric iron solution in biotite. *Journal of Metamorphic Geology*, *27*, 153–165. https://doi.org/10.1111/j.1525-1314.2009.00812.x

Takamura, Y., Tsunogae, T., Santosh, M., Malaviarachchi, S. P. K., & Tsutsumi, Y. (2015). Petrology and zircon U-Pb geochronology of metagabbro from the Highland Complex, Sri Lanka: Implications for the correlation of Gondwana suture zones. *Journal of Asian Earth Sciences*, *113*, 826–841. https://doi.org/10.1016/j.jseaes.2015.07.001

Takamura, Y., Tsunogae, T., Santosh, M., Malaviarachchi, S. P. K., & Tsutsumi, Y. (2016). U-Pb geochronology of detrital zircon in metasediments from Sri Lanka: Implications for the regional correlation of Gondwana fragments. *Precambrian Research*, *281*, 434–452. https://doi.org/10.1016/j.precamres.2016.06.015

Taylor-Jones, K., & Powell, R. (2010). The stability of sapphirine + quartz: Calculated phase equilibria in FeO-MgO-Al$_2$O$_3$-SiO$_2$-TiO$_2$-O. *Journal of Metamorphic Geology*, *28*, 615–633.

Tinkham, D. K., & Ghent, E. W. (2005). Estimating P-T conditions of garnet growth with isochemical phase-diagram sections and the problem of effective bulk-composition. *Canadian Mineralogist*, *43*, 35–50. https://doi.org/10.2113/gscanmin.43.1.35

Tomkins, H. S., Powell, R., & Ellis, D. J. (2007). The pressure dependence of the zirconium-in-rutile thermometer. *Journ of Metamorphic Geology*, *25*, 703–713.

Tsunogae, T., & Van Reenen, D. D. (2011). High-pressure and ultrahigh-temperature granulite-facies metamorphism of Precambrian high-grade terranes: Case study of the Limpopo Complex. In D. D. Van Reenen, J. D. Kramers, S. McCourt, and L. L. Perchuk (Eds.) *Origin and evolution of Precambrian high-grade gneiss terranes, with special emphasis on the Limpopo Complex of Southern Africa*. *Geological Society of America Memoir*, *207*, 107–124.

Vielzeuf, D., & Holloway, J.R. (1988). Experimental determination of the fluid-absent melting relations in the pelitic system: consequences for crustal differentiation. *Contributions to Mineralogy and Petrology*, *98*, 257–276.

Vielzeuf, D., Baronnet, A., Perchuk, A. L. D., Laporte, D., & Baker, M. B. (2007). Calcium diffusivity in alumino-silicate garnets: An experimental and ATEM study. *Contributions to Mineralogy and Petrology*, *154*, 153–170. https://doi.org/10.1007/s00410-007-0184-x

Waldbaum, D. R., & Thompson, J. B. J. (1969). Mixing properties of sanidine crystalline solutions: IV. Phase diagrams from equation of state. *American Mineralogist*, *54*, 1274.

Watson, E. B., & Harrison, T. M. (2005). Zircon thermometer reveals minimum melting conditions on earliest Earth. *Science*, *308*, 841–844. https://doi.org/10.1126/science.1110873

Watson, E. B., Wark, D. A., & Thomas, J. B. (2006). Crystallization thermometers for zircon and rutile. *Contributions to Mineralogy and Petrology*, *151*, 413–433. https://doi.org/10.1007/s00410-006-0068-5

White, R. W., Powell, R., & Clarke, G. L. (2002). The interpretation of reaction textures in Fe-rich metapelitic granulites of the Musgrave Block, central Australia: Constraints from mineral equilibria calculations in the system $K_2O–FeO–MgO–Al_2O_3–SiO_2–H_2O–TiO_2–Fe_2O_3$. *Journal of Metamorphic Geology*, *20*, 41–55. https://doi.org/10.1046/j.0263-4929.2001.00349.x

White, R. W., Powell, R., & Halpin, J. A. (2004). Spatially-focussed melt formation in aluminous metapelites from Broken Hill, Australia. *Journal of Metamorphic Geology*, *22*, 825–845. https://doi.org/10.1111/j.1525-1314.2004.00553.x

White, R. W., Powell, R., & Holland, T. J. B. (2007). Progress relating to calculation of partial melting equilibria for metapelites. *Journal of Metamorphic Geology*, *25*, 511–527. https://doi.org/10.1111/j.1525-1314.2007.00711.x

White, R. W., Powell, R., Holland, T. J. B., Johnson, T. E., & Green, E. C. R. (2014). New mineral activity-composition relations for thermodynamic calculations in metapelitic systems. *Journal of Metamorphic Geology*, *32*, 261–286. https://doi.org/10.1111/jmg.12071

White, R. W., Powell, R., Holland, T. J. B., & Worley, B. A. (2000). The effect of TiO_2 and Fe_2O_3 on metapelitic assemblages at greenschist and amphibolite facies conditions: Mineral equilibria calculations in the system $K_2O-FeO-MgO-Al_2O_3-SiO_2-H_2O-TiO_2-Fe_2O_3$. *Journal of Metamorphic Geology*, *18*, 497–511. https://doi.org/10.1046/j.1525-1314.2000.00269.x

Whitney, D. L., & Evans, B. W. (2010). Abbreviations for names of rock-forming minerals. *American Mineralogist*, *95*, 185–187. https://doi.org/10.2138/am.2010.3371

SUPPORTING INFORMATION

Additional supporting information may be found online in the Supporting Information section.

Appendix S1. Analytical procedures.

Table S1. Ti content in zircon thermometry.

How to cite this article: Dharmapriya PL, Malaviarachchi SPK, Galli A, et al. Hybrid phase equilibria modelling with conventional and trace element thermobarometry to assess the *P–T* evolution of UHT granulites: An example from the Highland Complex, Sri Lanka. *J. Metamorph. Geol.* 2021;39:209–246. https://doi.org/10.1111/jmg.12569